Quantitative Imaging of Multi-component Turbulent Jets

by

Arash Ash

B.Sc, Eastern Mediterranean University, 2007

A Thesis Submitted in Partial Fulfillment

of the Requirements for the Degree of

MASTER OF APPLIED SCIENCES

in the Department of Mechanical Engineering

University of Victoria

Supervisory Committee

Quantitative Imaging of Multi-Component Turbulent Jets

by

Arash Ash

B.Sc, Eastern Mediterranean University, 2007

Supervisory Committee

Dr. Nedjib Djilali, (Department of Mechanical Engineering)

Co-Supervisor

Dr. Peter Oshkai, (Department of Mechanical Engineering)

Co-Supervisor

Abstract

Supervisory Committee

Dr. Nedjib Djilali, (Department of Mechanical Engineering)

Co-Supervisor

Dr. Peter Oshkai, (Department of Mechanical Engineering)

Co-Supervisor

The Gaseous state of hydrogen at ambient temperature, combined with the fact that hydrogen is highly flammable, results in the requirement of more robust, high pressure storage systems that can meet modern safety standards. To develop these new safety standards and to properly predict the phenomena of hydrogen dispersion, a better understanding of the resulting flow structures and flammable regions from controlled and uncontrolled releases of hydrogen gas must be achieved. In this study the subsonic release of hydrogen was emulated using helium as a substitute working fluid. A sharp-edged orifice round turbulent jet is used to emulate releases in which leak geometry is circular. Effects of buoyancy, crossflow and adjacent surfaces were studied over a wide range of Froude numbers. The velocity fields of turbulent jets were characterized using particle image velocimetry (PIV). The mean and fluctuation velocity components were well quantified to show the effect of buoyancy due to the density difference between helium and the surrounding air. In the range of Froude numbers investigated, increasing effects of buoyancy were seen to be proportional to the reduction of the *Fr* number. The obtained results will serve as control reference values for further concentration measurement study and for computational fluid dynamics (CFD) validation.

Table of Contents

List of Tables

List of Figures

Acknowledgments

I owe my deepest gratitude to my supervisors, Dr. Nedjib Djilali and Dr. Peter Oshkai who have supported me throughout my research with their encouragement, patience and knowledge. Thank you for giving me the opportunity to be part of this project. It has been an honour and a pleasure to work with you.

I am indebted to people who were directly or indirectly involved in development of this work. Te-Chun Wu, who has helped me throughout the project and has patiently, supported me with his knowledge. I would like to extend my thanks to Peggy White and Sue Walton from the IESVic office for all of their supports.

Finally I owe my loving thanks to my parents, thank you for everything that you have done for me. I would like to thank my wife, Sogol, for her loving support and patience. And thank to all my dear friends: Peyman, Naser, Ramtin, Nima and many others. Without their encouragement, understanding, and loving support it would have been impossible for me to finish this work.

Dedication

To my mother and father

To my wife

CHAPTER 1

INTRODUCTION

1.1 BACKGROUND

1.2 EXPERIMENTAL STUDIES OF TURBULENT JETS

Prior to the development of a hydrogen infrastructure, well-researched safety standards must be implemented to reduce the risk associated with leaks and uncontrolled combustion related to high pressure hydrogen storage. These leaks range from slow releases from small-diameter holes in delivery pipes to high volume dispersions from accidental or controlled gas venting from high-pressure storage tanks. The resulting hydrogen jet and the combustible cloud represent a potential fire hazard. To develop new safety standards, the momentum and buoyancy effects related to the rapid, uncontrolled release of hydrogen must be studied in detail to accurately determine the resultant dispersion.

Dispersion of a stream of one fluid through a fluid with different characteristics such as velocity and density which results in mixing of the stream with the surrounding ambient is called jet flow. Such flows occur in variety of ranges, sizes and geometries and are classified according to different characteristics. Turbulent flows which are not confined by solid walls and are discharged from the round orifice are called free round jets. Such flows become completely turbulent in a short distance from the point of discharge. As a result of turbulence, particles of the surrounding ambient mix with the

emerging jet and get carried away. The jet mass flow increases in downstream direction as the jet spreads and its velocity decreases but the total momentum remains constant. Such flows are in the form of boundary layer nature as the extent in the transverse direction is small comparing to the main flow and the transverse gradients are large. Laminar sub-layer does not exist in free jet flows and the turbulent friction is dominant in the whole flow which makes these jets amenable to mathematical analysis. The characteristics of the free jet flows vary greatly depending on the values of Reynolds and Mach numbers. For conditions where the value of the Mach number is less than 0.3, the resultant jet is called subsonic in which the density is independent of the variations in pressure and temperature field. In subsonic turbulent flows, at any point in the jet, the static pressure is constant and equal to the pressure in the surrounding ambient.

At the nozzle orifice, when the jet flow is first introduced to the surrounding ambient, the zone of turbulent mixing is created at the surface of discontinuity in the velocity field. In the jet near field region, the boundary layer expands but does not reach the axis of the flow. The width of the mixing region increases in downstream direction as the jet velocity decreases. The rate of increase in jet width for a subsonic discharge can be estimated by assuming the turbulent mixing length to be proportional to the width of the jet. The increase of the mixing width for free turbulent round jet is reported to be proportional to the distance from the nozzle orifice in downstream direction. The decrease in height of the velocity profile for a round turbulent jet along the jet centerline can be estimated from the jet momentum and is reported to proportional to x^{-1} for the downstream distance of x (Schlichting 1979).

The entrainment of the surrounding ambient into the turbulent jet flow leads to dilution of the jet. The initial characteristics of the jet such as momentum flux, inflow condition, barrier surfaces and buoyancy flux can greatly influence jet growth rates and turbulent mixing. The effects of buoyancy, crossflow and barrier surfaces on the turbulent jet flows are discussed in the following subsections.

1.2.1 Buoyant Jet

Buoyant jet discharge has been studied for over a century, which resulted in extensive knowledge and theories about the nature of these releases. Several numerical and experimental researches have been formed on these theories which have led to considerable experimental data. These studies suggest that distinct flow regions are formed in a buoyant jet release, namely, initial strong jet region, weak jet region, advected line momentum puff region, advected plume region, and the advected thermal region (Jirka 2004). In each region, the flow behaviour is dominated by a set of independent flow parameters and overall behaviour of the flow is mostly independent of the initial region. Depending on the case being considered, some or all of these flow regions may occur but it should be noted that for any buoyant gas release the overall characteristics of the flow can be described by these distinct region. Froude number has been proved to be a good measure of ratio of momentum to buoyancy forces in subsonic discharge of flows in quiescent or relatively slow flowing fluid when the density difference between two fluids is considerable. The following relation was used to calculate Froude number:

$$Fr = U_{oc} / \left(gD\left(\rho_{\infty} - \rho_{jet} \right) / \rho_{j} \right)^{1/2} \qquad (1.1)$$

where Fr – Froude number, Dimensionless; U_{oc} – Jet centerline time-averaged exit velocity, m/s; g – acceleration due to gravity, m^2/s; D – Jet diameter, mm; ρ_∞ – Ambient air density, kg/m^3 and ρ_j – Jet exit density of helium, kg/m^3.

Large-scale ignited and unignited hydrogen leaks have been studied widely (e.g. (Chernyavsky, et al. 2010), (Schefer et al. 2006) and (Schefer et al. 2007)). In order to characterize the hydrogen discharge scenario in downstream of the leak and also to better understand extent of flammable gas envelope, these studies were extended to small unignited leaks in regions of momentum-dominated flows (high Froude numbers) and in flows were buoyancy forces are more pronounced (low Froude numbers). These slow leaks may take place in various small-scale hydrogen based systems with leaky fittings and O-rings seals or in low pressure electrolysers as well as in vents in storage hydrogen facilities. Schefer et al. (2008) described measurements of hydrogen dispersion in a laboratory-scale leak in cases of both momentum and buoyancy dominated regions using a turbulent jet positioned vertically and shooting upward for cases of various Froude numbers (Fr = 268, 152, 99 and 58) and concluded that for Froude numbers bigger than Fr = 286 buoyancy generated forces are small. They also concluded that hydrogen jets show similar behaviour as jets of helium and conventional hydrocarbon fuels. In the present study, helium was selected as the working fluid, because it is inert and its molecular weight is very close to the molecular weight of hydrogen.

1.2.2 Crossflow

The buoyant jet discharge flow configuration becomes more complicated by introducing a moving ambient which can be in the same direction of the discharge, opposite direction, perpendicular or at some intermediate angle. In all these cases, the flow near the release source is usually weakly advected and momentum fluxes are dominant. Farther downstream, the flow is strongly advected and the entrained ambient momentum flux dominates. Among these flow configurations, the crossflowing turbulent jet, in which a round jet is injected into a perpendicular fluid stream, is of particular interest, as it is representative, for instance, of the dispersion of hydrogen in a windy environment.

Part of this study focuses on dispersion of a buoyant, turbulent, round jet in a quiescent and crossflow at a wide range of Froude numbers. The crossflow was oriented perpendicular to the discharge in direction parallel to the buoyant forces. Schematic diagrams of the resulting vortical structures of the crossflowing jet and the corresponding coordinate system are illustrated in Figure 3.18. Introduction of a new downstream coordinate system along the jet was inevitable and was defined according to the procedure described in section 3.1.

Experimental evidence show that this kind of flow structure is extremely sensitive to the ratio of jet-to-crossflow momentum ($r^2 = \rho_j U_{oc}^2 / \rho_\infty v_\infty^2$), and the complexity of the resultant flow structure makes it difficult to draw general conclusions about the flow configuration (Su and Mungal 2004). In most cases, the initial momentum flux of the discharge determines whether a two-dimensional or a three-dimensional flow structure is created. The experimental data suggest that if the initial momentum flux acts in the

same plane as the buoyancy-generated and ambient entrained momentum flux, the resulting flow structure will have a two-dimensional trajectory (Kikkert 2006). The vortical structure of the turbulent crossflowing jet have been studied extensively, and many experiments have been conducted using different velocity ratios (r) spanned from 5 to 35 (Crabb, Durao and Whitelaw 1981). Detailed measurements of turbulence stresses were also reported for flows with r = 0.5, 1 and 2 (Andreopoulos and Rodi 1984), leading to the conclusion that the presence of a crossflowing ambient strongly affects the jet velocity profiles.

Off-center-plane measurements and the effects of different initial condition in crossflowing jet also point to the conclusion that the flow structure is very similar to that of pure jet in momentum-dominated region of the jet, and that the complex flow structure in the jet downstream is symmetric (Su and Mungal 2004). In present study, crossflow velocity was kept constant, and the resulting r values spanned from 0.6 to 11 for different Froude numbers considered.

1.2.3 Surface Effects

The other part of this study focuses on surface effects on a horizontal free jet flow. These jet flows are often called wall-jets. Shwarts et al. Cosart and Schwarz (1960) described the wall-jet as “a jet of fluid which impinges onto a wall at an angle from 0 to 90 degrees”. Launder and Rodi (1981) completed this definition and identified the wall jet as “a shear flow directed along a wall where, by virtue of the initially supplied momentum, at any station, the streamwise velocity over some region within the shear flow exceeds that of the free stream”. Here, a free turbulent jet dispersed parallel to a

wall surface with an impinging angle of 0 degrees. The jet flow was exhausted into still ambient environment and the wall surface was oriented under, above and at the side of the resultant flow. The velocity gradient between the jet flow and the ambient air creates a shear layer which develops in downstream locations as the ambient air entrains into the jet structure. Interaction between the jet flow and the wall surface also creates a boundary layer. As the flow develops, at some downstream location the jet shear layer and the wall boundary layer meet to produce a so called fully developed wall jet. Narasimha *et al*. (1973) suggested this downstream distance to be 30 times the distance from the wall to the nozzle. Schematic of a wall jet in vicinity of ground surface is shown in Figure 1.1.

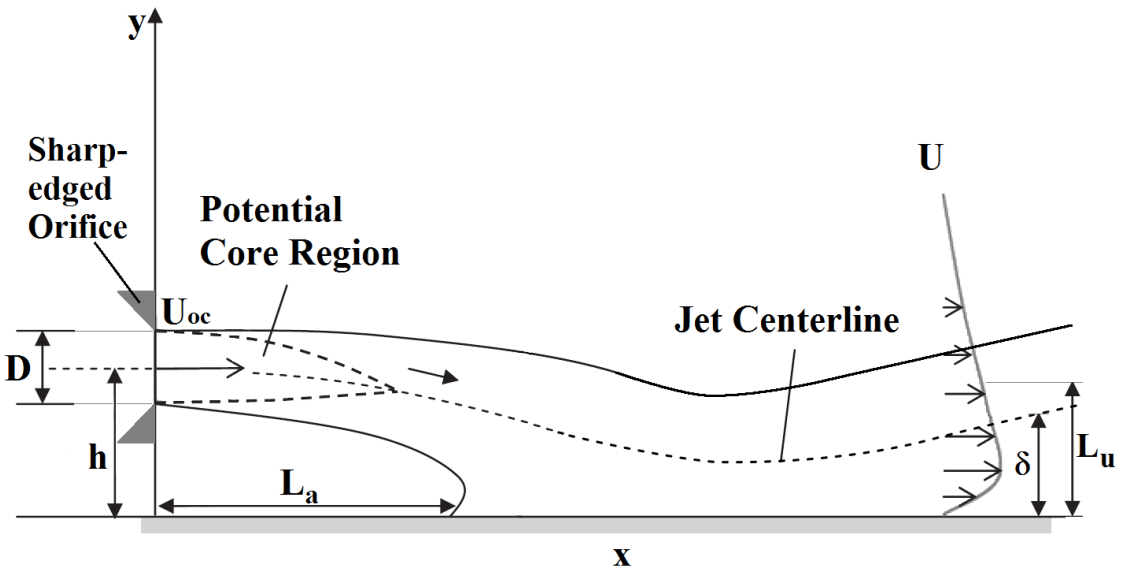

Figure 1.1 – Schematics of the wall jet flow.

In the figure, U_{oc} denotes the time-averaged nozzle exit velocity, h denotes the nozzle distance from the wall surface, L_u is the distance away from the wall surface at which the streamwise velocity decreases to half of maximum velocity (i.e. velocity along the centerline). In a fully developed wall jet, δ denotes the distance from the wall

surface to the point of maximum velocity and is also taken as the wall boundary layer thickness. As the wall jet propagates in downstream direction, the wall boundary layer thickness and L_u distance increase.

The structure of the wall-jet is considered to consist of an inner, an outer and a mixing layer. Cosart and Schwarz (1960) considered the inner layer of the a fully developed wall jet to be the distance between the wall surface and the point of streamwise maximum velocity at each downstream location. In early wall-jet studies (e.g. (Glauert 1956)) It has been reported that the inner layer velocity vary with classic one-seventh power of distance from the wall surface analogous to that of turbulent boundary layer. Later Wygnanski *et al.* (1992) reported some Reynolds number dependencies in scaling of wall-jet's inner layer. George *et al*. (2000) showed that the wall-jet behavior in inner layer is in fact to some extent similar to the classical turbulent boundary layer and it has a laminar sub-layer and a log law region. The detailed analysis of the inner layer does not fit to the scope of this study but it should be noted that the wall-jet's inner layer is similar to classical turbulent boundary layer with some differences.

The L_u length scale has been reported as the common scaling factor for the outer layer in a wall-jet structure (e.g. George *et al*. (2000)). The wall-jet's outer region could greatly affect the inner region and the structure of this inner layer is modified by the turbulence and entrainment from the outer layer (Schwarz and Cosart 1960). George *et al*. (2000) proposed a full similarity solution to wall jet flow structure at infinite Reynolds number which led to the appropriate scaling factor for both finite and infinite Reynolds number cases. These scaling factors were found to be velocity magnitude

along the jet centerline, U_c and half maximum velocity distance, L_u. Time-averaged velocity profiles tend to collapse while using the L_u length scale as the half velocity length in the upper half of the jet.

The mixing layer between the inner and outer layer of the fully developed wall jet structure is considered to be a very thin layer which separates these two layers from one another. The position of this mixing layer is defined as the location of the maximum streamwise time-averaged velocity at each downstream location and the mixing layer is identified by the jet centerline location.

The fundamental structures of wall jets are not two dimensional and wall jets are considered to exhibit pronounced three dimensional features. The shear layer created at the boundary of the jet flow and still air results in ambient entrainment which causes the jet to spread. As a result some of the jet's initial momentum is directed from the streamwise into the spanwise direction. This forces the velocity component in the spanwise direction to diverge from the nozzle centerline. Three-dimensionality and the interaction between the jet and the wall surface cause the wall jet growth rate to drop. The growth rate in wall jets are reported to be 30% slower comparing to free jets (Smith 2008).

The jet to surface attachment distance, L_a, is shown in the Figure 1.1. In order to find L_a theoretically, it has been assumed that the jet structure spreads symmetrically about the nozzle axis before the jet to surface attachment point. The width of a circular free jet can be calculated using Eqn. (3.7) (Kanury 1977). The nozzle centerline distance to the surface was used as the jet radius in order to find the downstream distance, x, at which the jet radius is equal to nozzle to surface distance. This point was

used as the theoretical jet to surface attachment point and is compared to the experimental values in chapter 3.4.

1.3 PARTICLE IMAGE VELOCIMETRY (PIV) FUNDAMENTALS

Velocity fields and consequently turbulence statistics and other flow physics for the cases considered herein are characterized using Particle Image Velocimetry (PIV). PIV is an optical method of flow visualization which can be used to measure the instantaneous velocity field of a small marked region of the fluid by monitoring the movement of markers. This technique has been developed from the early 1980's and has been adopted by many researchers due to its non-intrusive nature. It can be used on any kind of flow in liquid and gaseous state, moving or stationary and over a broad range of Reynolds numbers (Vogel 1994). PIV was used for various applications such as boundary layer studies, flows of jet or flow around an airfoil, vorticity analysis and etc. (Raffel, Willer and Kompenhans 2002).

In order to trace the resultant flow, particles are introduced into the flow as markers. The particles are usually solids in gases or liquids but can also be gaseous bubbles in liquids or liquid droplets. These particles are often called as seeding. Depending on the fluid under consideration, these particles should match the fluid properties and need to be neutrally buoyant and have a short response time to the fluid motion (Hinds 1999). Minimum flow interference can be achieved by careful selection of size and density of seeding particles. The particles motion is dominated by Stokes drag due to small sizes of particles (Hinds 1999). Stokes drag is a qualitative measure of how well the tracer particles follow the fluid streamlines with minimal interference and is given by:

$$St = \frac{\tau U}{L} = \frac{\rho d^2 C U}{18 \mu L}, \qquad (1.2)$$

where L and U are characteristic length and velocity of the flow respectively, C is a slip correction factor, τ – is relaxation time, which can be expressed as $\rho d^2 C / 18\mu$, where ρ and d are the density and typical diameter of the particle, μ is a dynamic viscosity of the fluid.

For $St>>1$, particles will continue in a straight line regardless of fluid streamline but for $St<<1$, particles will follow the fluid streamlines closely.

An instantaneous image of the marker particles in the jet in crossflow and the corresponding velocity field are shown in Figure 1.2.

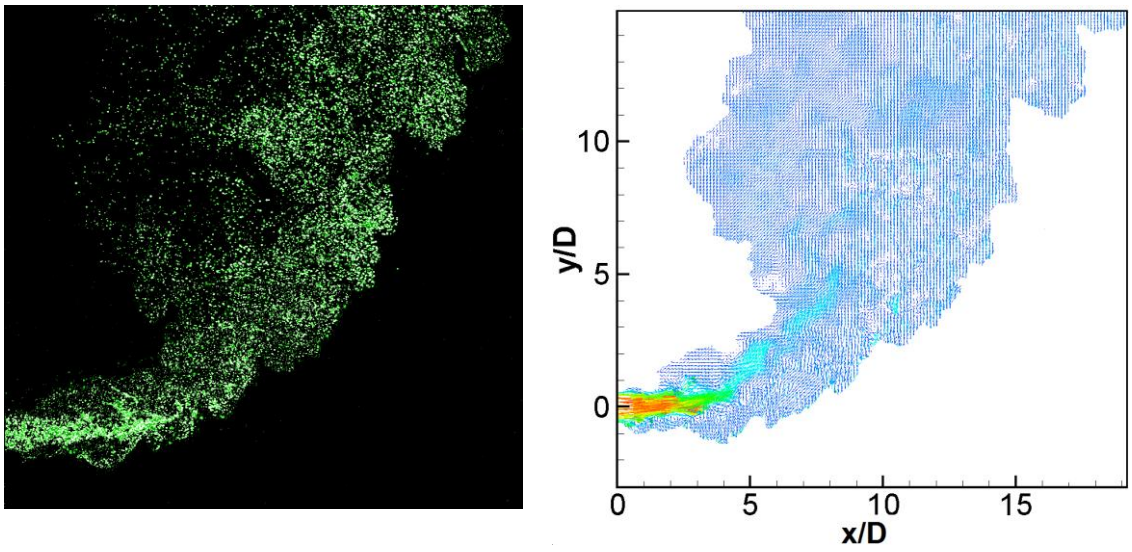

Figure 1.2 – PIV principles, Particles instantaneous image (Left), corresponding velocity field (Right).

The PIV velocity evaluation is performed by recording images of particles at two or more consequent time intervals. As can be seen in the above figure, all particles look alike which makes it impossible to follow a single particle in two consequent frames. Instead each single frame can be divided into smaller regions called Interrogation

Windows (IW). Each IW contains a group of particles which produce a somehow unique finger print. This particle pattern can be found in the consequent frame. By assuming constant velocity for all particles in an IW, particle displacements can be found by calculating the shift of IWs in a consequent frame. Knowing the exact time different between two frames and particle displacements, one can calculate the velocity vector for a group of particles in each IW.

In this study Planar or also called two-dimensional PIV was used. In this technique a pulsed light source is converted in to a light sheet which illuminated a two-dimensional cross-section of the flow field. By measuring the displacement of particles in *x*- and *y*-direction and by knowing the time interval between two images, corresponding velocity components can be calculated in each direction. A detailed overview of particle imaging techniques used in experimental fluid dynamics is given by Adrian (Adrian 1991).

As mentioned before, in order to calculate the velocity field, the displacement of a group of particles in two consequent frames should be monitored. A mathematical correlation procedure can be used for this purpose in order to find the most probable displacement of IWs. Many different methods have been used in literature for this purpose and among those Convolution filtering and Fast Fourier Transform (FFT) are the most popular in PIV analysis (Stamhuis 2006).

Convolution filtering is a close description of moving the IWs of the second image over the first image to find the most probable path. In this method a 2D probability density function of matching level of IWs in two subsequent frames is constructed using the summation of products of all pixel values of IWs in both images.

In FFT method, each IW is transformed into a complex domain. Complex conjugate production of these IWs for subsequent frames is then performed and the resulting image is transformed back which will show a 2D probability density function of level of matching between to IWs. This method is also called cross-correlation method as it provides a spatial cross-correlation between two subsequent frames (Utami, Blackwelder and Ueno 1991). The cross-correlation function, $Q(m,n)$, for two sample regions $f(m,n)$ and $g(m,n)$ can be presented as (Raffel, Willer and Kompenhans 2002):

$$Q(m,n)=\frac{\sum_{m=-\infty}^{\infty}\sum_{n=-\infty}^{\infty} f(m,n)\,g(m+x,n+y)}{\sum_{m=-\infty}^{\infty}\sum_{n=-\infty}^{\infty} f(m,n)\sum_{m=-\infty}^{\infty}\sum_{n=-\infty}^{\infty} g(m,n)}, \tag{1.3}$$

Where for an IW with m and n coordinates, f and g denote the image intensity distribution of the first and second frame and x and y are pixel offsets between two frames.

If all the particles in IW of the second frame match their corresponding spatially shifted particles in the first frame, the value of cross-correlation function approaches unity (Willert and Gharib 1991). The flowchart of the cross-correlation PIV procedure is shown in Figure 1.3. The value of the cross-correlation function is maximum if the most probable displacement of a group of particles is found in the second frame.

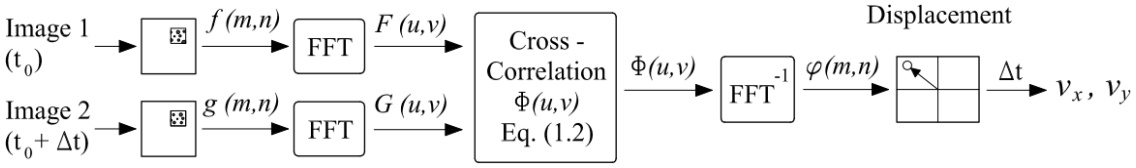

Figure 1.3 – PIV cross-correlation flowchart.

Both convolution filtering and FFT methods give comparable results but FFT is the preferable choice while considering turbulent flows since it provides faster calculation. More detailed information about the cross-correlation method and peak finding procedure can be found in (Raffel, Willer and Kompenhans 2002).

Although FFT approach offers a shorter calculation time, it has also some drawbacks. Firstly, the maximum particle displacement magnitude is limited by the Nyquist criterion associated with the Fourier transform. Secondly, FFT correlation can be only implemented with a square base-2 dimension (i.e.64×64).

To reduce the signal to noise ratio in the correlation algorithm and to improve the spatial resolution of resultant vector field, two noise reduction techniques was used. In flows with high velocity gradients, particles in a particular IW may exit the interrogation region in the subsequent frame. In order to address this issue the adaptive multi-pass technique (Westerweel 1997) was used which was done by offsetting the IW in the second frame of an image pair according to the mean displacement vector. This is an iterative process and it involves decreasing the IW sizes (i.e. 64×64 to 32×32 and finally to 16×16 pixels). After each multi-pass process a vector filtering and smoothing algorithm was used to harmonize the resultant vectors with neighbouring values and also to fill the empty spaces by bilinear interpolation of neighbour vectors.

The second correlation noise reduction technique was to ensure the integrity of the calculated cross-correlation peaks by overlapping neighbouring IWs. The IW overlapping was first introduced by (Hart 2000) in which the overlapping regions are multiplied to amplify the common correlation peaks and to damp the noise peaks. This

also increases the special resolution of the final resultant velocity field. In this study 50% IW overlap were employed.

To interpret the resultant velocity field, Reynolds decomposition procedure was used in present study. In order to perform turbulent analysis using Reynolds decomposition technique, appropriate inter-frame frequency should be implemented. For buoyant turbulent jet analysis the imaging rate of 5Hz was reported to provide the appropriate spacing in time for acquisition of random samples for average turbulence statistics (Chernyavsky, et al. 2010). A set of at least 300 images was used to calculate velocity vectors (<u> and <v>), out-of-plane vorticity, <ω_z>, root-mean-square (rms) of the velocity component fluctuations, and Reynolds stresses. Taking N as the total numbers of images, definitions of above time-averaged values are as follows (Velikorodny 2009):

Time-averaged velocity components:

$$< u, v >= \frac{1}{N}\sum_{n=1}^{N}(u_n(x,y), v_n(x,y)) \tag{1.4}$$

Time-averaged vorticity:

$$< \omega >= \frac{1}{N}\sum_{n=1}^{N}\omega_n(x,y) \tag{1.5}$$

Root-mean-square of u-velocity fluctuation:

$$u_{rms} = \left\{ \frac{1}{N}\sum_{n=1}^{N}\left[u_n(x,y) - < u(x,y) >\right]^2 \right\}^{1/2} \tag{1.6}$$

Root-mean-square of v-velocity fluctuation:

$$v_{rms} = \left\{ \frac{1}{N} \sum_{n=1}^{N} \left[v_n(x,y) - < v(x,y) > \right]^2 \right\}^{1/2} \tag{1.7}$$

Averaged value of Reynolds stress correlation

$$< u'v' > = \frac{1}{N} \sum_{n=1}^{N} \left[u_n(x,y) - < u(x,y) > \right] \left[v_n(x,y) - < v(x,y) > \right] \tag{1.8}$$

Similar relations to (1.8) can be written for other components of Reynolds normal stresses.

The PIV setup used in current study together with detailed information about the experimental setup is presented in Chapter 2 of this thesis.

1.4 SCOPE AND OBJECTIVES

For hydrogen safety considerations, identification of the size of hazardous zones and the extent of the flammable envelope are the key parameters in development of safety standards. The development of the jet mixing layer and downstream evolution of the resultant flow is of the particular importance in understanding of the flammable region. It has been observed that presence of strong buoyancy forces greatly influence the velocity decay rates and the centerline extent of the turbulent jets in the transverse direction. (Hourri, Angers and Benard 2009) reported that presence of strong buoyancy forces towards the end of the flammable cloud reduces the centerline extent. On the other hand the extent of the hazardous zone in the transverse direction was increased.

Velocity decay rates and the mixing characteristics of the jet discharges in moving ambient was observed to be strongly dependent on the ratio of the jet to crossflow momentum fluxes. The overall jet width and consequently the potential hazardous region in the jet center-plane was asymmetric and greatly dependent on the value of this

ratio. In addition the velocity decay rates and the turbulence quantities of jets in crossflow suggested the vertical growth and three dimensionality of the resultant flow which can potentially increase the flammable extent of the resultant hydrogen cloud.

For jet flows in proximity to surface, the maximum extent of the resultant flow was increased. Particular attention was given to the effects of the surface orientation and it was observed that the closer the surface to the jet centerline, the bigger the impact is on the extent of the resultant flow and the potential hazardous zone. (Hourri, Angers and Benard 2009) has drawn similar conclusion by considering the surface orientation on the flammable extent of the hydrogen leakage scenarios using CFD. The physical characteristics of jet flows in proximity to surface suggested the asymmetric three dimensional extension of the jet over adjacent surface. The effect of strong buoyancy forces in amplifying and reducing the effect of the surface on the overall extent of the resultant jet was also evident.

The lack of the reliable experimental data base (if any) in quantification of effects of buoyancy, crossflow and adjacent surface on the flammable extent of the hydrogen leakage scenarios is noticeable. Quantification of resultant velocity field and turbulent quantities on the overall downstream evolution of the jet and correlation of the velocity and concentrations field is a necessary step in development of the safety standards.

This study focuses on the investigation of jets produced by a high-velocity gas entering a quiescent and moving ambient which emulates the unintended hydrogen leak from a high pressure system in various different conditions, a possible scenario for fuel cell vehicles and hydrogen stations. This type of flow is usually turbulent, unsteady and can have significant compressibility effects. In order to achieve a better understanding

of the physics associated with the development of a turbulent jet, quantitative flow visualization was accomplished by employing digital particle image velocimetry (DPIV).

This work follows two primary objectives. The first objective is to experimentally characterize the effects of buoyancy, crossflow and proximity to surfaces on hydrogen dispersion with the aim of better understanding of the flow structure and flammable envelopes for uncontrolled leaks with different flow rates. Over the recent years, hydrogen leakage scenarios have been a subject of many CFD studies (e.g. (Chernyavsky, et al. 2010)) and a necessary step towards validation and development of these CFD models is to have a detailed well defined experimental database. So the second objective is to provide a well-defined quantitative database that can be used for future concentration measurements and also to validate CFD models related to hydrogen release scenarios.

1.5 THESIS OVERVIEW

The overview of different experimental setups and flow conditions used in this study are given in Chapter 2 of this thesis. Detailed design procedure of the crossflow assembly and its outflow velocity and turbulence intensity measurements are also included in that chapter. Chapter 2 contains detailed information about the sharp-edged orifice inflow configuration and details on flow conditions, initial velocity and turbulence intensities, different surface configurations for dispersion cases in the vicinity of a barrier, and the PIV setup of the experiment.

Chapter 3 presents the results and discussions of different cases considered in this work. Flow visualizations and associated characteristics of the resultant jet structure for the cases of free jets, jet in crossflow and surface effects on jets are presented. The buoyancy effects in free jet flows are discussed in detail for a range of Froude numbers in an attempt to distinguish the buoyancy and momentum dominated regions in resultant flow structures. Afterwards, the effects of the crossflow assembly with a fixed velocity are investigated in the same range of Froude numbers. Detailed discussions of the resultant flow regions and different scaling factors used in crossflowing jets are presented in that chapter. The final section of Chapter 3 focuses on horizontal jet dispersions in the vicinity of a barrier. Results of three different surface configurations emulating ground, ceiling and vertical wall are also given in that chapter. Conclusions and the recommendations for future work are presented in Chapter 4.

CHAPTER 2

EXPERIMENTAL SYSTEM AND TECHNIQUES

2.1 INFLOW CONFIGURATION

According to Townsend (1996), turbulent flows show a self-similarity when they become asymptotically independent of initial condition. However, George (1989) showed analytically that the entire turbulent flow is influenced by initial conditions and concluded that different initial conditions will lead to different self-similar states in the downstream regions. Three different nozzle configurations, commonly used in turbulent flow studies using round jets are smoothly contracting (contoured) nozzles, long pipes, and orifice plates. Among those, contoured nozzles have been widely used in most fundamental studies (e.g. (Crow and Champagne 1971) and (Becker, Hottal and Williams 1967)), because they produce a fairly uniform velocity profiles, also referred to as top-hat profiles, with low mean initial turbulence intensity ($<u'>(y)/U_{oc}$) of about 0.5% except at edges ($y > 0.45D$) (Smith, et al. 2004). This property of contoured nozzles makes them ideal for computational analysis. A long pipe located upstream of the circular orifice has also been considered widely in numerous studies (e.g. (Lockwood and Moneib 1980)). Although the exit velocity profile of circular jets issued by pipes is not uniform, the lower manufacturing cost and simplicity made long pipe inlets a common choice in fluid dynamics experiments. These pipes are usually manufactured long enough to produce a fully developed turbulent boundary layer at the

exit and their mean initial turbulent intensity has been reported to be between 3 to 9.5% (Smith, et al. 2004).

Limited information is available regarding circular jets originating from sharp-edged plate nozzles. This inflow configuration is characterized by a relatively complex initial velocity profile in near-field flow structure. However, it can be argued that sharp-edged orifice plates emulate unintended hydrogen leakage scenarios more realistically than the contoured nozzle and the long pipe inlet configurations. A detailed comparison between contoured nozzle, long pipe and sharp-edged plate inflow configurations and the corresponding flow structures may be found in (Smith, et al. 2004) and (Mi, Nathan and Nobes 2001). Briefly, in a sharp-edged orifice, the flow on the upstream side of the nozzle undergoes a sudden contraction which causes an initial separation in the fluid and increases mean initial turbulence intensity subsequently. This upstream lateral contraction forces flow streamlines to initially converge towards the jet exit and suddenly expand in the jet near-field very close to the nozzle exit which is called “vena contracta”. The presence of the vena contracta phenomenon causes a sudden local pressure drop and leads to a local maximum in the centerline mean velocity profile, which is one of the characteristics of a sharp-edged nozzle. It has been reported by Quinn (Quinn 1992) that this local velocity maximum is 30% higher than centerline velocity value at nozzle exit. Saddle-back mean velocity profile is another characteristic of the sharp-edged orifice, and the mean initial turbulence intensity is reported to be between corresponding values in contoured and pipe nozzles (Smith, et al. 2004). The centerline mean velocity decays faster as a result of the sudden expansion and increased entrainment as the jet travels downstream.

In this study, experiments were performed using a jet apparatus consisting of a honeycomb settling chamber and a sharp-edged orifice with the edge angle of 45º and exit nozzle diameter (*D*) of 2*mm* (see Figure 2.1).

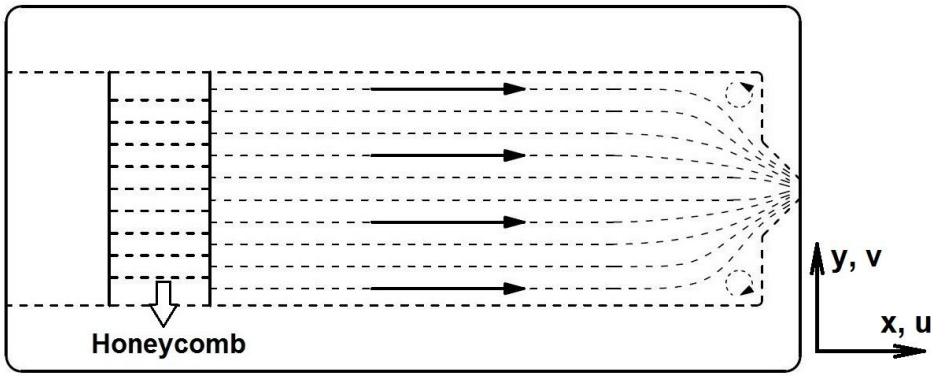

Figure 2.1 – Sharp-edged nozzle schematic

To have a better understanding of the sharp-edged orifice inflow configuration, time-averaged velocity profiles together with corresponding root-mean-square values were measured using PIV.

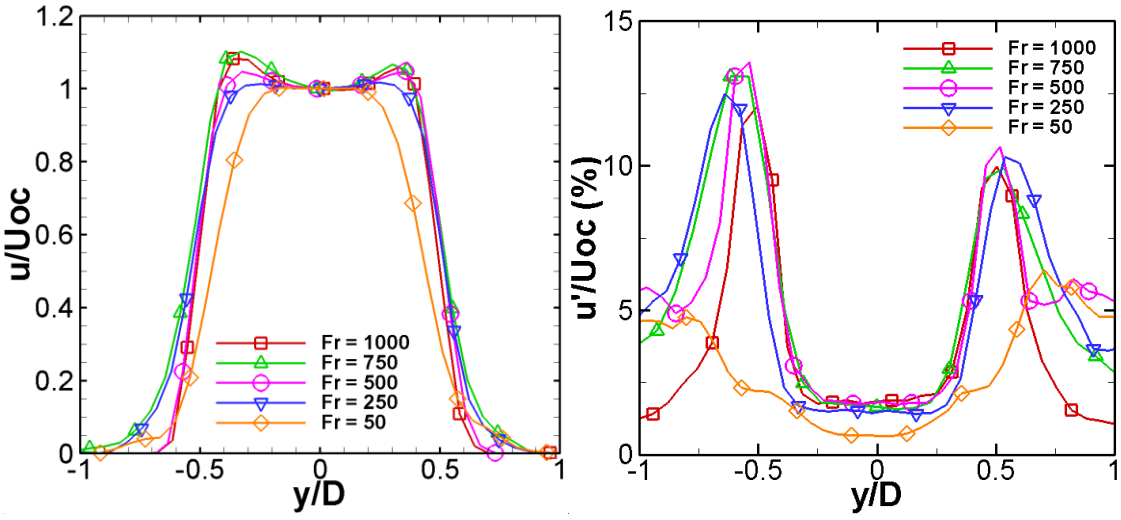

Figure 2.2 – Initial normalized radial mean velocity profile (left) and normalized radial rms values (right)

Measurements were performed at 0.1D downstream of the nozzle exit for the range of Froude numbers considered in this work. The initial mean normalized radial velocity profiles together with corresponding normalized rms values are shown in Figure 2.2.

For Fr = 50, a top-hat initial velocity profile with a very low turbulence intensity were observed which is related to laminar nature of this flow condition and is discussed in more detail in following sections. For Fr > 250, the increase in the Froude number lad to a more pronounced saddle-back initial velocity profile as a result of the higher initial momentum which moved the point of the vena-contracta further downstream and led to a higher peak in centerline velocity profile. On the other hand, decreasing the Froude number moved the vena-contracta point towards the jet exit, which led to a top-hat initial velocity profile and lower initial turbulent intensity. The initial turbulence intensity of approximately 2.5% was measure for Fr > 250. The data are in a good agreement with the results reported in (Mi, Nathan and Nobes 2001).

2.2 CROSSFLOW APPARATUS

One of the main objectives of the current study is to document the effects of a moving ambient on the buoyant jet discharge. The jet apparatus was oriented horizontally in order to capture the buoyant characteristics of the flow. The crossflow assembly was positioned to amplify the jet flow in the direction where the buoyancy effects were dominant. A small blower-type wind tunnel was designed and used for this purpose. Schematics of the crossflow apparatus is give in Figure 2.3.

Four identical fans with volumetric flow rate of 112 Cubic Feet per Minute (CFM) have been fed to a cubic box with side of 18cm. The upper side of the box was covered

with a 62*mm* thick hexagonal honey comb structure with cell side length of 2.5*mm* and wall thickness of 0.1*mm*. The equivalent hydraulic diameter of honeycomb cells where calculated to be 3.7*mm*.

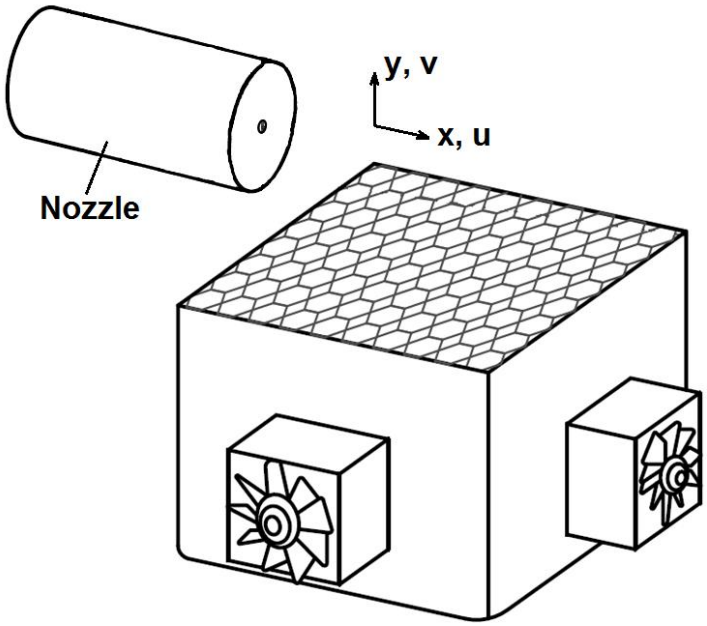

Figure 2.3 – schematics of the crossflow apparatus

Isentropic turbulence distance downstream of the honeycomb structure was calculated to be approximately 10*cm* taking the center of the box as the point of turbulence generation (Mikhailova, Repik and Sosedko 1994). All fans were connected to a variable voltage power supply unit and were operated with 24*V*. To monitor the uniformity of the resultant velocity field from the crossflow apparatus, PIV technique was used. The resultant crossflow velocity magnitude was measured to be approximately 11*m/s* with the maximum of 4% variation throughout the domain. The turbulence intensity generated by the blower at the nozzle tip was measured to be approximately 2% of the time-averaged crossflow velocity.

2.3 EXPERIMENTAL APPARATUS

The jet apparatus was positioned in a horizontal manner in order to capture the buoyant characteristics of the resultant jet flow. To ease the future modeling and to minimize the wake produced by the nozzle apparatus in crossflow cases, the jet was issued from the wall with $24cm \times 26cm$ dimension in (y, z) plane. The nozzle centered the wall in z direction at $10cm$ above the honeycomb surface. The picture of the experimental apparatus for the cases of free and crossflowing jets is shown in Figure 2.4. The green cloud in the following figure is the illuminated particles. It should be noted that crossflow apparatus is not in operation in this figure.

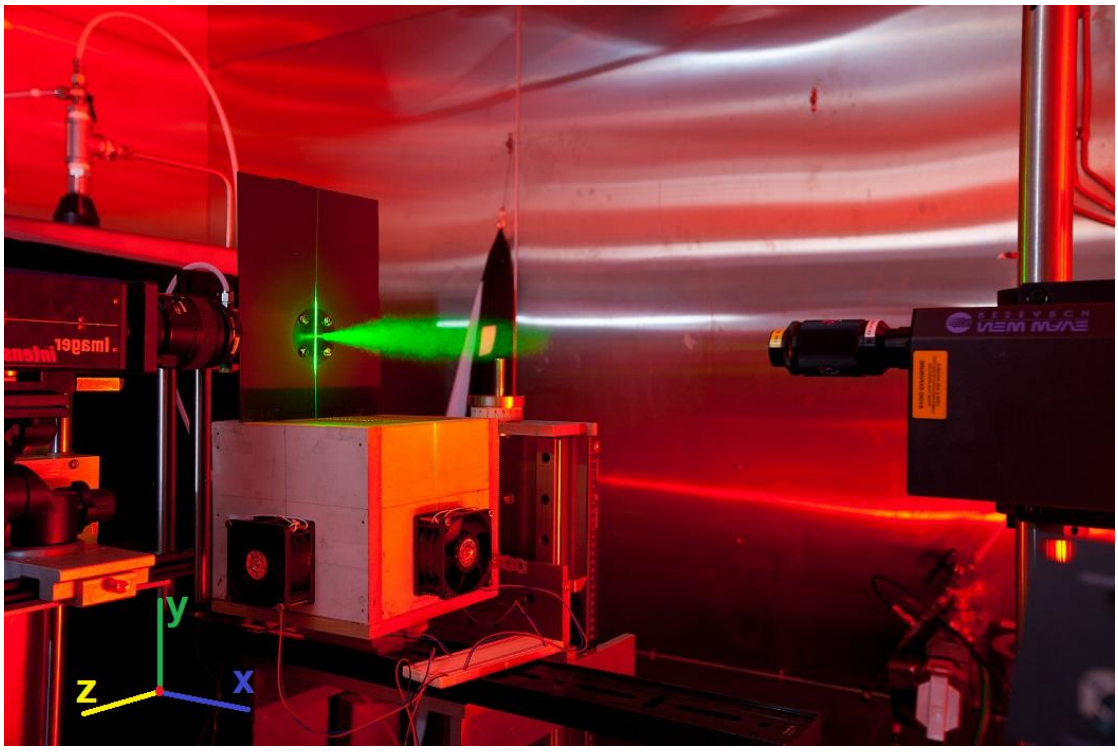

Figure 2.4 – Experimental apparatus

For the jet flows adjacent to a barrier, the same configuration was used with a surface positioned close to the nozzle. The jet to surface orientations for these cases is

shown in Figure 2.5. Detailed schematics of experimental setup for different cases considered herein are given in Chapter 3 of this thesis.

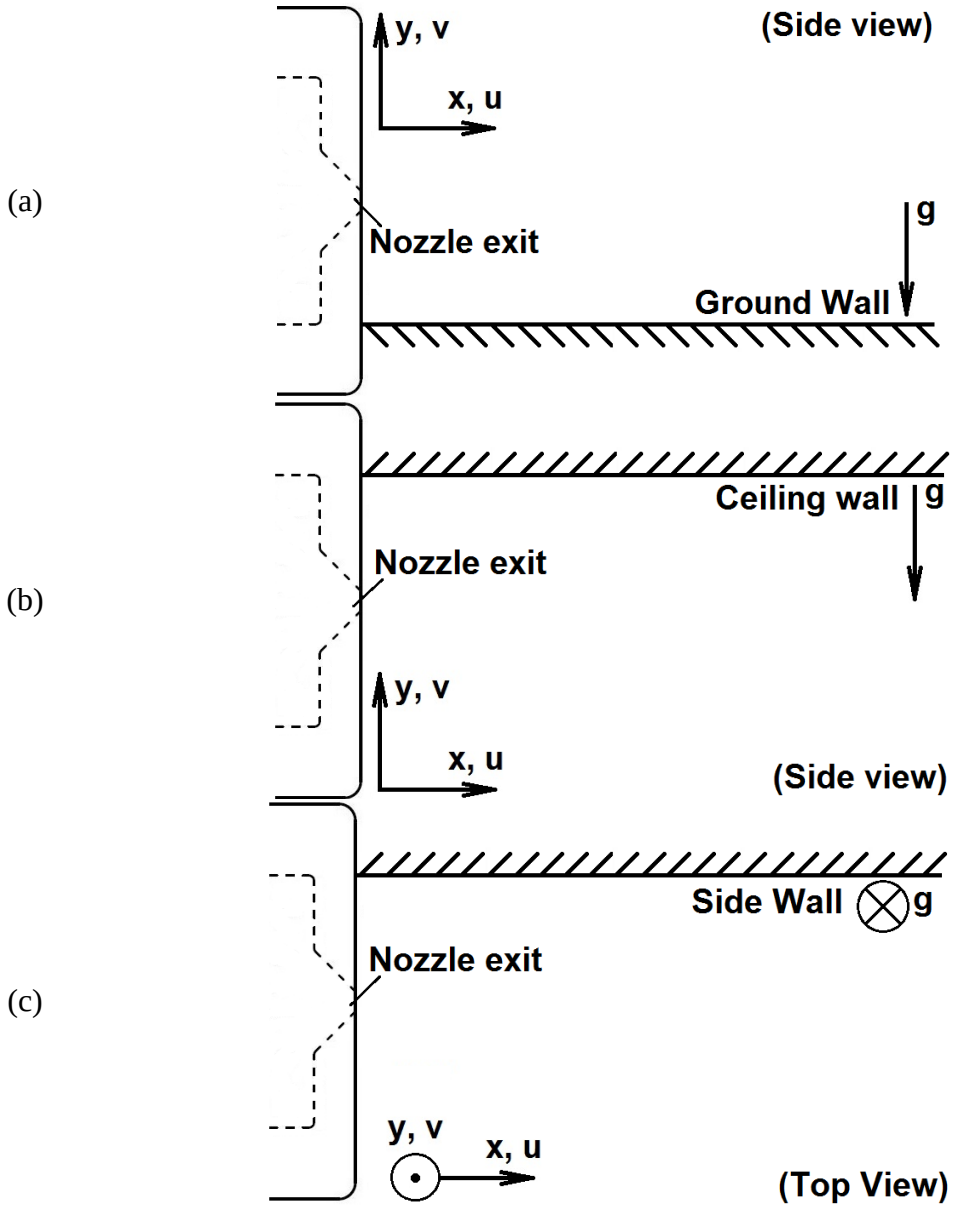

Figure 2.5 – Jet and surface orientation for wall effect cases, (a) ground, (b) ceiling and (c) vertical wall orientations

The exit nozzle diameter was 2*mm* (D) and helium were supplied by a T-cylinder monitored through mass flow controllers and exhausted horizontally to the quiescent, crossflow and adjacent to a surface for free, crossflow and wall-jet cases respectively.

Table 2-1 represents the cases and flow conditions that were considered herein. Volumetric flow rates together with centerline exit velocity of the jet flow are also given in this table for the considered geometry. A wide range of Froude numbers (i.e. *Fr=50, 250, 500, 750* and *1000*) were considered and experimental conditions were set accordingly. Resultant experimental Froude numbers and the corresponding Reynolds numbers at jet exit were calculated considering the jet geometry and are shown in Table 2-1. It should be noted that flow structure in a turbulent jet ranges from laminar (*Re* < 500) to transitional (885 < *Re* < 1360) to fully turbulent (*Re* > 2384).

Table 2-1. Flow conditions

Case	Q (lpm – H_2)	U_{oc} (m/s)	*Fr*	*Re*
1	64.4	318.33	~1000	5263
2	43.4	248.98	~750	4196
3	35.7	185.23	~500	3121
4	21	94.56	~250	1593
5	12	18.86	~50	317
Helium density and viscosity are 0.166 kg/m^3 and 1.97E-05 *kg/ms*, respectively				

It should be noted that the resultant Froude numbers for the cases presented in the table are shown as the approximate value. This was because of centerline velocity jump in the potential core area due to the sharp-edged orifice configuration which is discussed in previous sections. So the equivalent Froude numbers were approximated by averaging the nozzle exit and maximum values in the potential core region.

All properties are referenced to the room temperature T = 22ºC (±1) and the pressure P = 100kPa (±0.5). It has been reported that at the high Froude numbers (*Fr* > 1000), jet flows are momentum-dominated, while for the low Froude numbers, buoyancy forces are dominant. All discharges with intermediate Froude numbers (1000>*Fr*>50), are influenced by both the initial momentum of the jet and the

buoyancy forces generated by the relative density differences between the jet and the ambient gas (Schefer, Houf and Williams 2008). Also, it has been reported that for Froude numbers bigger than Fr >286 buoyancy forces are negligible (Schefer, Houf and Williams 2008). In the present study, helium was used as the working fluid to simulate the hydrogen dispersion; however, the density of hydrogen is approximately one half of helium density under the same conditions. Therefore, the effect of the Froude number on the buoyancy is expected to be more pronounced in the case of the hydrogen dispersion.

2.4 PARTICLE IMAGE VELOCIMETRY

Quantitative flow visualization was conducted using PIV. The PIV technique was used to record and calculate the 2D velocity field. The PIV setup in this work consisted of a laser which provided the illumination, seeding particles served as tracers and a charge-coupled device (CCD) camera which was used to capture the images of illuminated particles.

Detailed background information about PIV may be found in Chapter 1 of this thesis and also in (Adrian 1991). The isometric view of the PIV setup for the free jet flow is shown in Figure 2.6. Same PIV setup configuration was use in cases of jet in crossflow and jet flows adjacent to a surface.

The helium flow was seeded with olive oil droplets (LaVision Aerosol Generator) serving as tracers, with a typical diameter of approximately 1μm. The corresponding Stokes number was calculated using (1.2) to be approximately 2.45E-02. The illuminated olive oil particles are shown in Figure 2.7.

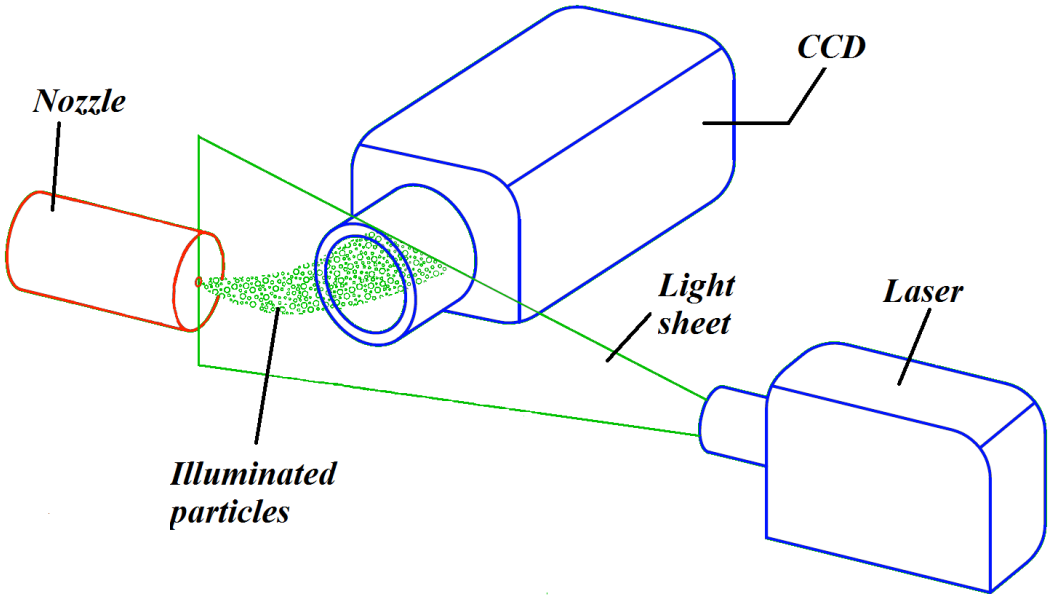

Figure 2.6 – Schematics of the PIV setup

Dual head Nd: YAG laser was used to illuminate the flow tracers. The laser beam was transformed to a light sheet with approximate thickness of 500μm. A high resolution CCD camera was positioned perpendicular to the light sheet in order to capture the scattered light from the illuminated particles. The camera had a total of 1376 × 1040 pixels and was equipped with a 60-mm lens. The field of view of the camera corresponded to a 21.5×15mm window. The imaging planes were parallel to the centre-plane of the jet in areas extended from the jet exit to far-field region. For calculation of the velocity field, the image area was divided into interrogation windows that were analyzed individually to yield local velocity values in the corresponding area.

The maximum framing rate of the camera was 15Hz, corresponding to 7.5 cross-correlated PIV images per second. Due to data transfer limitations this rate was further reduced to 4.9Hz. Lavision DaVis 7.1 software was used to calculate global instantaneous flow velocity fields of acquired images followed by a multi-pass spatial resolution improvement process with incremental decrease of interrogation window

size from 32 × 32 pixels to 16 × 16 pixels and with a 50% overlap in the *x*- and *y*-directions. The velocity vectors were calculated using the cross-correlation method. In the post-processing stage, the erroneous vectors were replaced by interpolation which resulted in bias error of approximately 2%. The final spatial resolution of 256 × 256μm and the temporal resolution of 4.9 Hz of the PIV image sequence were appropriate for capturing random samples for the calculation of the averaged turbulence statistics. Depending on the complexity of the resultant flow structure a total of 200 to 400 images were acquired for each case under consideration.

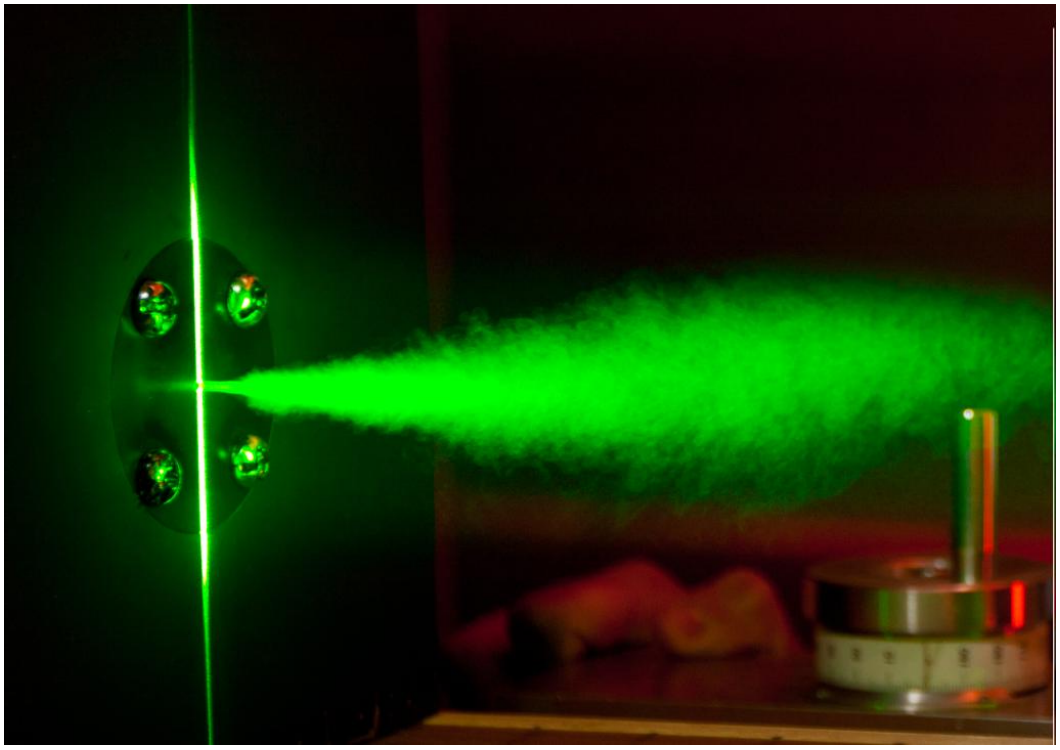

Figure 2.7 – Illuminated particles

Escaping of the seeding particles from the imaging plane due to the random un wanted oscillations and wobbling in the jet flow or as a result of the 3D vertical structure of the jet flow in some cases, resulted in a bias error in PIV measurements.

This effect can be minimized by increasing the thickness of the imaging planes in some cases or by increasing the total number of images. The amount of the particles escaping the imaging plane can be estimated by the means of the secondary peaks on the cross-correlation function. However, this is a computationally intensive procedure and was not implemented in this study.

The two major classes of uncertainties associated with PIV are: systematic error and root-mean-square error (Huang, Dabiri and Gharib 1997). The systematic error is due to implementation of cross-correlation and peak finding algorithm and root-mean-square errors generally are attributed to the noise in correlation domain. The vector loss due to filtration of spurious vectors was less than 2%. In addition precision errors associated with the location of correlation peak in particle displacement identification, accounted for uncertainty of less than 2%. The total uncertainty of the calculated velocity field was less than 4%.

CHAPTER 3

RESULTS AND DISCUSSION

This section presents the results of the various test cases considered herein. Definition of jet centerline coordinate system is included together with the results and discussions for free horizontal jet cases which served as the basis for crossflow and surface effect analysis.

3.1 JET CENTERLINE IDENTIFICATION

Due to the bifurcated structure of the resultant jet flow in most cases considered in this study, jet centerline deviated from the axis of the orifice. This deviation was more pronounced in low Froude number free jet flows, jet in crossflow and some discharges adjacent the barrier. In momentum dominated cases (i.e. high Froude numbers) for free jet flows and also in flow discharges far away from the surface, in surface effect scenarios, this deviation was negligible. Deviation of the jet centerline from the nozzle axis resulted in a more complex flow structure and required the use of a new coordinate system which reflected the downstream evolution of the flow. Schematic diagram of a possible flow structure of such case is illustrated in Figure 3.1. Given the knowledge of the flow evolution at downstream locations, the downstream distance, *s*, was measured along the jet centerline and *n* was defined as the vector normal to it. The (*s*, *n*)

coordinate system was related to the Cartesian coordinate system by rotating the (x, y) plane through the angle α about the z-axis.

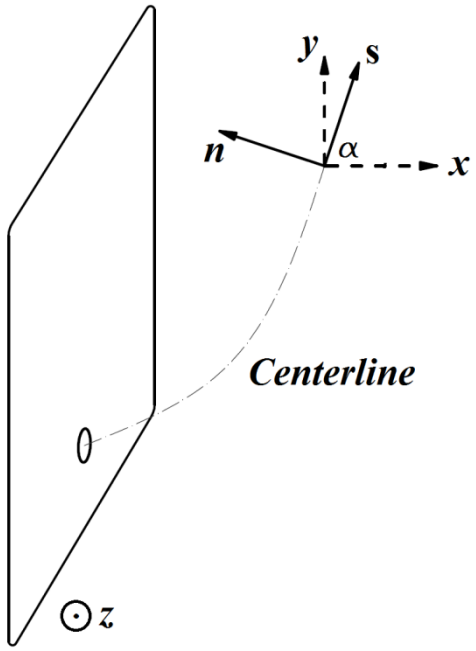

Figure 3.1 – The jet and the Cartesian coordinate system.

The centerline of the jet was originated in the center of the nozzle and was identified by fitting least-squares curve of the function expressed in Eqn (3.1), to the time-averaged velocity field trough locus of points of maximum velocity along the entire domain of consideration.

$$Y = AX^{\beta}, \tag{3.1}$$

Where A and β are constants and were evaluated for each case accordingly.

The procedure of finding these local maximum points was different for each case and a MATLAB code was developed for this purpose. For jet discharge in a uniform crossflow, these local maximum points were defined in a systematic manner by first determining the points of maximum time-averaged velocity magnitude (i.e. $<|\boldsymbol{U}|>$) along the x-direction in jet near-field region. At the jet far-field location the points of

maximum crossflow-subtracted velocity magnitude (i.e. $<|\boldsymbol{U}-v_\infty|>$) along the *y*-direction were considered. It should be noted that the *x*-direction was taken to be parallel to the nozzle center axis and the *y*-direction represented the direction of the crossflow. However, for the free jet discharge in quiescent ambient and also the jet discharge near a surface, the local maximum points of the velocity magnitude were considered in both *x*- and *y*-directions. After finding the tentative centerline by fitting a least square fit along these points of maximum velocity, the velocity values in the direction normal to the centerline were identified at each point and were compared to the centerline values. This was done in order to ensure that the identified values were also the maximum velocity values in profiles normal to the centerline.

Figure 3.2 represents the points of local maximum for the jet discharge in crossflow for Froude number 1000 and the corresponding jet centerline representation as an example. The solid black line is least squares fit to the data.

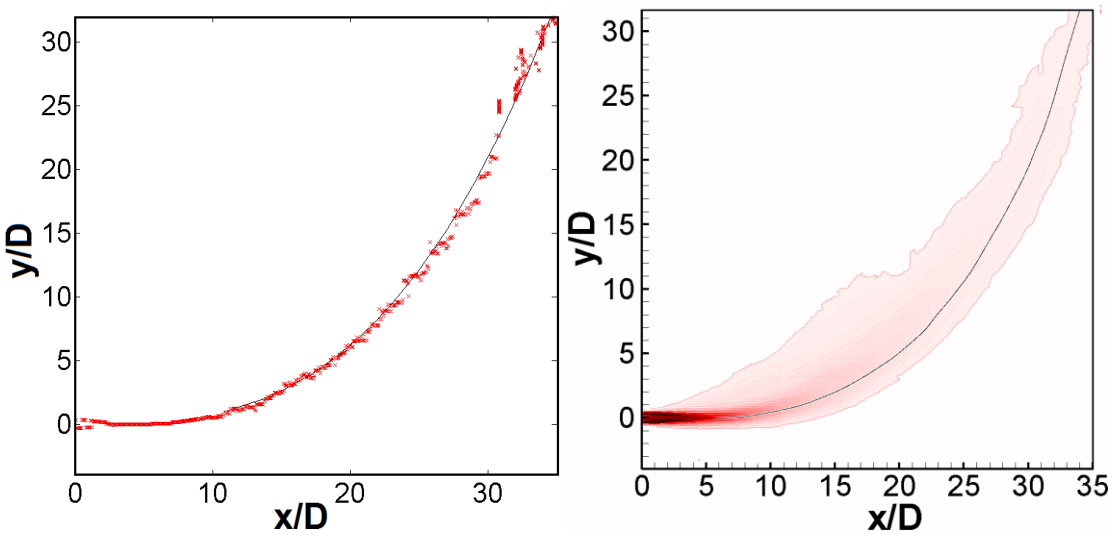

Figure 3.2 – Local maxima in the normalized time-averaged velocity field (left); jet centerline (right) *Fr=1000*.

After identification of the jet centerline, the resultant jet coordinate system (*s*, *n*) was transformed to the Cartesian coordinate system using a 2D rotational matrix with an angle α (see Figure 3.1) about the *z*-axis at each downstream location.

3.2 FREE HORIZONTAL JETS

Physical characteristics of the horizontal dispersion scenario of the round turbulent jet for a wide range of Froude numbers (i.e. *Fr = 1000, 750, 500, 250* and *50*) are presented in this section. The schematic of the experimental setup for free jet flows is illustrated in Figure 3.3.

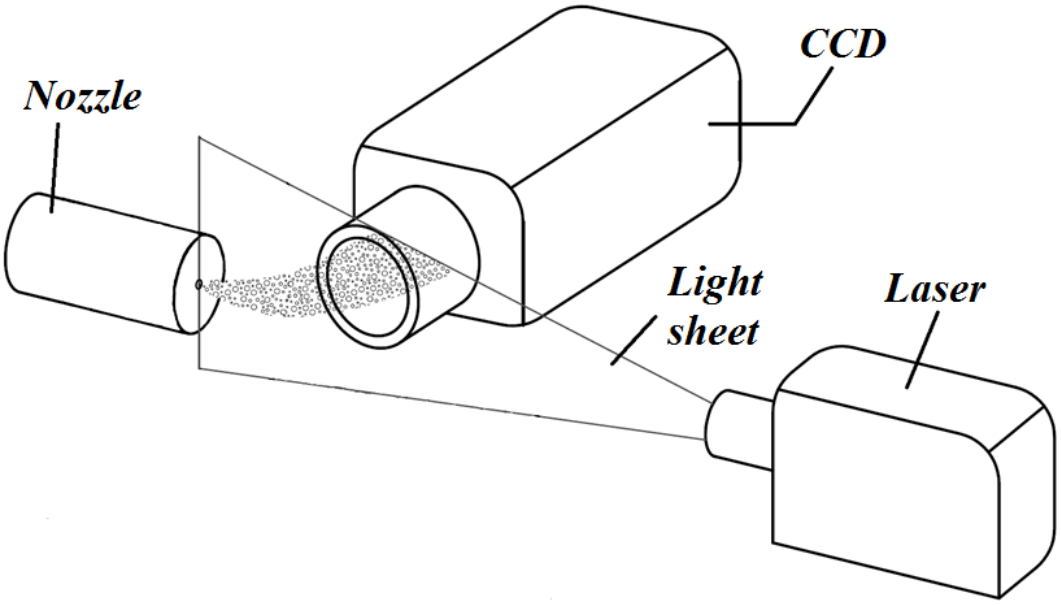

Figure 3.3 – Schematic of the experimental setup for free horizontal jet cases.

3.2.1 Jet Centerline

Jet centerlines corresponding to different cases considered herein are presented in Figure 3.4. At high Froude numbers (i.e. *Fr* > 250), effects of buoyancy were negligible, and the jet centerlines followed an almost straight pass with no deviation.

However, at low Froude numbers (i.e. $Fr \leq 250$), jet structure was divided into momentum and buoyancy dominated regions in the jet near- and the far-field regions, respectively.

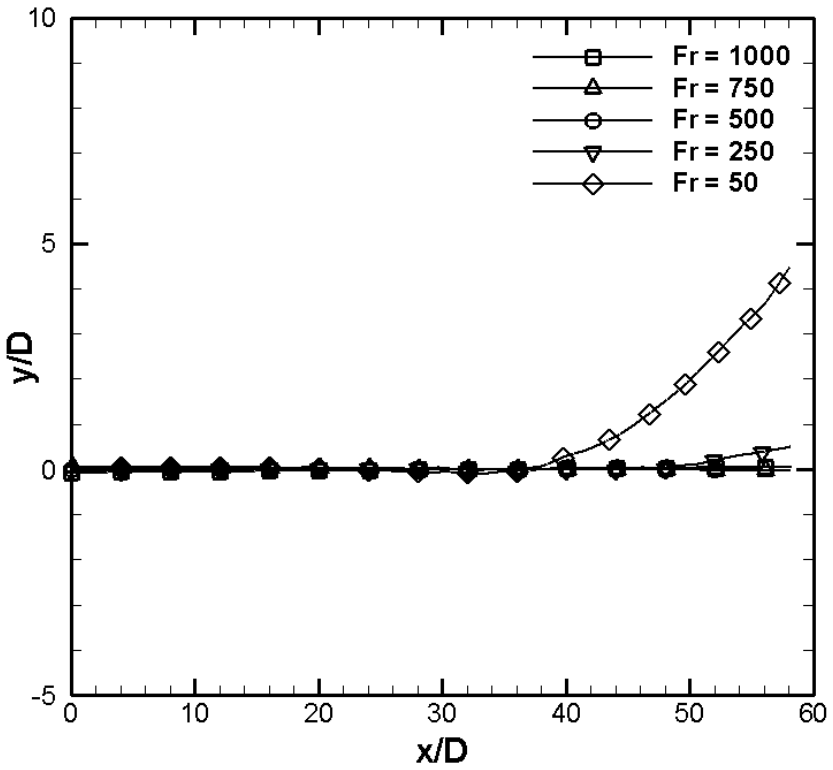

Figure 3.4 – Jet centerlines representations for free jet cases.

The first effects of buoyancy were observed at $Fr = 250$ at $x \approx 45D$ where the jet centerline shifted towards the $+y$ direction. This bifurcated behavior was more pronounced for $Fr = 50$, where the centerline of the jet deviated from the nozzle axis by almost $5D$.

3.2.2 Time-averaged Velocity Field

Figure 3.5 presents the normalized time-averaged velocity contours of the free jet flows between $x/D = 0$ and $x/D = 40$.

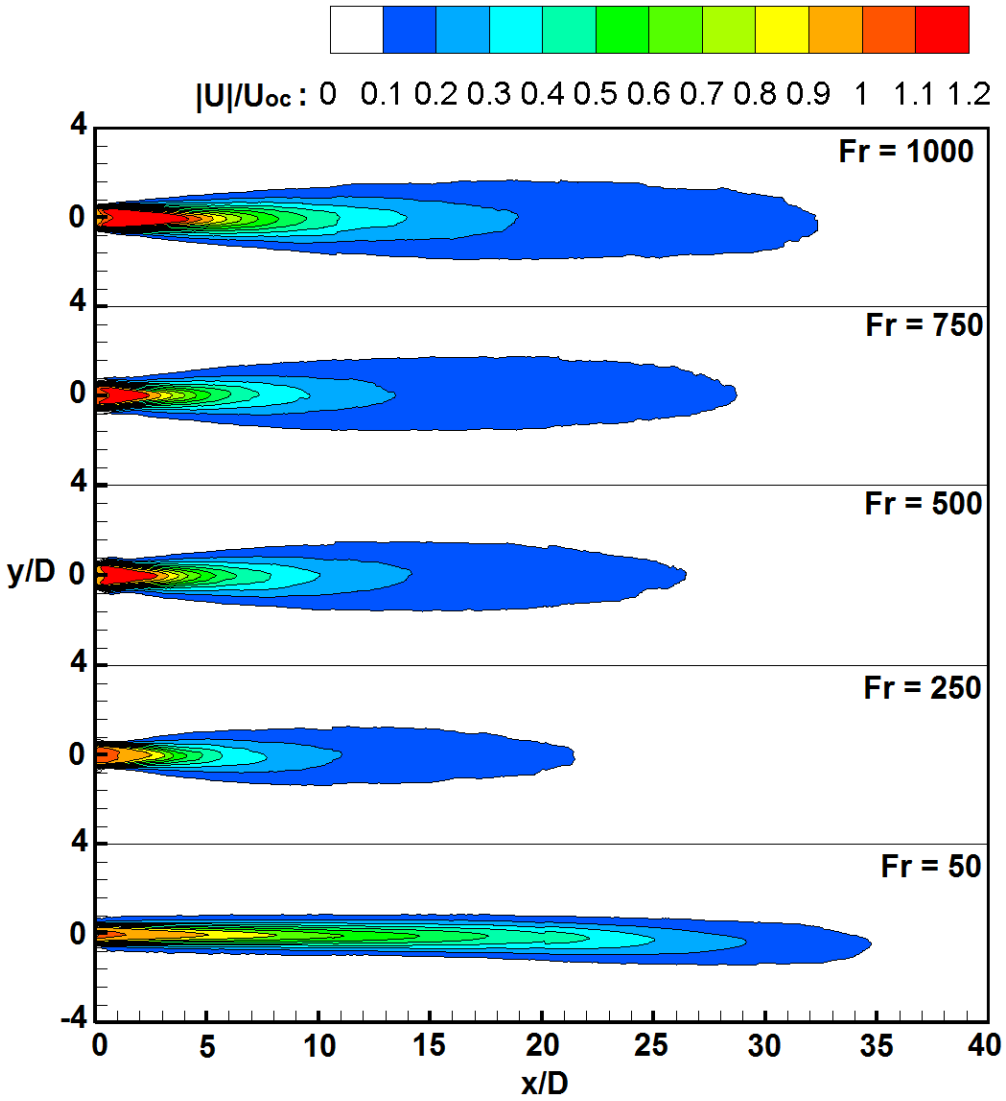

Figure 3.5 – Normalized time-averaged velocity magnitude ($|U|/U_{oc}$) contours between x/D = 0 - 40.

For each case, the red central area downstream of the nozzle exit corresponds to the potential core region with approximately uniform velocity. In the free jet flows, flow contours spread out gradually and symmetrically for high Froude numbers (i.e. *Fr* > 250), and the effects of buoyancy forces were negligible. It was also observed that higher Froude numbers led to bigger potential core area. However, for lower Froude numbers, the far-field region deformed under the influence of buoyancy forces which led to lower velocity decay rates due to presence of buoyancy driven acceleration

components. It should be noted that for Fr = 50, the Reynolds number was calculated to be 317, which corresponds to the laminar flow. It was observed that for x/D < 25, the jet travelled with minimal entrainment with very low velocity decay rates but at x/D > 30, the velocity profiles decayed gradually, and high amount of mixing occurred.

As mentioned before, in jets with Fr < 250, the far-field buoyancy-dominated regions were observed. To distinguish the momentum- and buoyancy-dominated regions in the jet, the jet/plume characteristic length scale, L_M, was used. This length scale describes the relative importance of momentum and buoyancy fluxes (List and Papanicolaou 1988) and is defined as:

$$L_M = \frac{M^{3/4}}{B^{1/2}}, \tag{3.2}$$

where M and B are specific momentum and specific buoyancy fluxes respectively and are defined as following:

$$M = QU_{oc}, \tag{3.3}$$

$$B = g\frac{(\rho_\infty - \rho_j)}{\rho_j}Q, \tag{3.4}$$

where Q is the initial volume flux, U_{oc} is the time-averaged nozzle exit velocity, g is the gravitational acceleration, ρ_∞ is ambient air density and ρ_j is helium jet exit density.

The resultant dimensionless distance in downstream direction (i.e. x/L_M) varies from very small values in jet-like to over 20 in plums-like flows. Jet/plume characteristic length scale may also be simplified into following relation:

$$L_M = Fr\,D, \tag{3.5}$$

where Fr is Froude number and D is the jet diameter.

Figure 3.6 illustrates the jet centerlines for free jet flows using the jet/plume characteristic length scale.

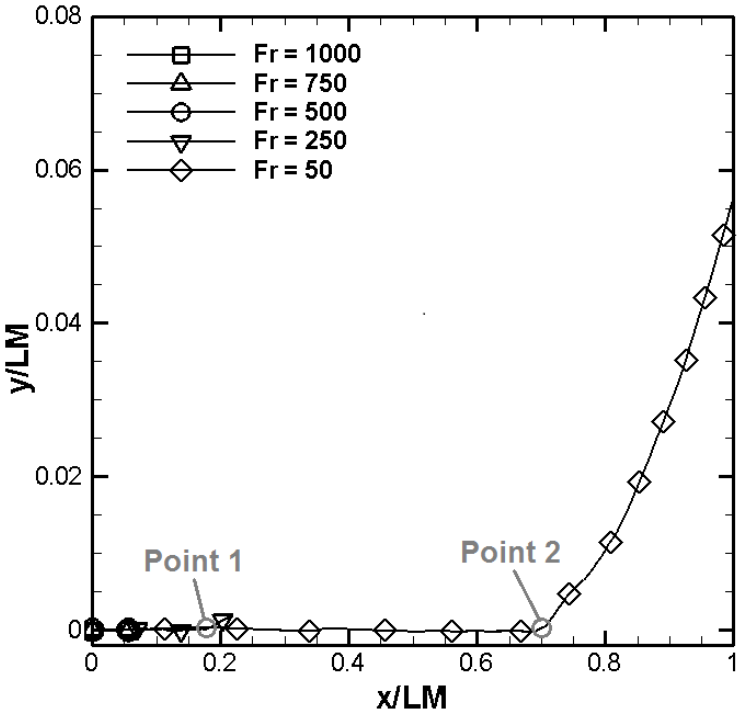

Figure 3.6 – Jet centerlines for free jet cases using L_M length scale.

Jet centerline representations of the cases with high Froude numbers (i.e. $Fr > 250$) showed straight lines with no deviations from the nozzle axis. However, a branched profile was observed for cases with lower Froude numbers and jet centerlines deviated from the nozzle axis. The branch points shown in Figure 3.6 can be used to identify the downstream location at which the first effects of buoyancy occurred. The position of these braches for Fr = 250 and 50 were observed to be located at approximately x/L_M = 0.16 and 0.61 which are identified as Points 1 and 2 in Figure 3.6. The corresponding downstream locations for points 1 and 2 were calculated to be x/D = 43 and 32 for Fr = 250 and 50 respectively. These downstream locations can be related to the points at

which the first effects of buoyancy occur which are consistent with the findings presented in Figure 3.4.

3.2.3 Velocity Decays

In order to characterize the jet flow in more details, a plot of the jet spread rates in terms of the inverse of the normalized time-averaged centerline velocity is presented in Figure 3.7. Here, $|U|_c$ denotes the centerline time-averaged velocity magnitude which is normalized by the time-averaged jet exit velocity at the center of the orifice, U_{oc}, and is plotted against centerline downstream coordinate, s, normalized by the jet diameter, D. The centerline downstream coordinate was calculated through numerical integration of the best fit centerline defined by Eqn. (3.1) for each case.

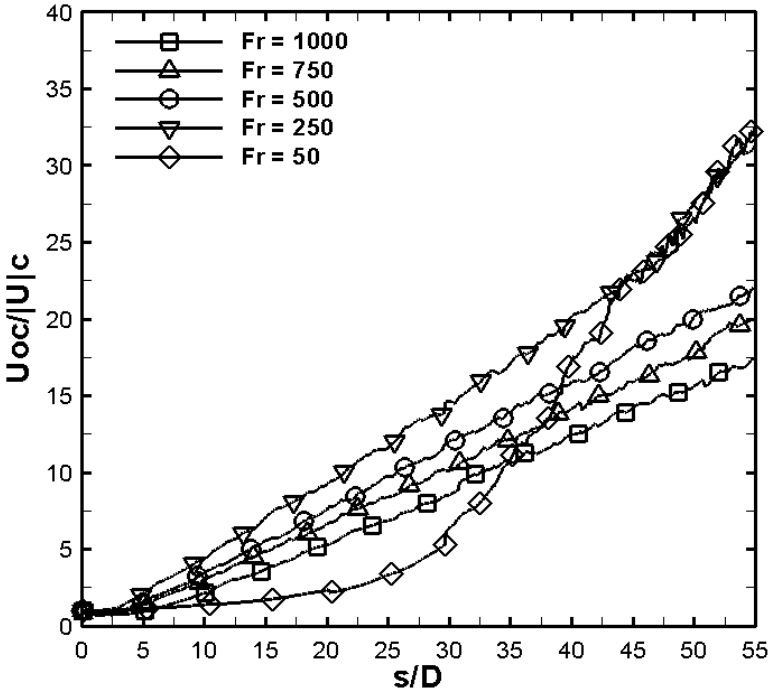

Figure 3.7 – Jet spread rate, free jet cases.

As shown in the Figure 3.7, downstream of the potential core region, the jet centerline velocity was decreased at a high rate for $Fr \geq 250$. However, for $Fr = 50$, the

exit velocity values persisted for 25 nozzle diameters downstream because of the laminar nature of the flow. In further observation, a correlation can be established between the *Fr* number, buoyancy effects and the centerline velocity decay rates. As shown in Figure 3.7, the jets centerline velocity for the case of *Fr* = 250, decayed much faster than that of higher Froude numbers. Therefore the smaller the *Fr* number the faster the flow will disperse in turbulent flow conditions.

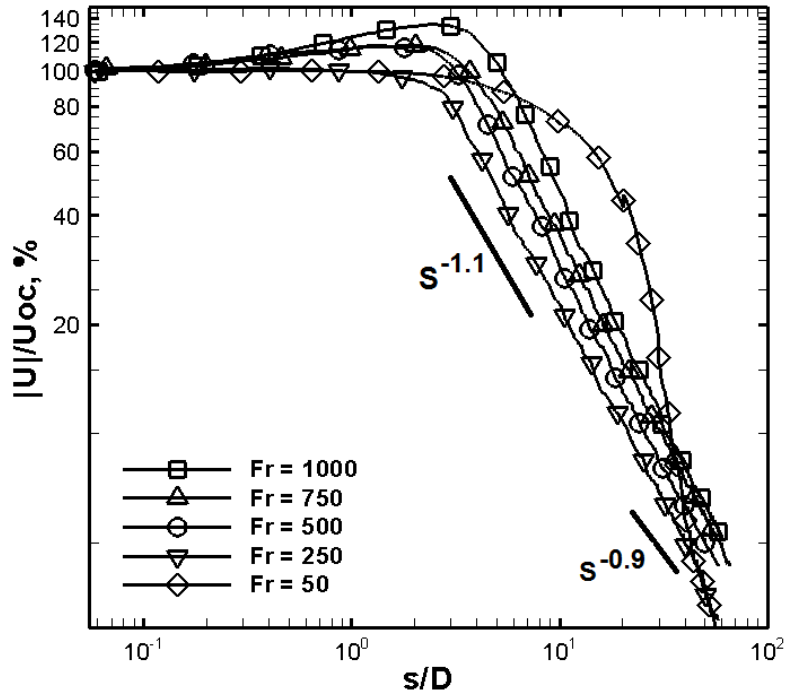

Figure 3.8 – Jet centerline mean velocity magnitude decay, free jet cases.

Normalized velocity decay profiles along the jet centerline coordinate system are presented in Figure 3.8. In order to show the power-law decays along the jet centerline in a linear manner, a log-log plot is preferable. The time-averaged velocity magnitude in immediate downstream of the jet exit is shown as 100% which experienced a rapid increase of approximately 30% to U_{cm} at the jet far-field regions as a result of the sharp-edged orifice inflow condition explained in section 2.1 and (Quinn 1992). It should be noted that in cases with lower initial time-averaged velocity (i.e. *Fr* = 250 and 50), this

centerline velocity overshoot was not observed and the effects of the initial inflow condition was negligible. However, the effects of the inflow condition were evident on the velocity decay rate which is explained in following.

For $Fr \geq 500$, equal velocity decay rates were observed downstream of the potential core region. The $s^{-1.1}$ and $s^{-0.9}$ lines are shown on Figure 3.8 for comparison. For Fr = 250, the velocity decay rate of $s^{-1.1}$ was observed in the jet near-field regions which was similar to those of higher Froude numbers. However, slower decay rate was observed at the jet far-field regions as a result of buoyancy-driven acceleration components in the buoyancy dominated regions. The decay rate of approximately $s^{-0.9}$ was observed at s/D > 50. For Fr = 50, slow decay rates were observed for almost 25 nozzle diameters downstream of the jet exit as a result of laminar flow condition. At the jet far-field regions, jet structure suddenly transitioned to turbulent flow with very high velocity decay rates of approximately $s^{-3.3}$. These decay rates dropped slightly in $s > 50D$ in buoyancy dominated regions.

It should be noted that the centerline velocity decay rates for the free jets flows initiated from a contoured nozzle are reported to be s^{-1} (Su and Mungal 2004). The faster velocity decay rates can be linked to the sharp-edged inflow condition.

3.2.4 Time-averaged Velocity Profiles

The radial velocity profiles at several downstream locations are presented in Figure 3.9.

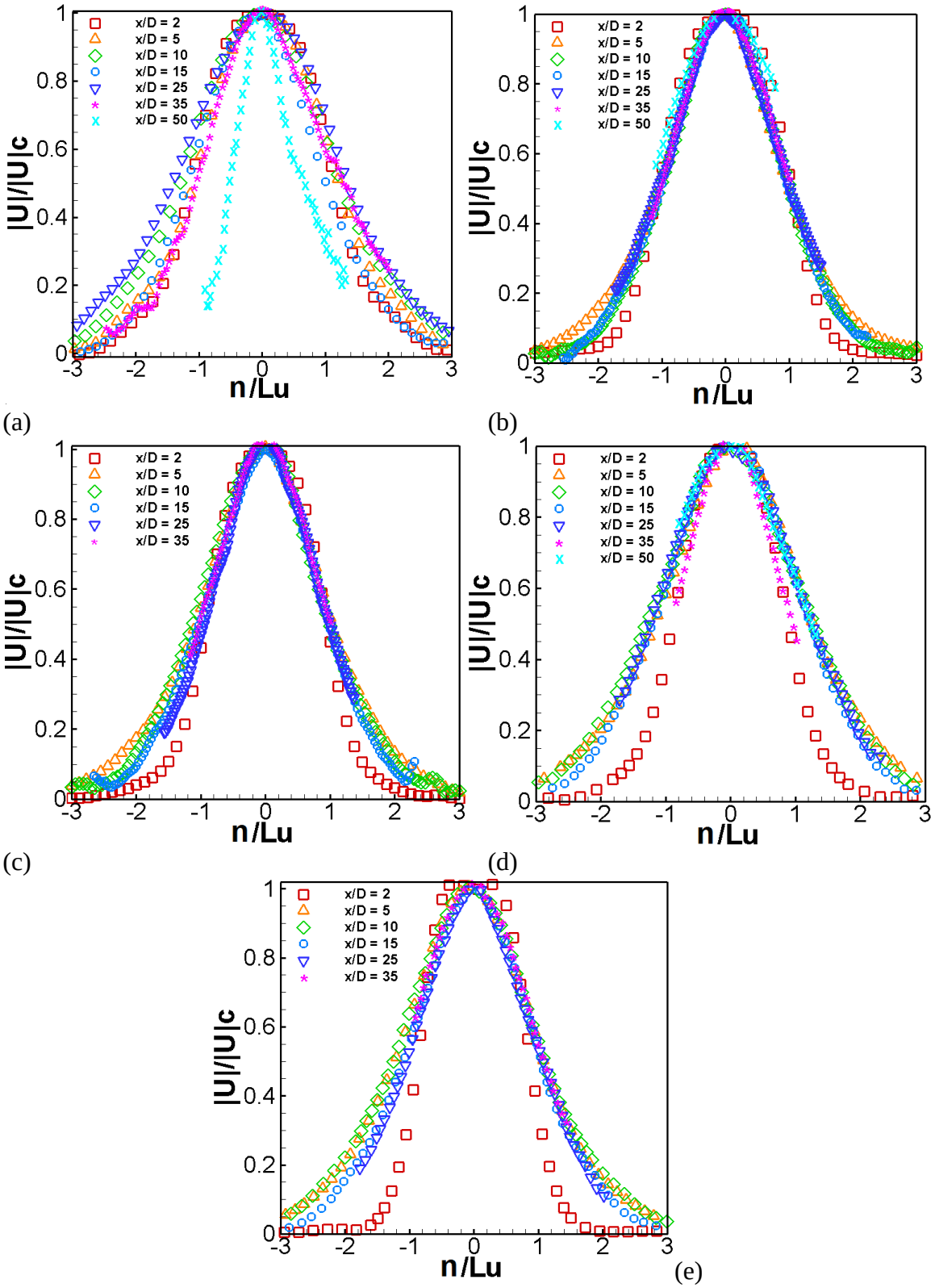

Figure 3.9 – Radial profiles of the normalized time-averaged velocity. Fr = (a) 50, (b) 250, (c) 500, (d) 750 and (e) 1000.

Here, L_u represents the radial location at which the time-averaged velocity is half of the centerline velocity. It is evident from the figure that the radial profiles for x/*D* = 5, 10, 15, 25, 35 and 50 for *Fr* > 250 are symmetric and can be accurately approximated by a Gaussian distribution. For *Fr* = 50, the radial velocity profiles for x/*D* = 50 was not symmetric as a result of high buoyancy forces in this region which forced the flow to rise and narrowed the lower side of the jet boundary in -*n* direction.

Figure 3.10 presents the normalized time-averaged velocity magnitude profiles for the free jet discharges at several downstream locations. Velocity magnitude is normalized by time-averaged nozzle exit velocity. In the cases with high Froude numbers, radial velocity profiles show a symmetrical bell-shaped peak which coincides with the jet centerline. However, for low Froude numbers, these symmetrical velocity profiles were observed to deform and at the jet far-field regions as the jet shifted up as a result of strong buoyancy forces.

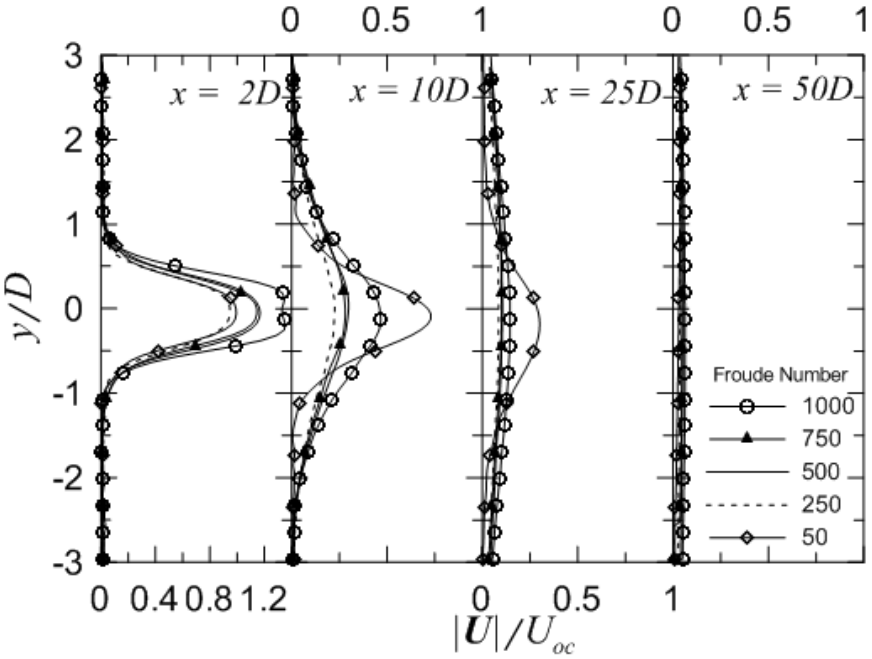

Figure 3.10 – Time-averaged normalized velocity magnitude profiles of the free jet cases.

3.2.5 Turbulence Statistics

Normalized rms velocity components (i.e. $u'/|U|c$ and $v'/|U|c$) along the jet centerline coordinate system are plotted in Figure 3.11. High initial turbulence intensity of sharp-edged orifice structure led to low initial values in the velocity fluctuations. These velocity fluctuations increased rapidly downstream of the potential core region. Axial fluctuations were generally higher than the radial fluctuations for all cases considered herein. The asymptotic ratio of $v'/u' \approx 0.75$ was observed which is slightly higher than values reported by contoured nozzle ($v'/u' \approx 0.7$) (Xu and Antonia 2002). In the case of Fr = 250 these axial fluctuations experienced a peak at the jet near-field region downstream of the potential core area as a result of strong shear layer instabilities in this region.

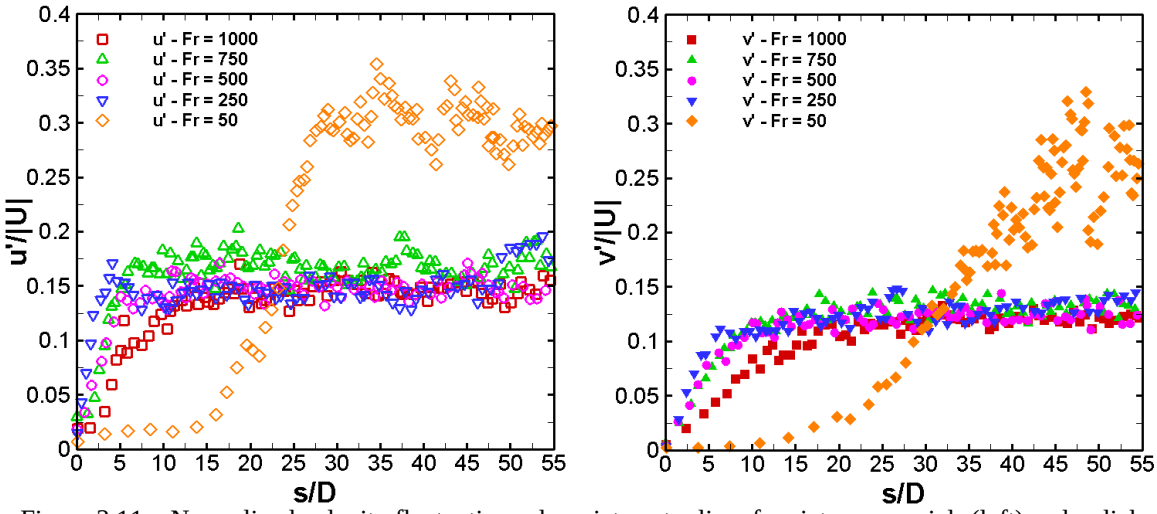

Figure 3.11 – Normalized velocity fluctuations along jet center line, free jet cases, axial- (left) and radial-velocity fluctuations (right).

At low Froude numbers (i.e. Fr < 250), increased velocity fluctuations were observed in the buoyancy-dominated regions. It should be noted that for Fr = 50, laminar nature of the flow at the jet near-field led to very low velocity fluctuations which gradually increased in the transition region.

Figure 3.12 illustrates the profiles of turbulent kinetic energy components in the jet center-plane for *Fr* = 1000 and 250 which corresponded to flow conditions with negligible and more pronounced buoyancy forces respectively. The turbulence stresses for the case of *Fr* = 50 are not discussed here because of laminar nature of the flow.

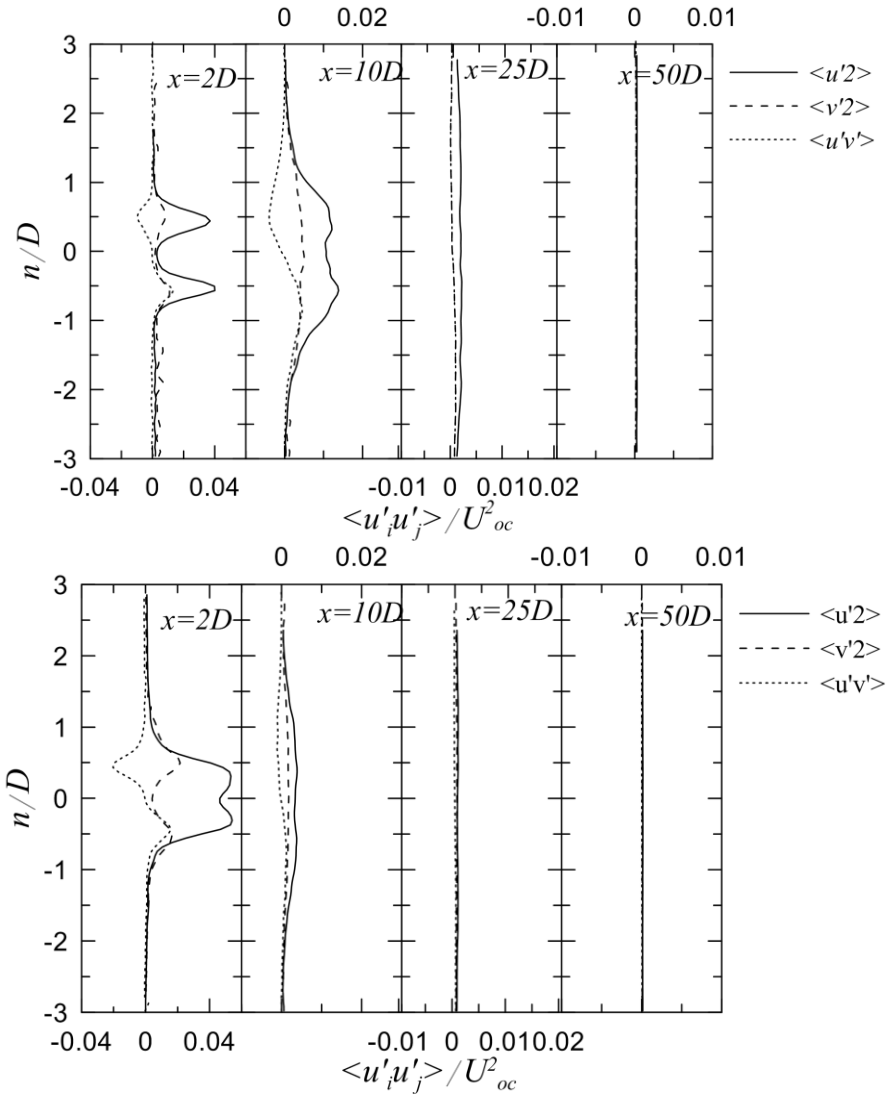

Figure 3.12 – Stress profiles in jet center-plane for free jet cases. (a) *Fr* = 1000, (b) *Fr* = 250.

Turbulent stress components were normalized by time-averaged nozzle exit velocity, U_{oc}. The profiles of turbulent normal stresses for all free jet flows were

observed to be similar with slight difference in magnitudes so general conclusions were drawn for all the cases considered herein.

The averaged axial normal stress components, $<u'^2>$ and the radial component, $<v'^2>$, showed two peaks at the jet near-field region with a saddle-back profile centered at the jet centerline. These show the dominance of the jet shear layer instability at the jet near-field region. The $<u'^2>$ components had higher magnitudes than $<v'^2>$ due to strong pressure gradient in *n*-direction (Yuan, Street and Ferziger 1999).

Farther downstream, the two peaks in the normal stress components meet, leading to a single peak profile. (Yuan, Street and Ferziger 1999) also noted that at locations that are sufficiently far downstream from the nozzle, the turbulent normal stress components generated between the jet fluid and ambient produce a single local peak. It should be noted that for Fr = 250 the axial component of turbulence kinetic energy showed a higher magnitude peak than the radial stress profiles, which is also evident in the plots presented in Figure 3.11.

The turbulent shear stresses, $<u'v'>$, in the jet near-field region were observed to have a high positive value at the jet lower boundary and a high negative value at the upper boundary which are also resulted from jet shear layer instability. At the jet far-field regions the negative shear stress region became stronger relative to positive region. This could be a result of presence of high buoyancy driven acceleration components, which deflected the jet structure towards the $+n$ direction.

3.2.6 Vorticity

The vorticity field and the streamline contours for the free jet flows for the range of Froude numbers considered herein are presented in this section. The out-of-plane vorticity fields, ω_z, were calculated using the following relation from the PIV vector field.

$$\omega_z = \frac{\partial v}{\partial x} - \frac{\partial u}{\partial y} \tag{3.6}$$

The vorticity magnitude and the streamlines were calculated using time-averaged velocity fields extracted from a sequence of 400 PIV images. The streamlines were plotted using the Tecplot software.

The time-averaged vorticity and the streamlines for the free jet flows are presented in Figure 3.13 and Figure 3.14 respectively. It should be noted that jet flows from left to right in all figures presented in this thesis. The images presented in Figure 3.13 illustrate two large-scale vortices form in the shear layer produced at the jet and ambient air interface. The shear layer at the top of the jet consisted of positive (counter clockwise) vorticity and the lower shear layer consisted of negative (clockwise) out-of-plane vorticity.

The vorticity magnitude increases by increasing the Froude number as a result of increased velocity gradient between the jet flow and the ambient air interface. The maximum vorticity magnitudes were observed at the nozzle tip were the jet flow was first introduced to the ambient. Moving to farther downstream locations the peak vorticity was decreased but the overall circulation was increased due to larger spatial extent. For $Fr > 250$ the vorticity magnitude dropped drastically for $x/D > 8$.

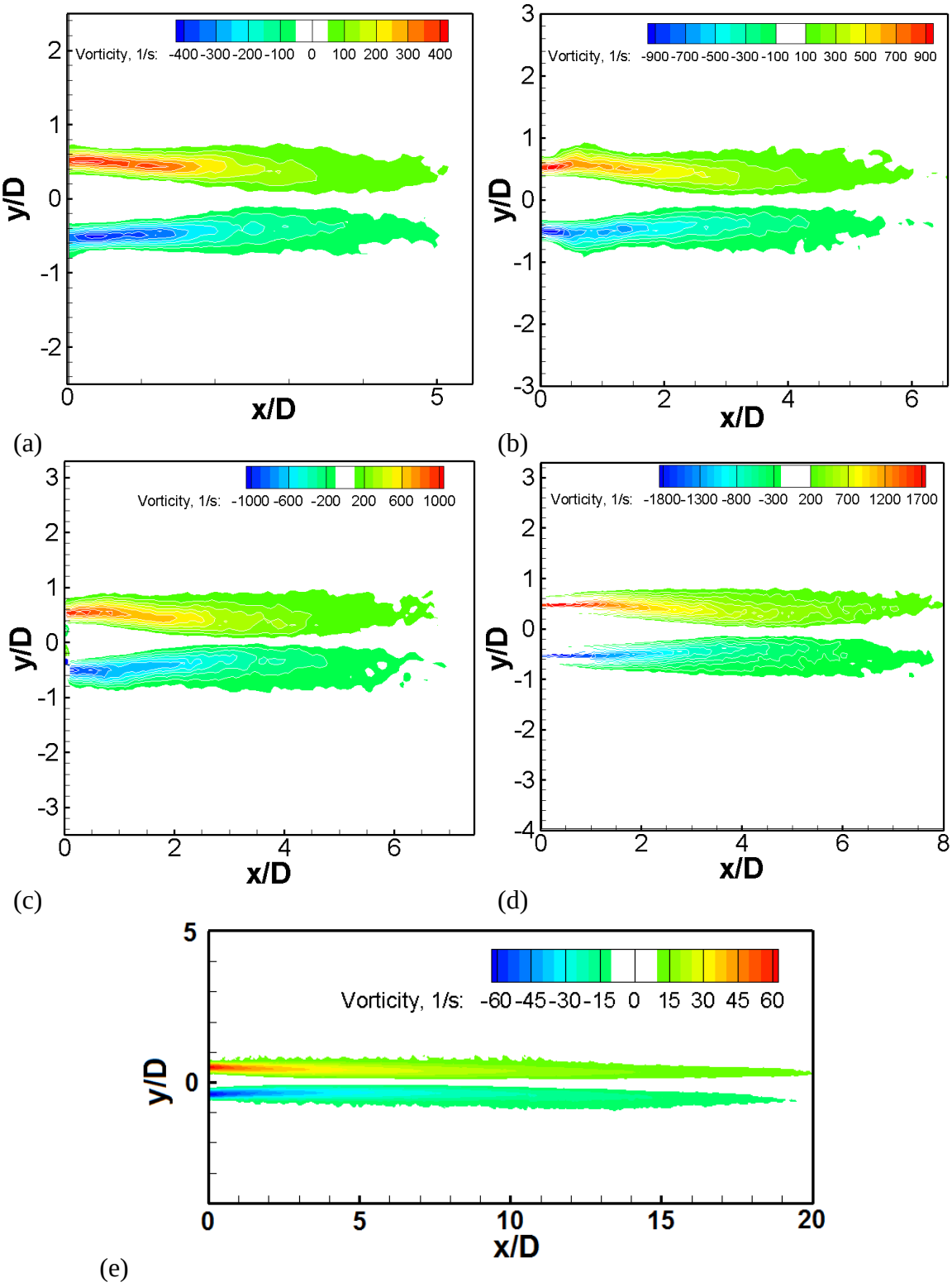

Figure 3.13 – Time-averaged out-of-plane vorticity contours Fr = (a) 250, (b) 500, (c) 750, (d) 1000 and (e) 50.

For *Fr* = 50, the vorticity magnitude decayed with a slower rate comparing to higher Froude numbers. This was due to laminar nature of the flow, which led to lower ambient entrainment in jet near-field areas.

Time-averaged stream line of the free jet flows with Froude number 50, 250 and 1000 are shown in Figure 3.14.

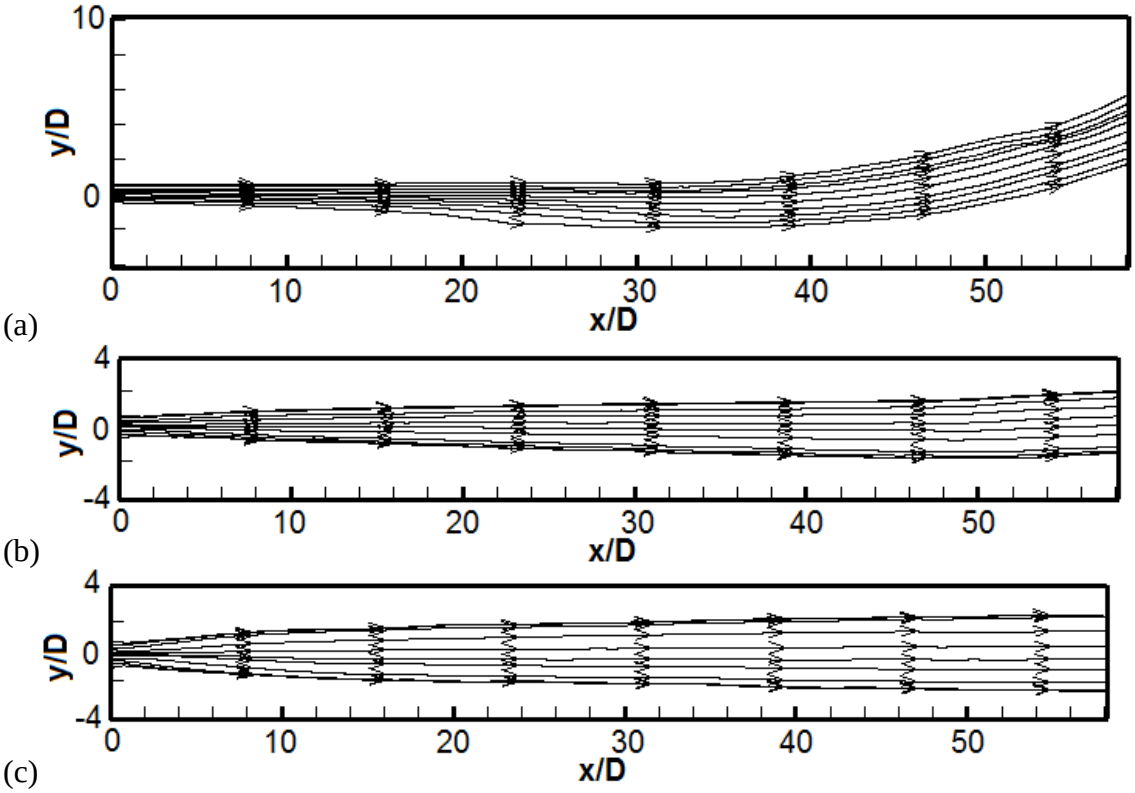

Figure 3.14 – Time-averaged streamlines Fr = (a) 50, (b) 250, (c) 1000.

The streamline pattern for *Fr* = 500 and 750 showed same configuration as *Fr* = 1000 and they are not shown here in order to avoid repetition.

As shown in the figure, the averaged streamlines for *Fr* = 50 deviated towards the *+y* direction due to presence of strong buoyancy forces at x/D > 35 which is consistent with the finding presented in Figure 3.6. The streamlines for *Fr* = 250 showed the similar behavior at the jet far-field region (i.e. *x/D* > 45). The streamlines representation

for Fr > 250 showed no centerline deviation from the nozzle axis and the buoyancy forces were observed to be negligible in the regions under the study.

3.2.7 Jet Boundary and Jet Width

Figure 3.15 illustrates the jet boundary contours for free jet flows. The flow boundary contours were computed by first determining the jet centerline (dashed line), then moving in centerline's normal direction, *n*, at each downstream location until the velocity dropped to a specified fraction of the centerline value. Su and Mungal (2004) suggested the points of the boundary contours at a given normal profile to be located where the local value is 20% of the centerline value . The 20% of the centerline values gives a good representation of the boundary contours, but due to the high resolution of the current data this value was even further reduced to 10% (solid lines in following figure). The jet centerline was identified by determining the maximum time-averaged velocity at each downstream location.

For Fr = 50, the minimal ambient entrainment for x/D < 28 and corresponding laminar structure is evident in Figure 3.15. For higher Froude numbers the rapid growth of jet boundary layers caused the boundary contours to exit the imaging plane for x/D > 20.

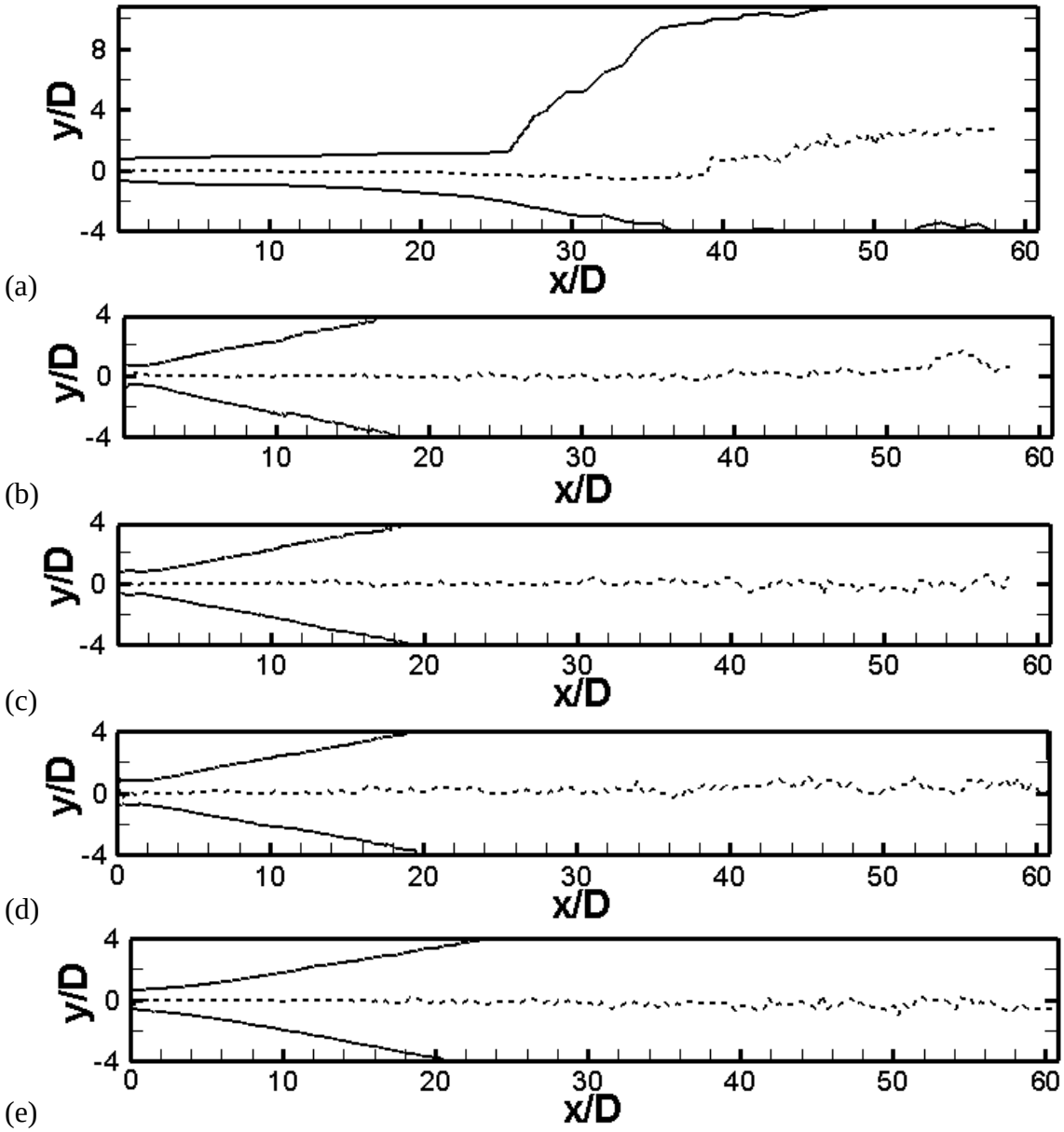

Figure 3.15 – Free jet boundary contours, Fr = (a) 50, (b) 250, (c) 500, (d) 750 and (e) 1000.

Figure 3.16 represents the downstream evolution of the jet width for the free jet flows. The nominal half-width at each location was computed as the distance between the jet boundary and the jet centerline. These values were calculated separately for $+n$ direction (i.e. upper boundary) and $-n$ direction (lower boundary). These partial width values were designated by δ_+ and δ_-, respectively and the full width by $\delta_t \equiv \delta_+ + \delta_-$.

(a)

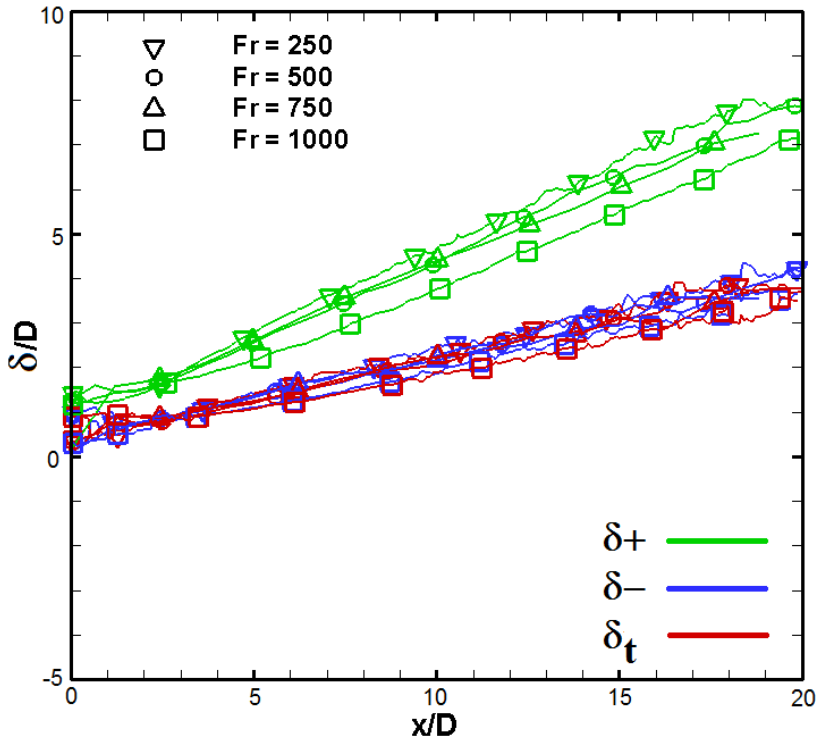

(b)

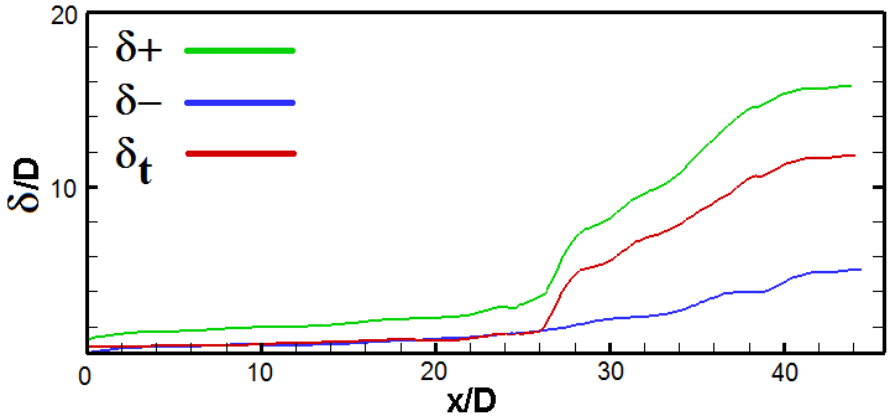

Figure 3.16 – Flow width, Fr = (a) 250, 500, 750 and 1000, and (b) 50.

For $Fr \geq 250$, the δ_+ and δ_- half-width values almost collapsed on each other, which represented the symmetric growth of upper and lower boundaries of the jet in these cases. The jet full width observed to be slightly narrower in higher Froude numbers as a result of higher initial jet momentum in these cases. For Fr = 50, partial half-width values collapsed for $x/D < 26$ due to laminar characteristics of the flow. At the far-field

locations the flow transitioned from laminar to turbulence and the jet structure was clearly asymmetric due to presence of strong buoyancy forces. As a result the jet's upper boundary thickened and the jet centerline deflected towards the *+y* direction.

3.3 JET IN CROSSFLOW

Physical properties of the horizontal jet dispersion in crossflow for the wide range of Froude numbers (i.e. *Fr = 1000, 750, 500, 250* and *50*) are presented in this section. Figure 3.17 illustrates the schematics of the experimental setup for these cases.

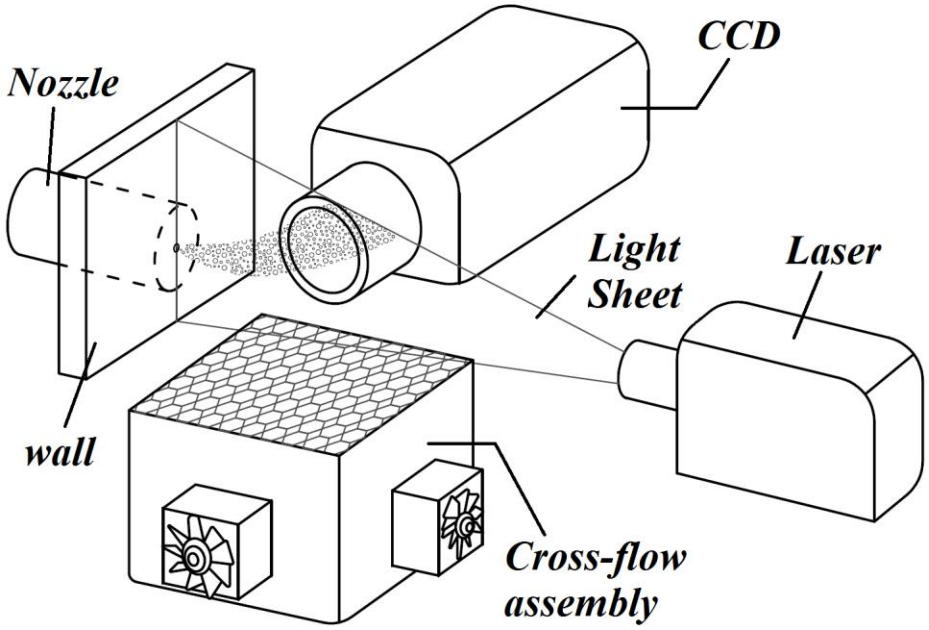

Figure 3.17 – Schematics of the experimental setup for jet in crossflow cases.

3.3.1 Scaling of Jet in Crossflow

Analysis and scaling of the vortical structure in crossflowing jet were subjected to various studies. Different factors in scaling of crossflowing jets have been used in an ongoing attempt to find the appropriate global scaling factor in order to achieve a better understanding of physical nature of these flows. Three different scaling factors were

used extensively in literature and advantages and drawbacks of each method are explained in following.

Employing jet diameter, *D*, as normalization parameter might be a more convenient choice since it has been used conventionally in free jet flows. It has been reported that in the vortical structure of the crossflowing jets, horseshoe and wake vortices have identical oscillating modes which can be calculated based on the jet diameter (Moussa, Trischka and Eskinazi 1977). Fric and Roshko (1994) provided visualization of crossflow and jet exit boundary layers experimentally and concluded these two sources as the main sources of vorticity in the jet in crossflow. All these argument and also Reynolds number calculation are based on the jet diameter, *D*. However, Kelso *et al*. (1996) showed that formation of wake vortices from the separation of crossflow boundary layer in inner side of the jet is very much dependent on jet-to-crossflow velocity ratio, *r*, and jet Reynolds number. The major drawback of using local length scale, *D*, as the scaling factor in crossflow studies is the dependency of results on the velocity ratio. Jet diameter normalization scale allows *r*-dependent structural analysis which will be presented in more details in following sections.

In order to suppress the effects of *r* in the jet in crossflow studies, Broadwell and Breidenthal (1984) considered momentum fluxes in the jet far-field regions and concluded that product of velocity ratio and jet diameter is the only global length scale. The *rD* scaling factor can be used to collapse jet centerlines for the cases in which different jet-to-crossflow velocity ratios were considered. Pratte and Baines (1967) employed this strategy and normalized all coordinate systems with *rD* to collapse centerlines of jet flows with different *r* values and they also developed a formulation to

generalize jet centerlines with r = 5 to 35. Centerline velocity decays and physical dimensions of crossflowing jets with different jet-to-crossflow velocity ratio may be well quantified by rD scaling factor. Although the rD factor might be a very good agreement in crossflowing jet studies but it still cannot provide a global length scale for all classes of jet-to-crossflow velocity ratios. Normalized coordinate systems using this factor resulted in different classes of jets depending on their r values. For instance, centerlines of jet flows with very small r values did not collapse on those with large r values. Not many information about classification of jets with different r values is documented in literature but according to data presented in this study jets with r = 3 to 8, $r < 1$ and r = 11 were observed to be in three different classes respectively.

Keffer and Baines (1963) used a third length scale, r^2D, in his studies for crossflowing jets with r = 6, 8 and 10 with various jet diameters. It was reported that this scaling factor was convenient to collapse jet centerlines for that class of jet-to-crossflow velocity ratio but still may not be used as a global factor for all r values. The r^2D factor may be used to identify jet near- and far-field regions and also to discuss self similarity properties of jet flows in crossflow. In following sections jet centerline representations and decay rates using different scaling factors are discussed for various Froude numbers.

3.3.2 Jet Centerline Using Different Scaling Factors

As mentioned before, it was preferable to use a new coordinate system in the jet discharges in crossflow. This new coordinate system reflects the flow evolution and the

jet spread in downstream locations. The schematics of the resultant jet in crossflow structure are shown in Figure 3.18.

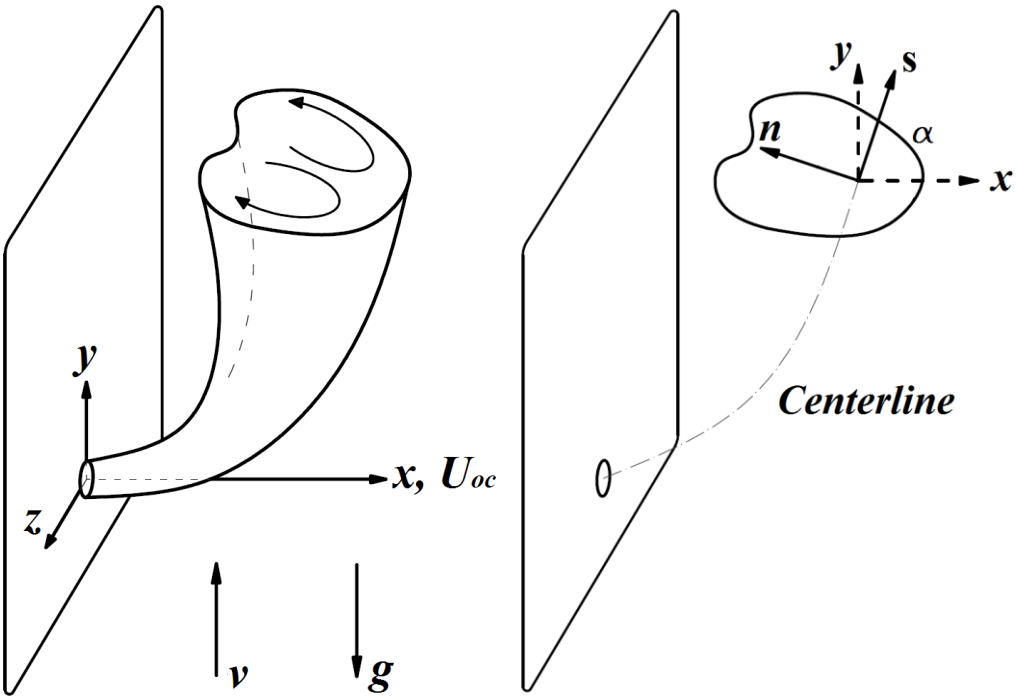

Figure 3.18 – Jet in crossflow (left), corresponding coordinate system (right).

The jet centerline was found based on the technique described in Section 3.1. It should be noted that the side of the jet corresponding to negative-*n* is called windward side and the relating boundary is called outer boundary. The jet surface and the boundary corresponding to positive-*n* is called wake or lee side and inner boundary respectively.

The *rD* scaling factor together with *D*, r^2D length scales introduced in 3.3.1 were used to normalize the *x*- and *y*-coordinate system. Figure 3.19 shows jet centerline representation for jet dispersions in crossflow using the jet diameter, *D* as the normalization factor.

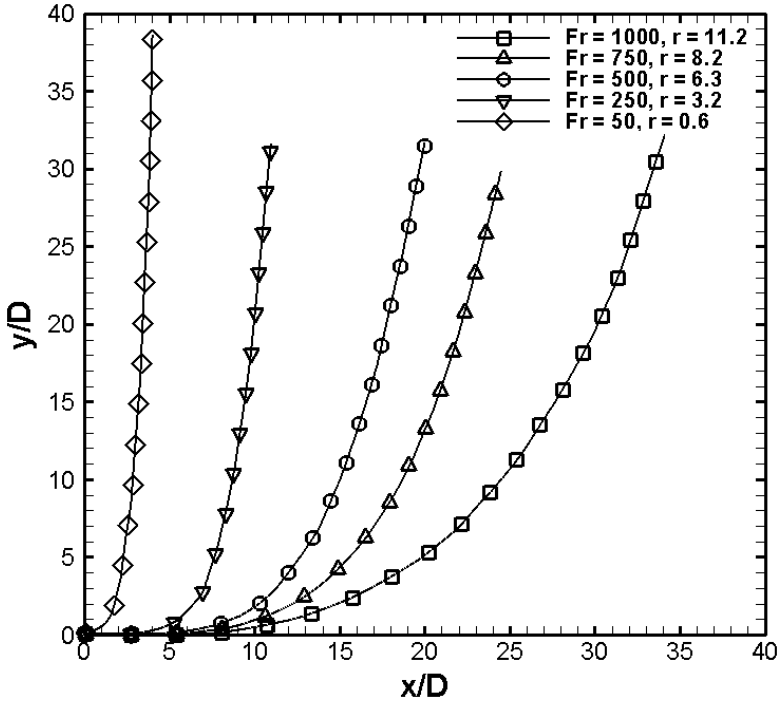

Figure 3.19 – Jet centerline representation normalized by *D*.

The *D* scaling factor allowed for structural analysis which was dependent on the jet-to-crossflow velocity ratio. The *D*-scaled plot in Figure 3.19 shows that increasing the *r* value led to the more jet penetration into the crossflow field. Jet centerlines for different *r* values clearly did not collapse over the whole range of study while using the jet diameter as the normalization factor. For Fr = 50 jet structure was observe to turn sharply in the direction of crossflow, downstream of a very short potential core region (i.e. $x < 0.5D$). For higher Froude numbers jet centerlines collapsed in potential core areas before turning towards the crossflow direction. As shown in Figure 3.19 jet centerlines collapsed in $x < 4D$ for $Fr > 250$ and in $x < 7D$ for $Fr \geq 500$. Keeping the crossflow velocity constant, higher the Froude number resulted in higher *r* values and longer potential core region due to higher initial momentum flux.

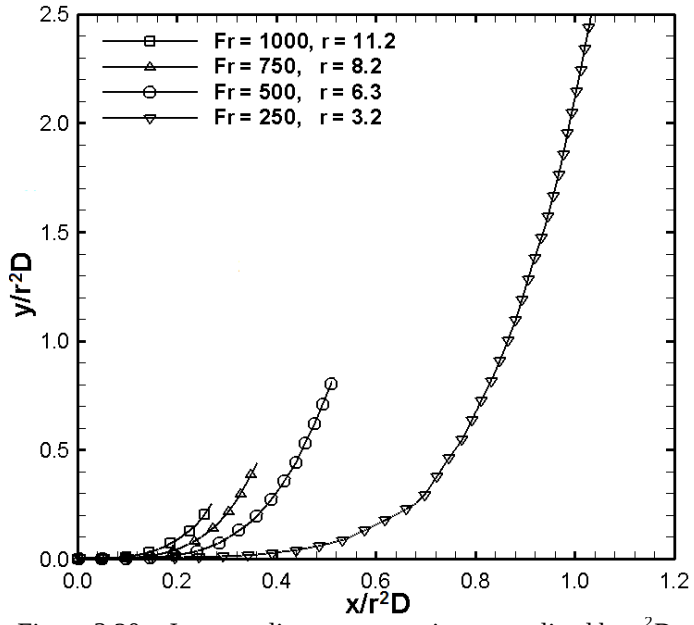

Figure 3.20 – Jet centerline representation normalized by r^2D.

The r^2D-scaled jet centerline representation is illustrated in a Figure 3.20. The jet centerline for $Fr = 50$ (i.e. $r = 0.6$) is not shown in this figure. Since for cases with low r value (i.e. $r < 1$), the r^2D-scale resulted in a very large jet span. In other words for cases with jet-to-crossflow velocity ratio bigger than unity, employing r^2D scaling factor led to a smaller normalized coordinate system whilst for cases with $r < 1$ this length scale enlarged the resultant non-dimensionalized coordinate system which made the comparison between these cases impractical. Keffer and Baines (1963) implemented r^2D length scale in his studies and showed that jet centerlines collapsed for $x < 0.05r^2D$ for different r values. Results presented herein did converge in that range and it was also observed that for $Fr \leq 750$ this range was extended to $x = 0.2\ r^2D$. Jet centerlines collapsed for the range of $x < 0.1r^2D$ for all the cases considered herein. As can be seen in Figure 3.20, this range was limited by r value and higher r value decreased this range. Full jet centerline collapse over the whole range was not achieved

at the jet far-field regions unless for cases with close r values (i.e. Fr = 500 and Fr = 750).

Figure 3.21 represents the jet centerlines using rD length scale. Pratte and Baines (1967) showed that the product of jet-to-crossflow velocity ratio and the jet diameter to be the only global length scale in crossflowing jet studies with different r values. However, as shown in the Figure 3.21, complete jet centerline collapse for all the jet flows considered herein was not achieved over the whole range of the study. Same behavior is also reported by (Mungal and Smith 1998) who concluded that the difference between their data and those of (Pratte and Baines 1967) could be because of the fact that Pratte *et. al*. data was extended to $100rD$ and were acquired using jets discharges from a pipe nozzle. Mungal and Smith (1998) also indicated that the presence of the wall surface in crossflowing jet studies (see Figure 3.17) might introduce a low pressure region behind the jet column which is r-dependent and could affect the jet centerline propagation. Fric and Roshko (1994) observed the same low pressure regions for cases with $r < 8$ and concluded that the effects of these regions are negligible for higher r values.

As shown in Figure 3.21, the effect of this low-pressure region was very pronounced for Fr = 50 which forced the jet centerline to deviate from other centerlines for $x > 0.3rD$. However, for higher Froude numbers (i.e. $Fr \geq 250$) jet centerlines were observed to collapse for $x < 1.5rD$. Although jet centerlines did not collapse completely in flows considered in the present study, it was observed that the rD scaling factor was a better candidate in crossflowing jet studies comparing to the D- and the r^2D-scale. Mungal and Smith (1998) also showed that physical dimensions of counter

rotating vortex pair structures of jets with different *r* values at fixed locations were essentially the same while *rD* length scale was used as the scaling factor.

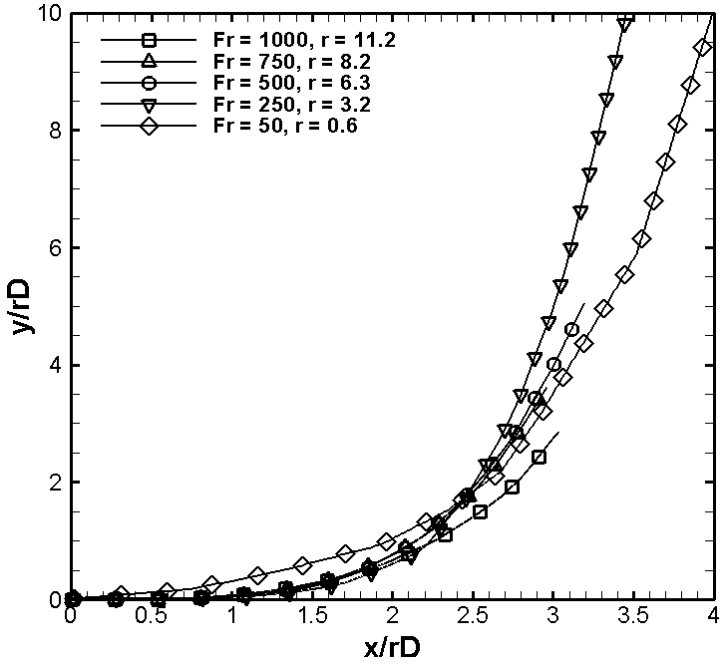

Figure 3.21 – Jet centerline representation normalized by *rD*.

Implementation of *rD*-scale same as r^2D-scale may result in enlarged jet span for cases with $r < 1$. This together with the resultant plume like flow structure which was observed for $Fr = 50$, led to the conclusion that this case belongs to a different group of crossflowing jets. General conclusions were drawn for $Fr = 50$ but detailed study of the resultant plume-like structure of the flow was not in the scope of the current study.

The *rD*-scale has been used as the global normalization factor and was used for further detailed analysis of the jet in crossflow cases. Eqn. (3.1) was used in order to find the least square fit to the locus of points of maximum velocity field. The constants of Eqn. (3.1) for jet flows considered herein were calculated to be $A = 3.09$, 3.37, 3.58, 3.31 and 3.88 with $\beta = 0.08$, 0.05, 0.07, 0.06 and 0.03 for $Fr = 1000$, 750, 500, 250 and 50 respectively.

3.3.3 Time-averaged Velocity Field

Figure 3.22 shows the normalized time-averaged velocity contours.

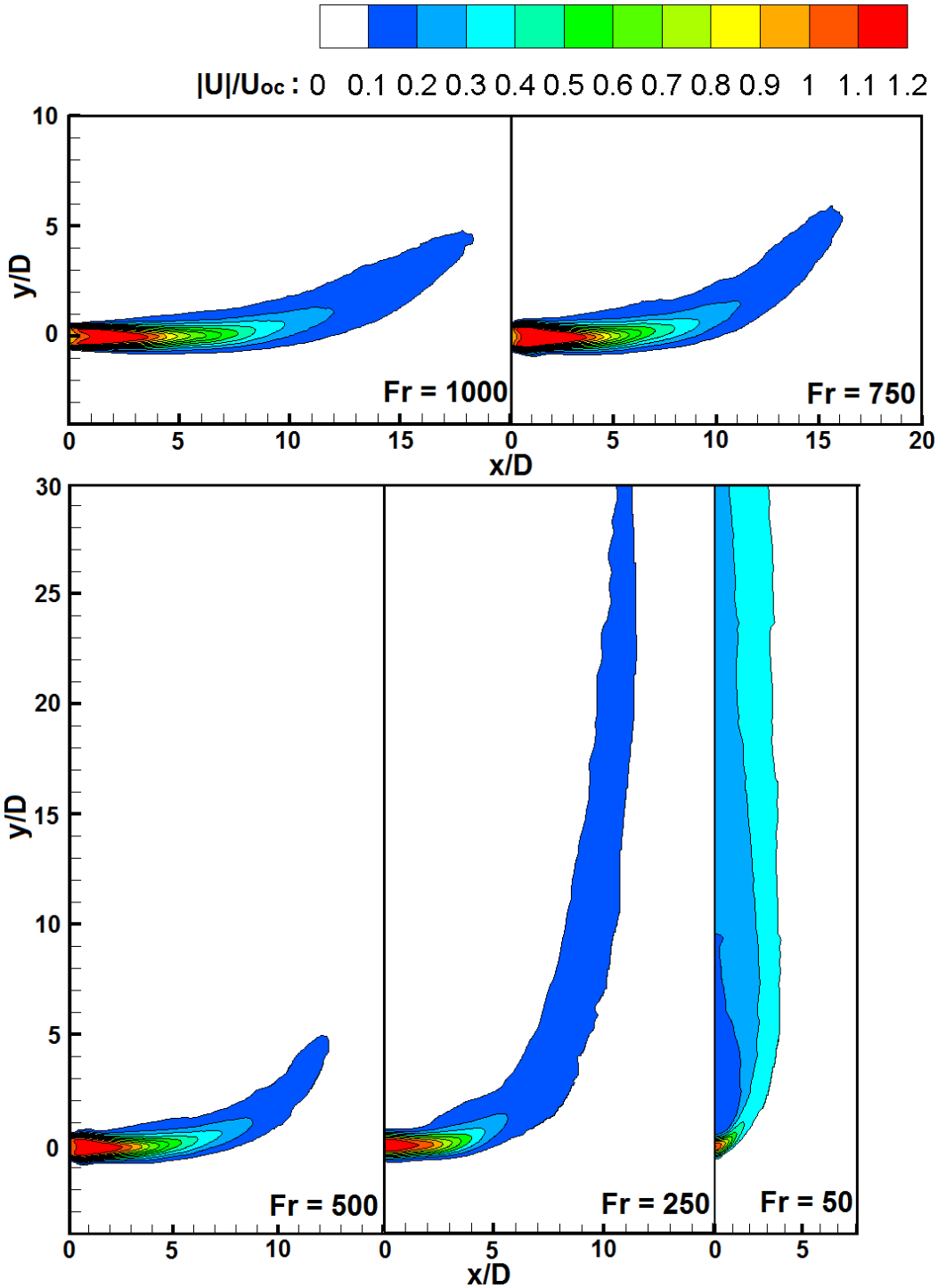

Figure 3.22 – Normalized time-averaged velocity magnitude ($|U|/U_{oc}$) for jet in crossflow.

The crossflow velocity was maintained to be constant for all jet flows considered herein. Jet-to-crossflow velocity ratios of approximately r =11, 8, 6, 3 and 0.6 were calculated for Fr = 1000, 750, 500, 250 and 50, respectively. The jet flows with higher Froude numbers penetrated farther into the crossflow structure, as it was expected.

Higher Froude numbers showed longer potential core areas as the result of higher initial momentum fluxes in these cases. Low r vales for Fr = 50 resulted in a sudden break down in the jet structure downstream of a very short potential core region.

3.3.4 Velocity Decays

3.3.4.1 The D Scaling

The jet centerline velocity decays are shown in Figure 3.23. The time-averaged velocity field was normalized by time-averaged nozzle exit velocity and the jet centerline coordinate system, s, was normalized by the jet diameter, D. In order to show power-law decays along the jet centerline in a linear manner a log-log plot was preferable. The 100% velocity magnitude shows the time-averaged nozzle exit velocity magnitude. Farther downstream, the centerline velocity was observed to increase to a maximum of 130% for flows with $Fr \geq 500$ under the influence of sharp-edged orifice nozzle structure. For Fr = 250 and 50 a negligible velocity increase was observed. The velocity profiles decayed downstream of the potential core region. Lowering the r value led to smaller potential core length, l. The potential core lengths for different cases considered herein were measure as: $l = 4.9D$ for Fr = 1000, $l = 4.5D$ for Fr = 750, $l = 3D$ for Fr = 500, $l = 1.1D$ for Fr = 250 and $l = 0.1D$ for Fr = 50.

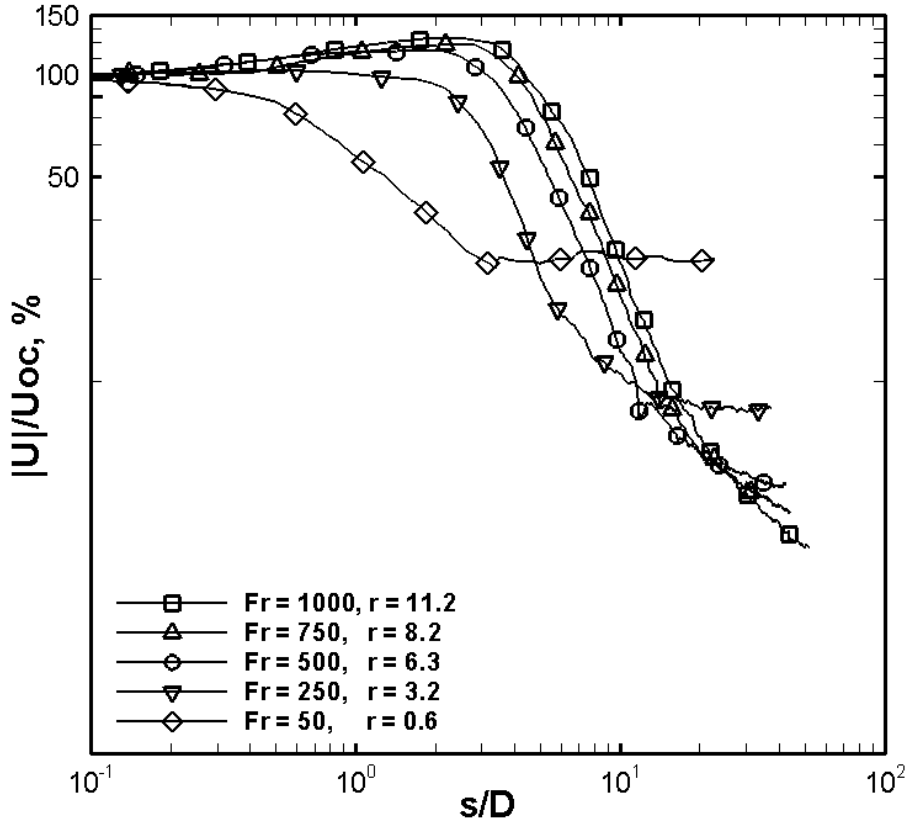

Figure 3.23 – Jet centerline time-averaged velocity magnitude decay normalized by jet diameter, *D*

For mixing purposes, *Fr* = 50 with smallest potential core area would be the best candidate. For other design objectives it should be noted that centerline decay lines for different *r* values crossed each other. For instance for a desired decay rate of below 20%, *Fr* = 500 showed a faster decay comparing to *Fr* = 250. As shown in Figure 3.23, *Fr* = 50 illustrated a completely different decay rate comparing to other jet flows. This together with the plume-like structure of the resultant flow proved the conclusion that *r* = 0.6 belonged to a different class of crossflowing jets. For other cases it was observed that lowering the Froude number resulted in slower decay rates.

Downstream of the potential core region, the jet centerline velocity decayed at a high rate depending on the Froude number. Farther downstream, velocity decay profiles branched to a region of slow decay rate at the jet far-field locations. For *Fr* = 50,

centerline velocity decay profiles converged to a steady value at the jet far-field region as the flow velocity approached the crossflow velocity. As shown in the Figure 3.23, the branch points were moved closer to the jet exit by lowering the Froude number. Slower decay rates at the jet far-field regions downstream of the branch point may be explained by the pronounced buoyancy forces in those locations. The presence of strong buoyancy driven acceleration components at the jet far-field regions slowed down the velocity decay rate which forced the decay plots to branch.

3.3.4.2 The rD Scaling

Time-averaged velocity magnitude along the jet centerline for different Froude numbers normalized by *rD* factor is presented in Figure 3.24. The velocity magnitude and the centerline coordinate system were normalized by the time-averaged nozzle exit velocity and the *rD* length scale, respectively.

Inside the potential core area for $Fr \geq 500$, the centerline velocity increase to a maximum value of 130% was observed due to sharp-edged orifice structure of the nozzle. For $Fr = 50$ and 250, the centerline velocity magnitude remained 100% due to low initial contraction and the effects of initial inflow condition were negligible.

Downstream of the potential core region the decay rate of approximately $s^{-1.5}$ was observed for $Fr > 250$. Faster centerline velocity decay rates were observed in crossflowing jet flows comparing to free jet flows. The decay rate of free jet flows was observed to be approximately $s^{-1.1}$. The $s^{-1.5}$ and $s^{-2.3}$ line are also shown in Figure 3.24 for comparison. For $Fr = 50$, a much slower centerline decay rate of $s^{-2.3}$ was observed and the centerline decay profiles followed a completely different path. The $s^{-2.3}$ decay

rate corresponded to the wake-like region of the crossflowing jet (Su and Mungal 2004). The plume-like behavior of the *Fr* = 50, which is shown in Figure 3.22, and its $s^{-2.3}$ decay rate confirms that this jet flow belongs to the different class of crossflowing jets.

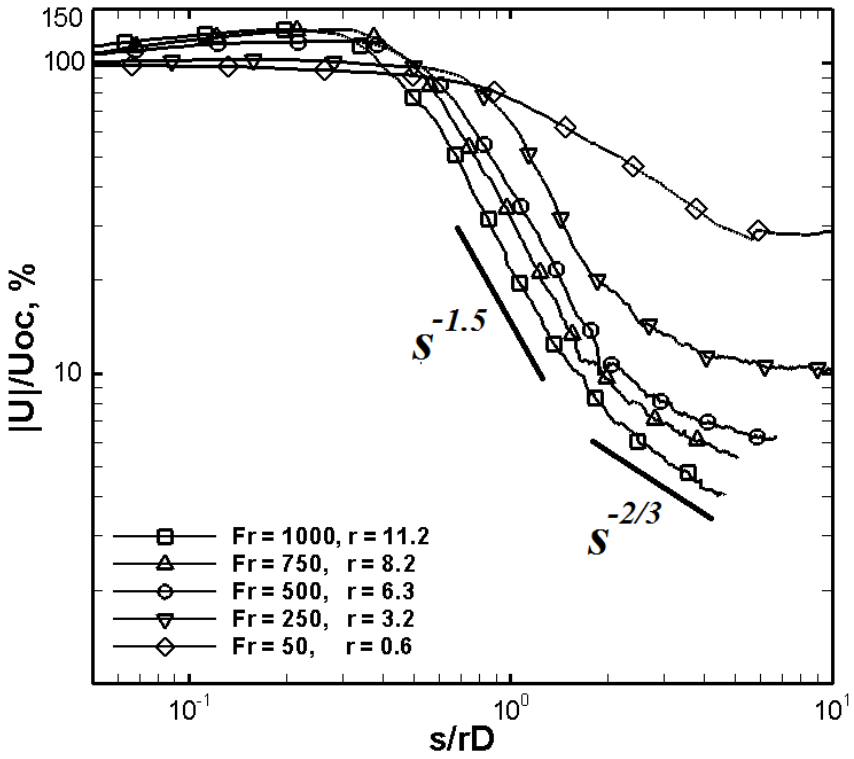

Figure 3.24 – Time-averaged velocity decay along jet centerline normalized by *rD* length scale

For $Fr \geq 250$, downstream of the region with $s^{-1.5}$ decay rate, the jet centerlines branched away to a region with slower decay rates. Decays rates of these downstream regions were observed to be slower than those of free jet flows. The location of these branch points are of a particular interest, especially according to the jet mixing point of view. These branch points were located in locations at which the centerline velocity decay rates slowed down from $s^{-1.5}$ to approximately $s^{-2.3}$. These points are reported as the transition points between jet- and wake-like regions (Su and Mungal 2004). It has

been also reported by (Mungal and Smith 1998) that the position of the branch point in the jet centerline velocity decay profiles normalized by *rD*-scale corresponds to the position at which the counter-rotating vortex pair structure is fully developed. Here, increasing the Froude number was observed to delay the branch point in the centerline velocity decay plots. It can be concluded that increasing the Froude number while keeping the crossflow velocity constant may move the formation of fully developed counter-rotating vortex pair structure farther downstream. For jet flows considered herein, the branch points occurred at $s = 2\ rD$ for $Fr = 50$, at $s = 2.46\ rD$ for $Fr = 250$, at $s = 2.6\ rD$ for $Fr = 500$, at $s = 2.86\ rD$ for $Fr = 750$ and at $s = 4\ rD$ for $Fr = 1000$.

For $Fr = 50$ and 250 the time-averaged velocity decay rates along the jet centerline showed no power-law dependency and the velocity magnitude remained constant at the jet far-field regions. The jet centerline velocity was observed to approach the crossflow velocity (i.e. $v_\infty = 11.2$ m/s) at those downstream locations.

3.3.4.3 The r^2D Scaling

The time-averaged velocity decay rate along the jet centerline normalized by r2D-scale is presented in Figure 3.25.

For $Fr = 50$, the velocity decay profiles along the jet centerline followed a complete different path with different decay rates comparing to other cases considered herein. This strengthened the conclusion that this flow was associated with a different class of crossflowing jets. It was reported that the main advantage of employing r^2D length scale as non-dimensionalizing factor is to discriminate jet near- and far-field regions (Mungal and Smith 1998).

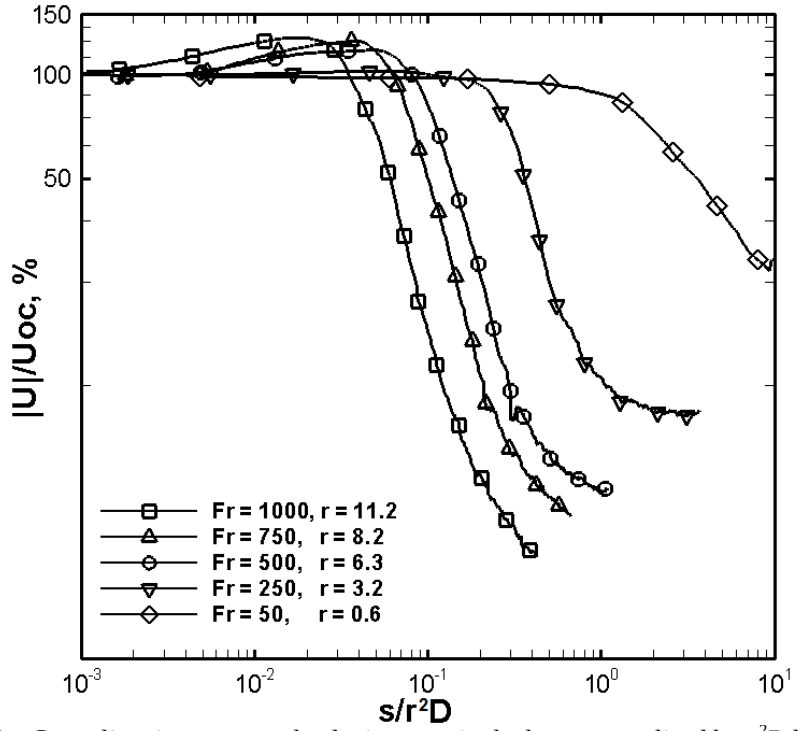

Figure 3.25 – Centerline time-averaged velocity magnitude decay normalized by r^2D length scale

The position of the branches using r^2D length scale for $Fr \geq 250$ aligned approximately at s ≈ 0.3 r^2D, corresponding to y ≈ 0.2 r^2D. It can be concluded that for these cases the region y/ r^2D < 0.2 may be considered as the jet near-field region at which r dependent properties of the crossflowing jet such as the formation of the counter-rotating vortex pair structure are developing (Mungal and Smith 1998). On the other hand regions with $y/ r^2D > 0.2$ corresponded to jet far-field region at which jet flow structure was reached a fully developed self-similar states.

3.3.5 Time-averaged Velocity Profiles

The radial velocity profiles at several downstream locations along the jet centerline coordinate, s, normalized by global rD factor versus n-coordinate (see Figure 3.18) are presented in Figure 3.26, and same as free jet cases, L_u represented the radial location at which the time-averaged velocity was observed to be half of the centerline velocity.

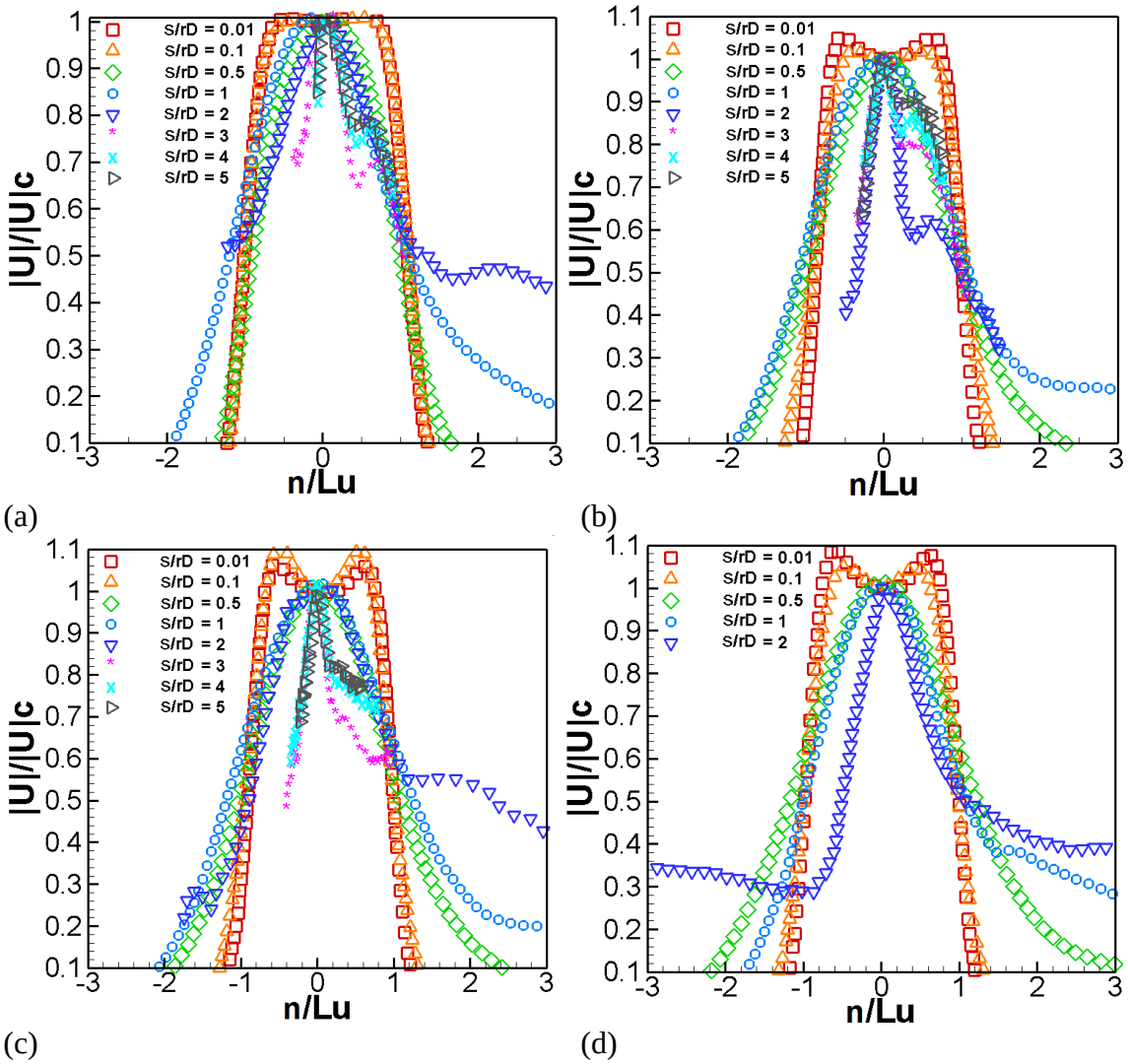

Figure 3.26 – Radial velocity profiles, jet in crossflow Fr = (a) 250, (b) 500, (c) 750 and (d) 1000.

The results for *Fr* = 50 are not shown in this figure because of plume-like structure of the resultant flow structure. Figure 3.26 show that radial profiles at *s/rD* = 0.01 and 0.1 were observed to be symmetric and can be approximated by a Gaussian distribution. The radial profiles at the jet near-field regions were similar to those of free jet flows since the jet flow was dominated by initial jet momentum and was very weakly advected. The saddle-back velocity profile of the sharp-edged inflow condition was observed at the jet near-field region. The saddle-back profile were more pronounced in

cases with higher Froude numbers and were negligible for Fr = 250. For Fr = 250 a bell-shaped velocity profile similar to those of contoured nozzle inflow condition was observed.

Farther downstream, it was evident that time-averaged radial velocity distributions departed from symmetry. For downstream locations with s/rD > 0.1, the radial velocity distributions showed two distinct peaks with one near the jet centerline and with the other weaker peak near the jet's inner boundary. As flow evolved, for s/rD > 3, the peak near the jet centerline weakened and two peaks were observed to join together to form a more symmetric profile. The radial profiles at s/rD > 3 for Fr = 1000 are not shown in the figure since the radial velocity profiles did not reach the half maximum value, $L_{u,}$ in the imaging plane. It should be noted that lowering the Froude numbers resulted in a better mixing between the jet and the crossflow structure which widened the jet structure at the jet far-field regions. This led to a wider velocity distribution profile and a larger L_u value subsequently which scaled down the resultant velocity profiles comparing to those at the jet near-field. In order to illustrate the downstream evolution of the jet in crossflow flow structure the normalized velocity profiles at several downstream locations along fixed (x, y)-coordinate system is presented in Figure 3.27.

Time-averaged crossflow subtracted velocity profiles at different fixed y/rD locations and time-averaged velocity magnitude at fixed x/rD locations are shown in the figure. Velocity components are normalized by time-averaged nozzle exit velocity where x and y-coordinate systems were normalized by global rD factor. Symmetric velocity profiles were observed at jet near-field regions (i.e. x/rD = 0.1).

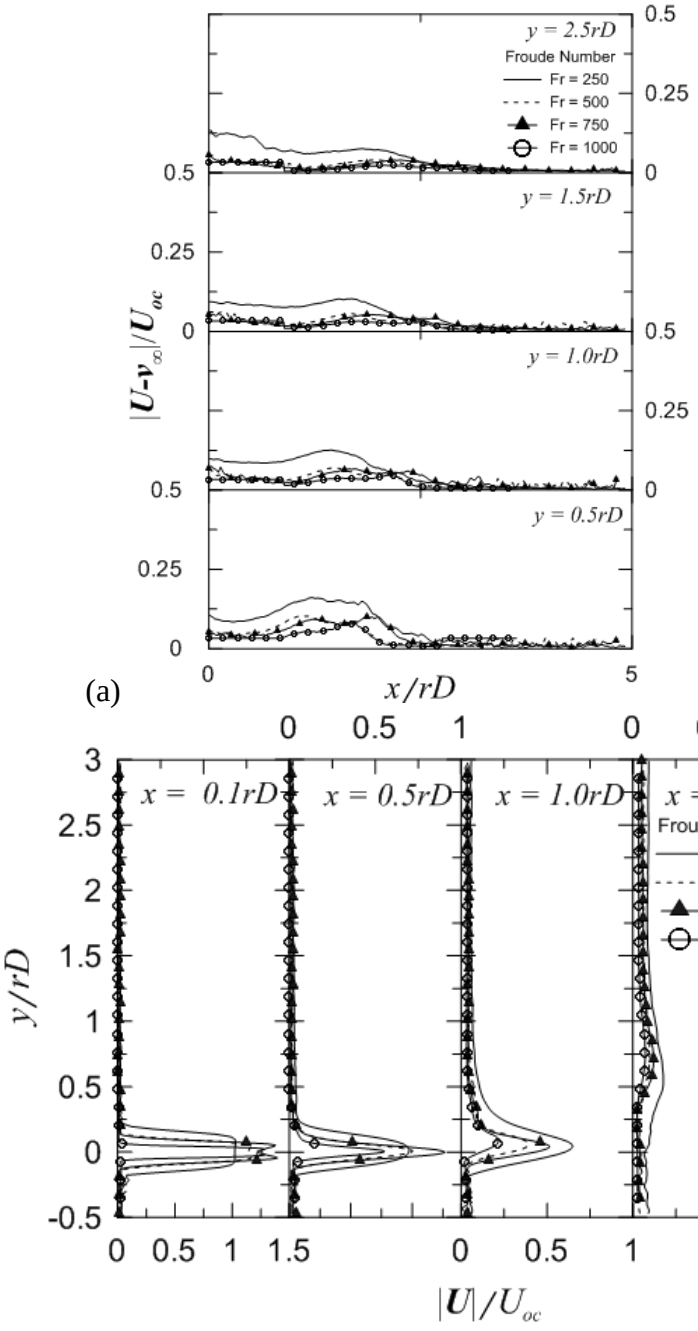

Figure 3.27 – Time-averaged normalized velocity magnitude profiles of the jet in crossflow, (a) Profiles of Averaged crossflow subtracted velocity magnitude, and (b) Profiles of velocity magnitude

Farther downstream, the velocity profiles departed from symmetry. At *x/rD* = 1.0, the secondary peak in velocity profiles started to form as shown in Figure 3.26. The time-averaged crossflow subtracted velocity profiles (i.e. $<|\boldsymbol{U}-v_\infty|>$) showed a noticeable asymmetric profile with two distinct peaks. However, for the case of

velocity profiles at fixed *y/rD* locations, the stronger peak was seen near the inner boundary of the jet and another weaker peak near the jet centerline. Same behavior was also reported by (Su and Mungal 2004). The reason for this behavior was that when fixed location in the (*x, y*) coordinate system was considered instead of (*s, n*) coordinates of the jet, the velocity profiles might not show the actual evolution of the jet in the normal planes. It can be concluded that for the cases of jet in crossflow, (*s, n*) coordinate system can show the jet downstream evolution more accurately. At *y/rD*>1.0, the peak near the centerline weakened and disappeared at the far-field locations which led to a roughly symmetric profile.

3.3.6 Turbulence Statistics

Downstream evolution of normalized rms values of fluctuating velocity components (i.e. $u'/|U|c$ and $v'/|U|c$) along the jet center coordinate system are plotted in Figure 3.28. Two different scaling factors of *rD* and *D* were used in normalization of jet coordinate system, *s*. The corresponding values for the case of *Fr* = 50 are not shown in the figure because of plume-like structure of the resultant flow. Same as the free jet flows, low initial values were observed in velocity fluctuation components as a result of sharp-edged orifice inflow condition.

These turbulence intensity values increased rapidly to peak values downstream of the potential core area. The peak values in the cases of crossflowing jets were more evident comparing to free jet flows. The turbulence intensity of *Fr* = 250, 500 and 750 reached to maximum values of approximately 0.4. However, the maximum value of 0.3 was observed for *Fr* = 1000. This difference in peak values may be explained by high

jet-to-crossflow ratio (i.e. r =11.2) for Fr = 1000 which was approximately twice the value for Fr = 500. High r values may lead to a momentum dominated jet flow which is weakly advected by the crossflow structure. This weak advection led to the smooth deflection of the jet towards the direction of crossflow field. On the other hand for the cases with low r values the lower initial momentum of the jet resulted in a stronger crossflow advection and sudden turn of the jet flow towards the direction of crossflow which would led to higher turbulence intensity values in these cases.

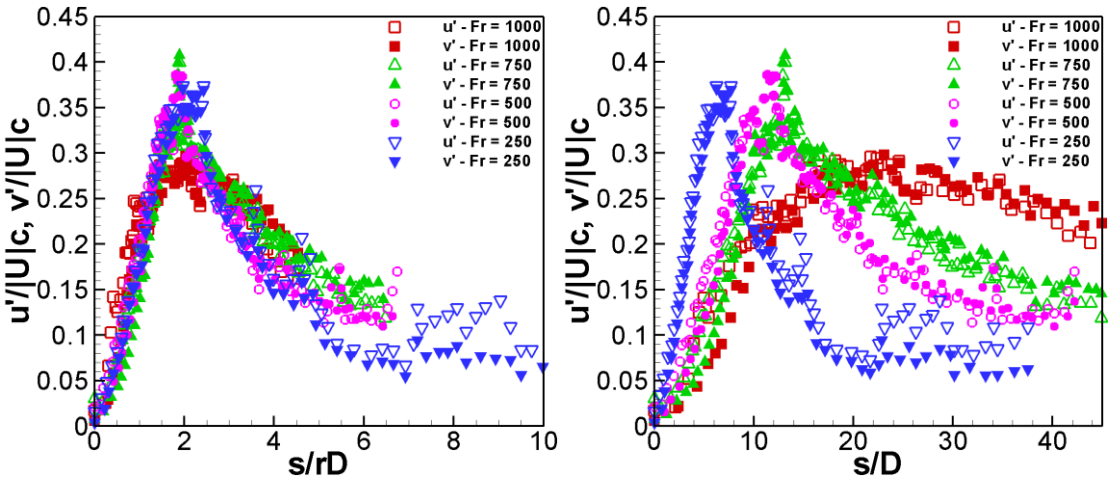

Figure 3.28 – Normalized velocity fluctuations along jet center line, jet in crossflow, jet centerline normalized by rD (left) and nozzle diameter (right).

The rms profiles collapsed using rD length scale as the normalizing factor. However, using D-scale caused the peak values in rms profiles to shift towards farther downstream locations in higher Froude numbers. Using D as normalization factor led to appearance of r-dependent characteristics of crossflowing jets. The peak values in turbulence intensity plots were observed at approximately s =1.8 rD for all the cases considered herein and at s = 7D, 11D, 13D and 23D for Fr = 250, 500, 750 and 1000 respectively.

The turbulence intensities for jet in crossflow were observed to reach a substantially higher peak values, compared to free jet flows (almost twice in magnitude). Similar to free jet flows the axial fluctuations were generally higher than the radial fluctuations. The axial and radial fluctuation values for the cases of Fr = 750 and 500 approached the asymptotic value of 0.14 and 0.13 at $s = 5rD$ respectively. For Fr = 1000 the rms values did not reach an asymptotic value in the range considered in this study but it was expected to follow a similar trend. For Fr = 250, the axial and radial turbulence intensity values approached asymptotic values of 0.09 and 0.07 respectively at $s = 7rD$. The asymptotic ratio of $v'/u' \approx 0.85$ was observed in cases considered herein which is slightly higher than the values of free jet flows.

Axial fluctuations were slightly higher than the radial fluctuations for all cases considered herein at the jet near-field regions. The axial and radial turbulence intensities were observed to be approximately equal at downstream of potential core region where crossflow momentum forced the jet to turn towards the crossflow direction. Downstream of the jet turning point towards the crossflow direction, the axial rms values were observed to be higher than radial components as a result of the formation of the wake vortices. It should be noted that this condition was only reached in Fr = 250 and other Froude numbers did not reach this stage in the considered ranges.

Components of turbulence kinetic energy at different downstream locations along the jet centerline for Fr = 1000 and 250 are shown in Figure 3.29. The turbulent stress components were normalized by time-averaged nozzle exit velocity, U_{oc}, and have been plotted against n-coordinate normalized by global rD length scale in jet coordinate system. Due to qualitative similarities in plots for considered cases, the stress profiles

related to *Fr* = 1000 and 250 are presented here as they represent momentum and buoyancy dominated flows respectively.

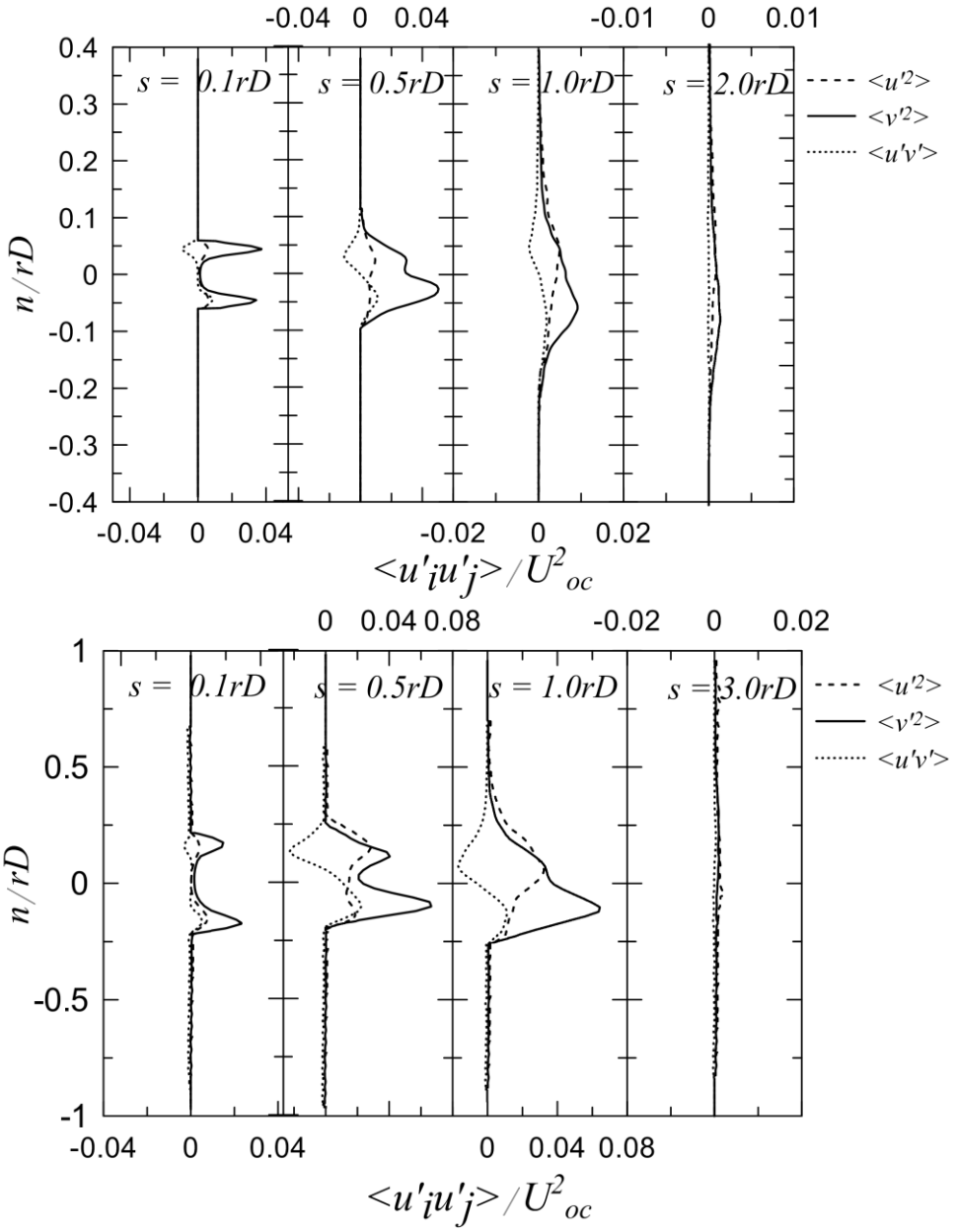

Figure 3.29 – Stress profiles in jet center-plane for jet in crossflow cases. (a) *Fr* = 1000, (b) *Fr* = 250.

Near the jet exit at *s* = 0.1*rD*, axial and radial components of averaged normal turbulent stresses showed two distinct peaks at the jet near-field region where jet initial momentum forces were dominant. These shown jet shear layer instability along jet's

outer and inner boundary at the jet potential core region. Due to the strong pressure gradient in *y*-direction at jet's potential core region, and weak crossflow advection, the $<u'^2>$ component of turbulent stresses showed higher values comparing to radial component $<v'^2>$ and shear stress $<u'v'>$. At $s = 0.5rD$, in the potential core region, normal stresses profiles still showed two distinct peaks but the strong pressure gradient in *y*-direction suppressed the peak in $<v'^2>$ near the jet outer boundary. Strong interaction between jet and crossflow field in jet outer boundary weakened the axial normal stress component, $<u'^2>$ in windward side of the jet. The turbulent shear stress, $<u'v'>$, instabilities became stronger in those locations as a result of high mixing between jet and crossflow structure.

Farther downstream, at $s > 1.0rD$, approximately at the end of potential core region, the peak values in axial and radial component of turbulent normal stresses were comparable showing a single peak profiles. However, the maximum of $<u'^2>$ occurred closer to the jet's outer boundary and the maximum of $<v'^2>$ were located closer to the inner boundary of the jet. This misalignment of the peaks continued throughout the measurement region.

The turbulent shear stresses values, $<u'v'>$, showed a positive peak near the jet's outer boundary and the other peak near the inner boundary which were also resulted from the jet shear layer instability. The peak values in jet near-field regions were smaller in magnitude comparing to turbulent normal stresses. As the jet evolved at the far-field locations, the higher interaction and mixing between the jet and crossflow led to the higher generation of $<u'v'>$. At the potential core region, the peaks in turbulent shear stress profiles were aligned by the jet centerline and the magnitude of the positive

peak were slightly dominant due to higher interactions between jet and crossflow in these regions. Downstream the potential core area, at $s > 1.0rD$, regions of negative were dominated slightly. The regions of positive $<u'v'>$ in windward side of the jet were observed to become weaker relative to negative peak at farther downstream locations along the jet centerline coordinate as the jet bent towards the crossflow direction. The $<u'v'>$ profiles shifted towards the jet's outer boundary in these locations as the mixing between jet's inner boundary and crossflow field became the dominant mechanism for $<u'v'>$ generation.

3.3.7 Flow Structure in Crossflowing Jets

3.3.7.1 Vorticity

The vortical structure of the jet in crossflow consists of four general regions (Fric and Roshko 1994). The horse shoe vortices wrap around the jet column in jet near-field region. The jet shear layer or ring vortices which occur at the jet outer boundary in the region where it bends towards the crossflow direction. The wake structure forms in the area between the lee side of the jet and the wall boundary downstream of the jet column and convects at the jet far-field locations. Finally, counter-rotating vortex pair which is the dominant vortex structure after jet has turned towards the direction of crossflow. The schematic of the vortical structure of jet in crossflow is presented in Figure 3.30.

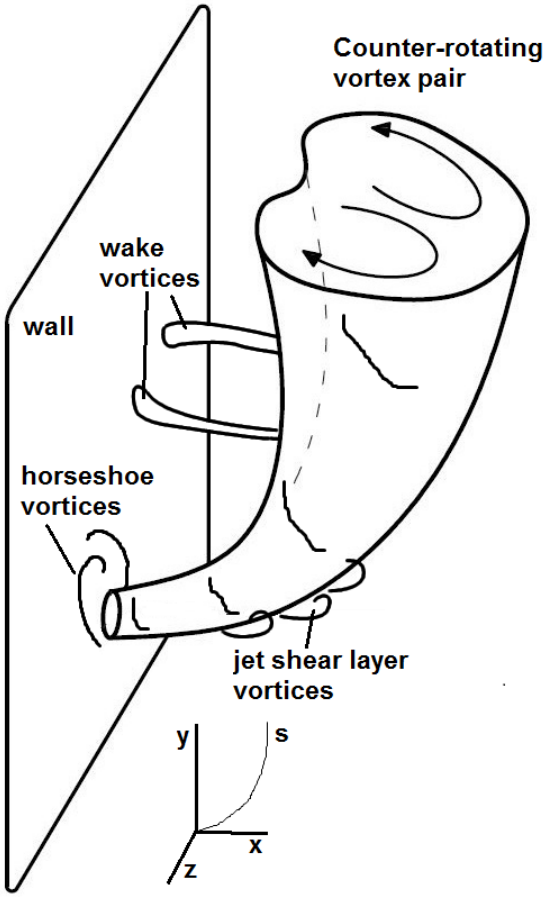

Figure 3.30 – Schematics of jet in crossflow vortical structure (re-drawn from (Fric and Roshko 1994))

An example of instantaneous PIV image with corresponding velocity field of jet center plane for Fr = 250 is illustrated in Figure 3.31. Similar behavior was observed for higher Froude numbers as well so resultant vortical structure of Fr = 250 are explained as an example here. Velocity field was normalized by time-averaged nozzle exit velocity and x- and y-coordinate were normalized by the jet diameter, D. The Jet outer boundary at the jet near-field regions was observed to be much thinner comparing to the inner boundary.

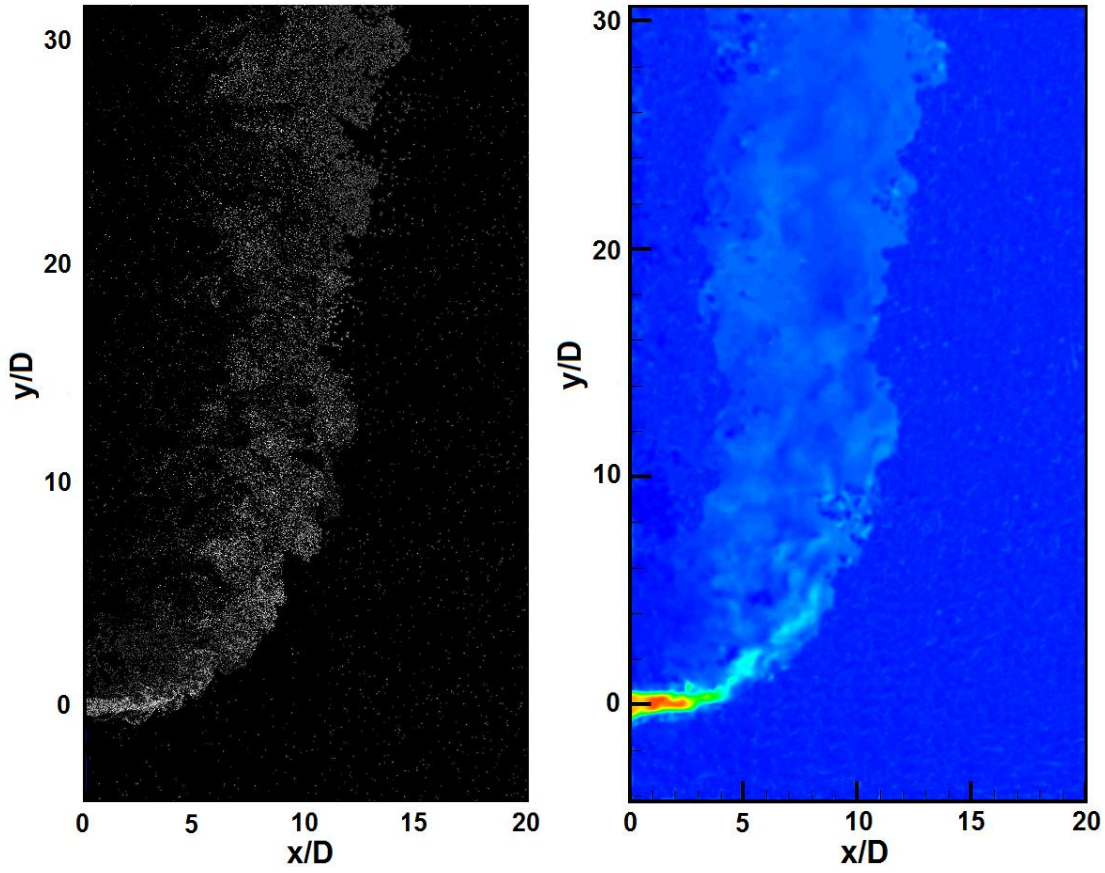

Figure 3.31 – Instantaneous PIV image (left), Corresponding Velocity Field (Right), *Fr* = 250

The crossflow field retarded the outer boundary of the jet with less entrainment in the jet potential core area ($x < 5D$) and forced the jet structure to deviate from the nozzle axis. On the other hand in the same region, the lee side of the jet accelerated and widened in order to balance the mass flow rate (Crabb, Durao and Whitelaw 1981).

At the jet far-field regions ($y > 8D$), the jet inner boundary were observed to be widened as a result of the presence of wake vortices. Wake vortices were formed at the location where the crossflow structure reached the jet lee side area. Farther downstream, the jet inner boundary region corresponded to regions of very high crossflow entrainment with high mixing characteristics.

Averaged velocity magnitude field for Fr = 500 is shown in Figure 3.32 in order to better describe the bifurcated structure of jet in crossflow. The bifurcated structure of the crossflowing jet is evident in Figure 3.32. This bifurcated structure was observed to be more pronounced in regions where the jet flow deviated from the nozzle axis and was bent in the direction of the crossflow. As shown in the figure, one of the branches was observed to be near the outer boundary of the jet and evolved from the initial jet. Points of maximum velocity magnitude and jet centerline as the result were located in this region. The other branch was located in the lee side of the jet and was initiated approximately from the end of potential core area and was turned sharply into the wake side of the jet.

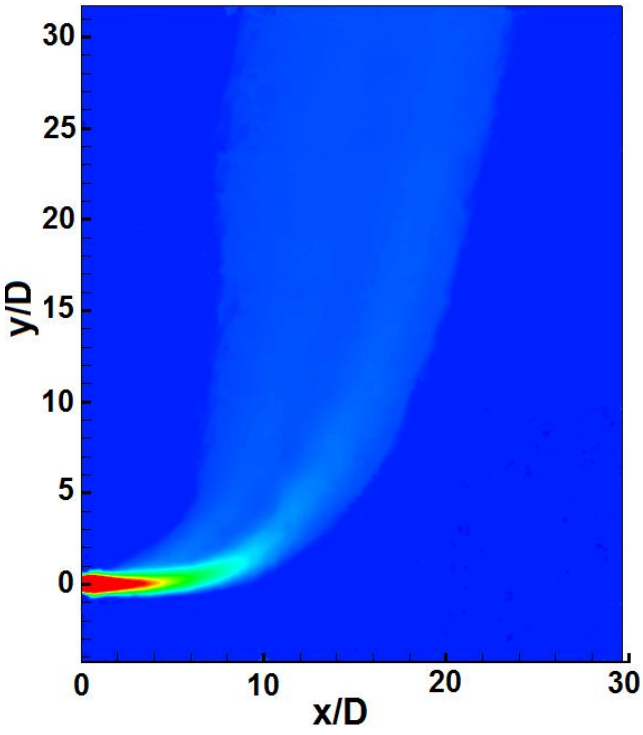

Figure 3.32 – Time-averaged velocity magnitude field, Fr = 500

Downstream of the potential core region the centerline velocity profile decayed gradually leaving the jet structure more vulnerable to the crossflow stream.

Downstream of the potential core region the jet outer boundary decelerated and was observed to turn towards the direction of the crossflow whilst the lee side of the jet was accelerated to maintain the overall mass flow rate. According to (Andreopoulos 1983) this flow acceleration, forces the lee side of the vortex rings to stretch strongly for several diameters in downstream direction. Stretched side of the successive vortices can join together to form a bound vortex which can initiate regions of strong turbulence. Bound vortices might be a starting point for formation of counter rotating vortex pair and the secondary branch in lee side of the jet.

At the jet far-field regions, the relative velocity gradient between windward and lee side of the jet was observed to become smaller and smaller and the resulting vorticity diffused gradually. At some point downstream, depending on the *r* value and the jet *Re* number, the propagation of wall boundary layer and wake structure in lee side of the jet or both retarded the lee side of the jet which led to an opposite vorticity region (Andreopoulos 1983). It should be noted that the model described above is a possible scenario for an ideal laminar jet discharged in a crossflow and in order to apply this model to a turbulence flow, the vortex rings should be replaced by eddies containing vorticity.

Vorticity plots for the cases considered herein are presented in Figure 3.33. It should be noted that not all the steps stated in above model were observed in measurement regions considered here. Similar to free jet flows increasing vorticity magnitude were observed by increasing the Froude number. Maximum vorticity values were adjacent to nozzle tip and at farther downstream regions the vorticity values were decreased.

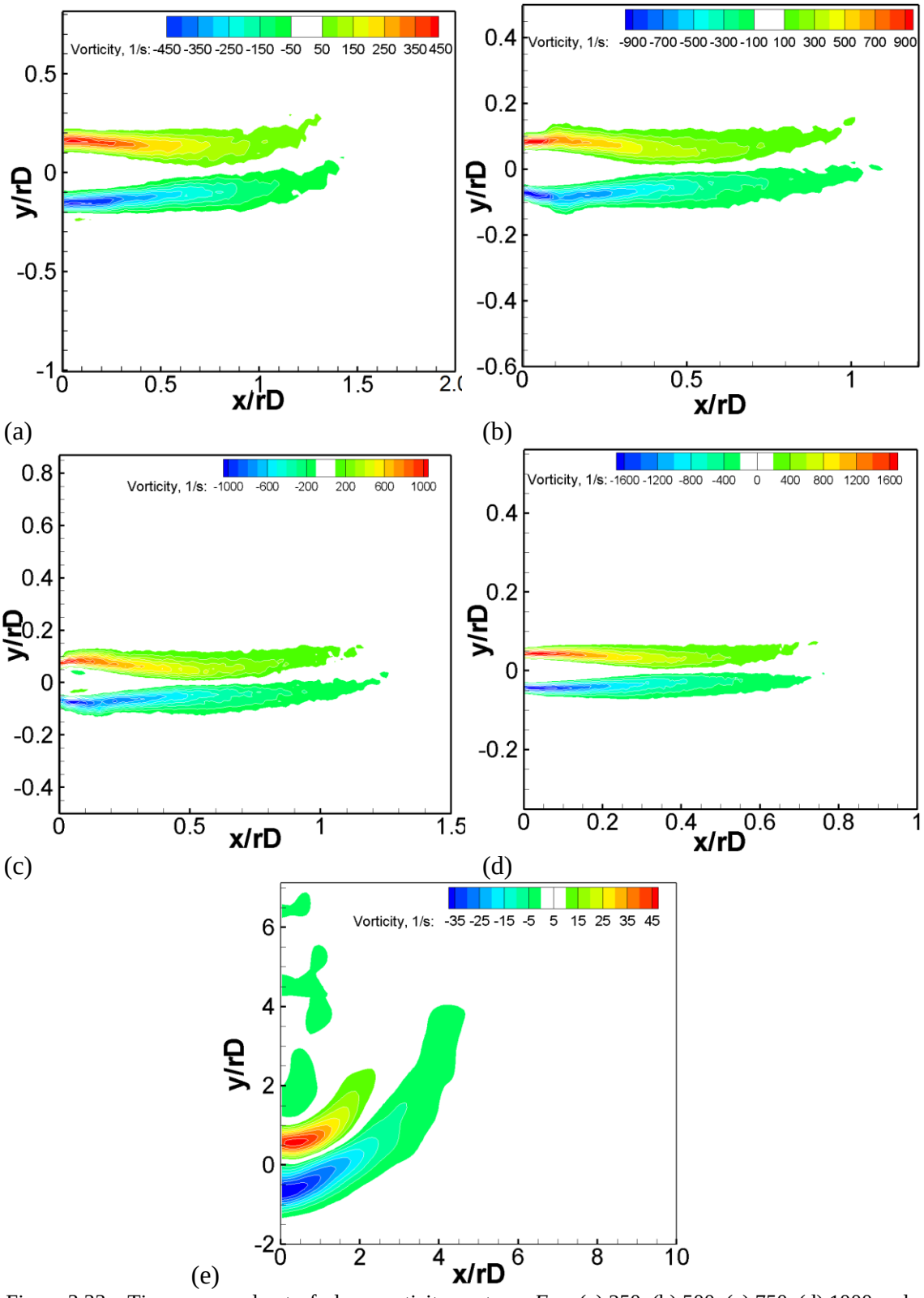

Figure 3.33 – Time-averaged out-of-plane vorticity contours *Fr* = (a) 250, (b) 500, (c) 750, (d) 1000 and (e) 50.

At the jet potential core region, the vorticity fields were observed to be similar to those of free jet flows for $Fr \geq 250$. For $Fr = 50$, the jet structure collapsed downstream of a very short potential core region due to the low jet-to-crossflow velocity ratio which led to a plume-like flow structure. The circulation regions widened at the jet far-field regions. For $Fr \leq 750$, downstream of the potential core region, the circulation region corresponding to the negative vorticity near the jet outer boundary extended more comparing to the other side. This was due to strong interaction between crossflow and the jet outer boundary which forced the outer boundary to turn and to decelerate. The inner boundary of the jet accelerated to balance the mass flow rate. This together with turning of the outer boundary suppressed the circulation and mixing of the jet inner boundary downstream of the potential core region. These steps were more pronounced in $Fr = 50$ due to low initial jet momentum fluxes. The vorticity field for $Fr = 1000$ was very similar to those of free jet flows in the jet near-field region, due to the high r value comparing to other cases, which prevented the jet from sharp turnings towards the crossflow direction.

For high Froude numbers (i.e. $Fr \geq 250$) the higher initial momentum of the jet resulted in a further penetration in the crossflow field and a more extended potential core region. This delayed the formation of bound vortices and also led to a more pronounced bifurcated structure. The distance between two branches in the windward and the lee side of the jet was more evident in higher Froude numbers. Decreasing the Froude number reduced the distance between two branches of the resultant bifurcated structure. For instance in the case of $Fr = 250$, the maximum distance between two

branches were approximately one diameter whilst the maximum distance between branches for *Fr* = 500 was observed to be approximately 2*D* as shown in Figure 3.32.

3.3.7.2 Streamlines

Flow stream traces presentation is an intuitive tool to visualize the flow patterns. Flow stream traces determined from the jet center-plane time-averaged velocity field is shown in Figure 3.34.

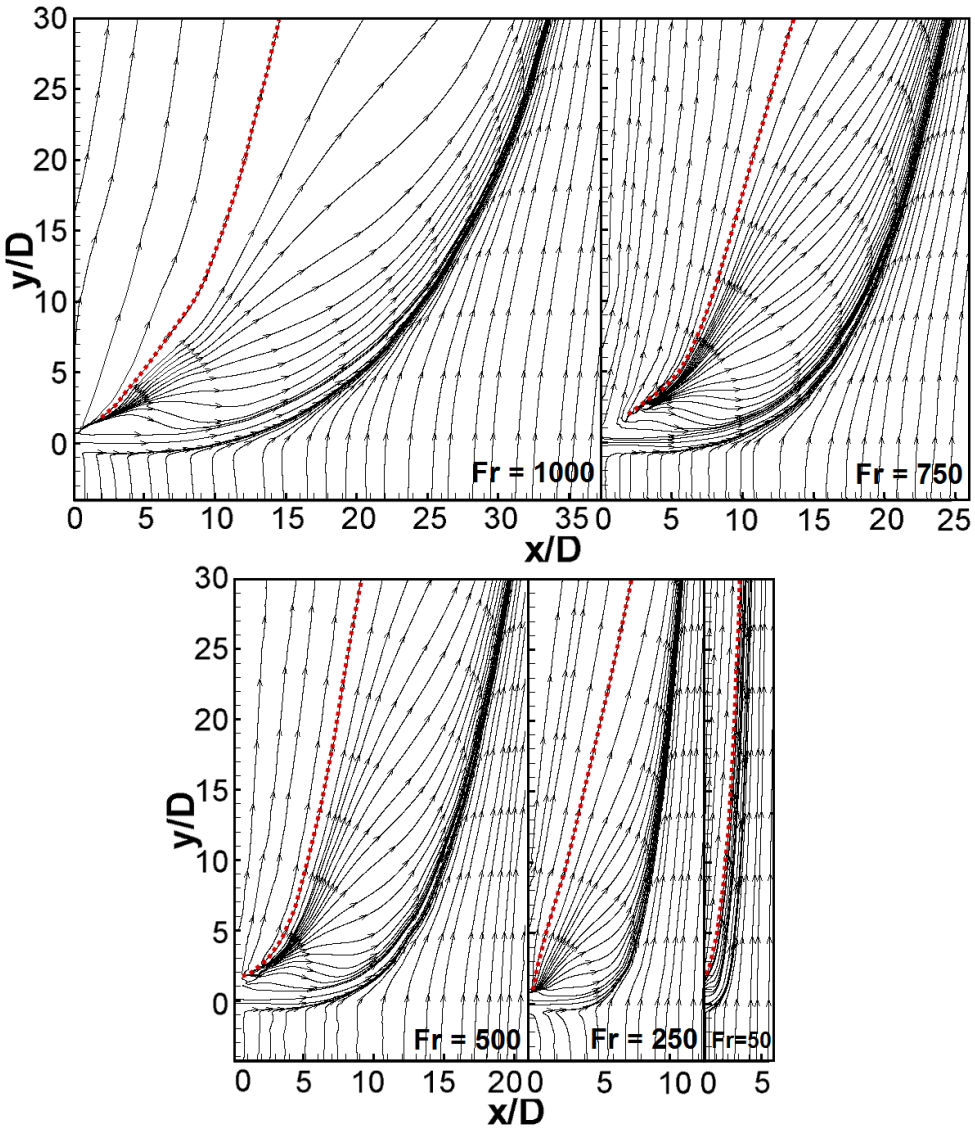

Figure 3.34 – Flow streamlines of jet center-plane determined form the time-averaged velocity field

The spacing between streamlines and initial points were selected arbitrarily and do not necessarily shown the stream function values.

The jet outer boundary streamlines showed a general waviness pattern. This wavy pattern was also reported by (Hama 1962) and (Su and Mungal 2004). They reported that this behaviour was resulted in by the very high velocity gradient between jet's outer boundary and crossflow which led to a significant three-dimensionality in flow and resulted in an efficient mixing and a convoluted flow field. By decreasing the Froude number it was observed that this wavy pattern moved closer to the initial jet region which can be explained by jets initial momentum forces: starting form the lower edge of the nozzle in windward side of the jet and moving along the jet outer boundary, jet initial momentum decayed by the influence of the crossflow which led to the flow deceleration adjacent to this boundary. Flow kinetic energy dissipated into heat and turbulence kinetic energy. Increase in turbulence kinetic energy of the jet led to the production of turbulent eddies. However, this process was observed to be dependent on the r value and the jet initial inflow condition.

The streamline pattern also provided a good visualization of the flow boundaries. As shown in Figure 3.34, the outer boundary of the crossflowing jet may be identified as the boundary with cluster of stream traces which approximately follow the flow centerline. For lower Froude numbers, the jet outer boundary turned more quickly into the crossflow direction and the overall jet structure penetrated less into the crossflow as a result of the lower initial momentum. In the lee side of the jet some flow streamlines originating from stagnation point, turned towards the jet centerline with an inflection point. The jet inner boundary may be quantified as the line in the lee side of the jet

which separates these streamlines with an inflection point and those with positive concavity. The approximate position of the jet inner boundary is identified in Figure 3.34 by a dashed line. As it is shown the figure, the inner boundary was moved closer to the wall by decreasing the Froude number. The jet width which is identified as the distance between outer and inner boundary became narrower by decreasing the Froude number.

For Fr = 50, the crossflow momentum forced the jet to move adjacent to the wall with a narrow overall jet structure. Increasing the Froude number, a stagnation point with positive divergence towards the lee side of the jet appeared in jet near-field region which moved to farther downstream location for higher Froude numbers. For instance for Fr = 250, the stagnation point is approximately located in lee side of the jet at (x, y) ≈ (0.2D, 1.1D) versus (1D, 1.5D) for Fr = 1000. No stagnation point was observed in the windward side of the jet and crossflow stream lines were observed to entrain into the jet flow.

3.3.8 Flow Width in Crossflowing Jets

In order to better understand the jet flows in crossflow, the interaction of the jet boundary layer and boundary layer generated by the wall surface adjacent to the orifice (see Figure 3.17) is of great importance. Low wall and jet boundary layers interactions was one of the main objectives in designing of the experimental setup. This was to minimize the surroundings intrusion in the overall jet structure. It has been reported that in crossflowing jets near a surface, the wall boundary layer turbulent contribution to the overall turbulent quantities approaches to zero in far downstream regions

(Andreopoulos 1983). However, the downstream distance at which this takes place is difficult to estimate. Andreopoulos (1983) also reported that this distance depends on relative length scale sizes for a given jet-to-crossflow velocity ratio. He concluded that for cases with $D \gg \delta$ at jet orifice, the wall boundary contribution to the overall turbulent quantities is negligible. Where δ is wall boundary layer thickness (see Figure 3.35).

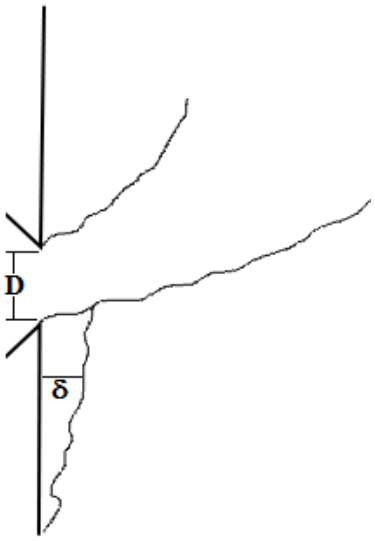

Figure 3.35 – Flow configuration as function of D and δ for $D \gg \delta$ cases (Andreopoulos 1983).

In order to calculate the wall boundary layer at the jet's orifice, the crossflow has been assumed to be fully developed turbulent from the leading edge of the wall surface. Wall's turbulent boundary layer was calculated using the $1/7^{th}$ law to be $\delta/D = 0.09$ at the orifice and 0.4 at the top of the imaging plane ($y/D = 30$). So it was expected that wall boundary layer would cause a minimal contribution in the overall turbulence quantities of the crossflowing jet. This might not be true for the case of Fr = 50, because of the plume-like structure of the resultant flow.

The boundary contours for the time-averaged velocity field for $Fr = 1000$ centerplane together with jet centerline are shown in Figure 3.36. The boundary

contours (solid line) represent the loci of points at which the local time-averaged velocity is 20% of the jet centerline (dashed line) values. This was computed by first finding the maximum time-averaged velocity values and then marching in the normal direction at each downstream location along the jet centerline until the velocity values dropped to 20% of the centerline values. The asymmetric structure of the crossflowing jet structure is evident in the figure. The jet flow was forced away from the windward side of the jet and was deposited to the lee side by the crossflow.

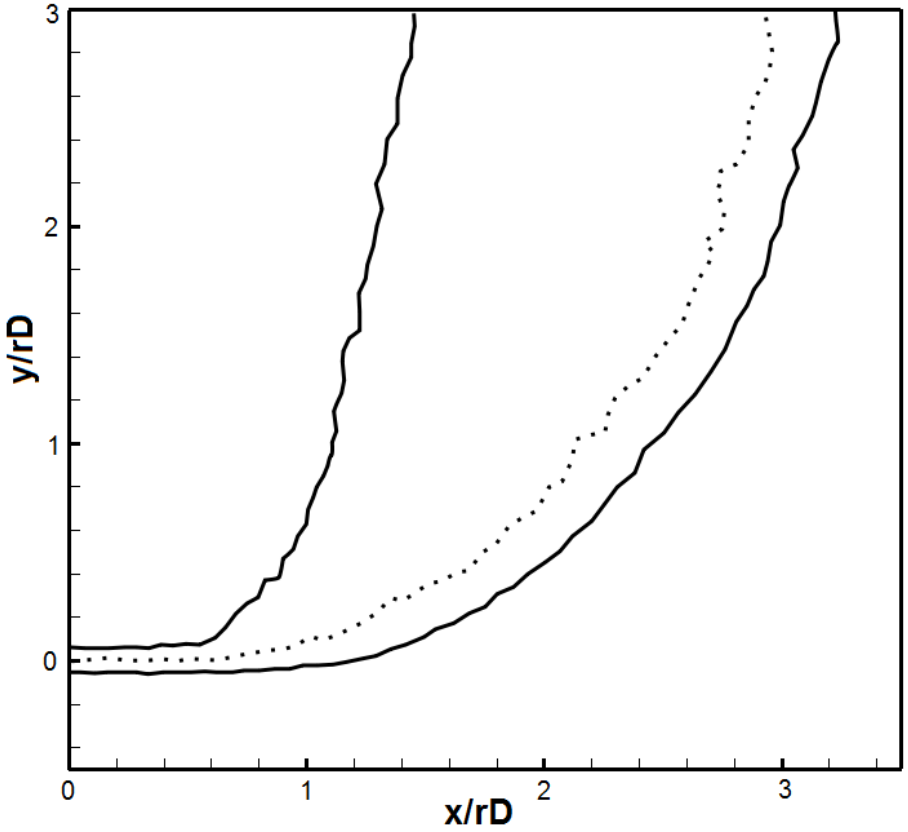

Figure 3.36 – Boundary contours for time-averaged velocity field, Fr = 1000.

The dependency of the flow widths on the centerline coordinate system, *s*, is shown in Figure 3.37. Since the flow was not symmetric about the jet centerline it was important to determine these partial widths for +*n* direction (lee side) and –*n* direction

(windward side) separately. The nominal half-widths were calculated as the distance between boundary contours and the jet centerline at each point. These partial widths are denoted as $\delta+$, $\delta-$ and δ_t for jet half width in lee-, windward-side and jet full width respectively. In order to have better visual representation, the flow widths for Fr = 250 are presented in a separate plot.

(a)

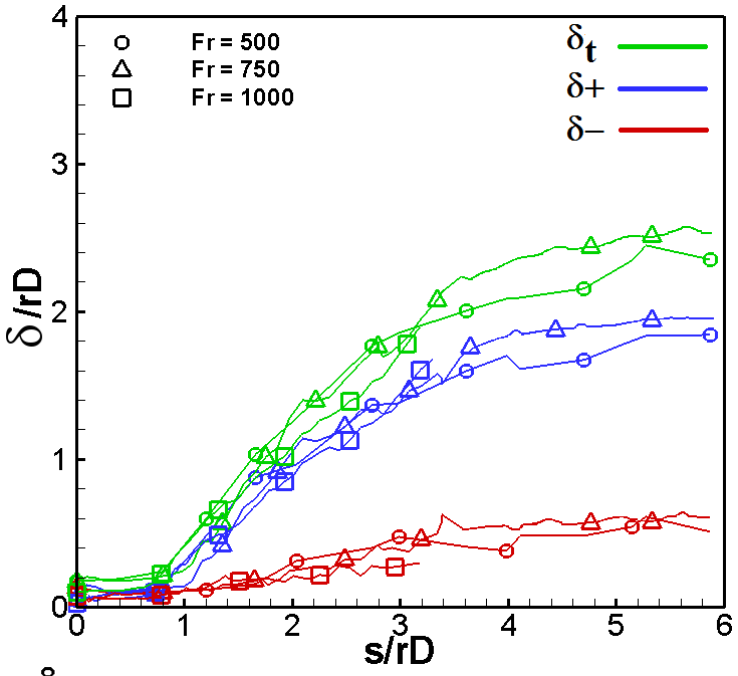

(b)

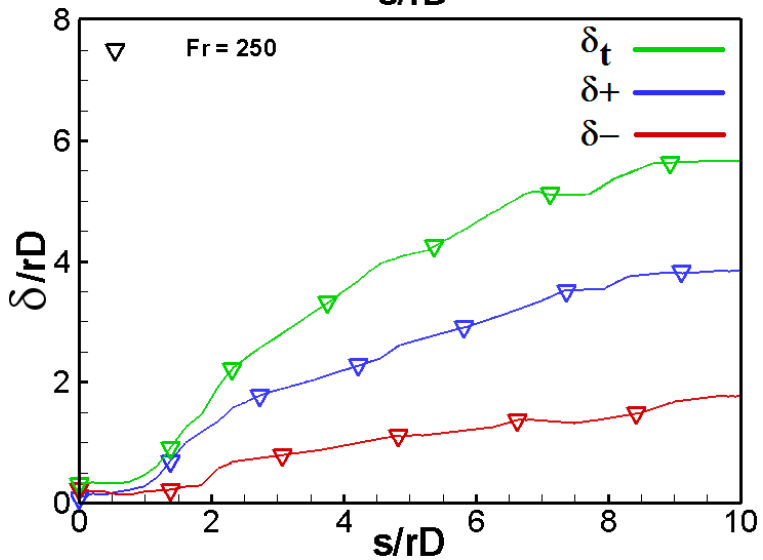

Figure 3.37 – Flow widths in jet centerplane for crossflowing jets, Fr = (a) 1000,750 and 500, (b) 250.

The asymmetric structure of the resultant jet is evident in partial widths and it is clear that $\delta+ > \delta-$. The jet widths plots almost collapsed on each other for $Fr \geq 500$ but for $Fr = 250$, as the jet-to-crossflow ratio decreased, the jet structure was observed to be more vulnerable to the crossflow field and flow widths were slightly larger. The flow full width growth rates exceeded those of free jet flows and transitioned to a slower growth rate at the jet far-field locations.

3.4 SURFACE EFFECTS

Physical aspects of a fluid flow near a barrier were always a topic of interest in fluid dynamics. In this section the physical properties of a horizontal jet near a surface boundary are presented. Two different cases of $Fr = 1000$ and 250 were considered as the flow conditions. $Fr = 1000$, represented a momentum dominated flow in which buoyancy forces were negligible. On the other hand $Fr = 250$ was chosen as a case in which buoyancy effects were more pronounced. Three different boundary conditions were considered, namely: ground, ceiling and vertical wall. In order to characterize the increasing effects of boundary condition on the jet flow two different distances of $1D$ and $3D$ (where D is the nozzle diameter) from the surface of the boundary to the center of the nozzle were considered. Schematic of experimental setup for jet flows adjacent to the ground boundary is shown in Figure 3.38 as an example. For the jet flows adjacent to the ceiling and the vertical wall, similar experimental setups with surfaces placed above and at the side of the jet were used respectively. Different surface orientations are shown in Figure 2.5.

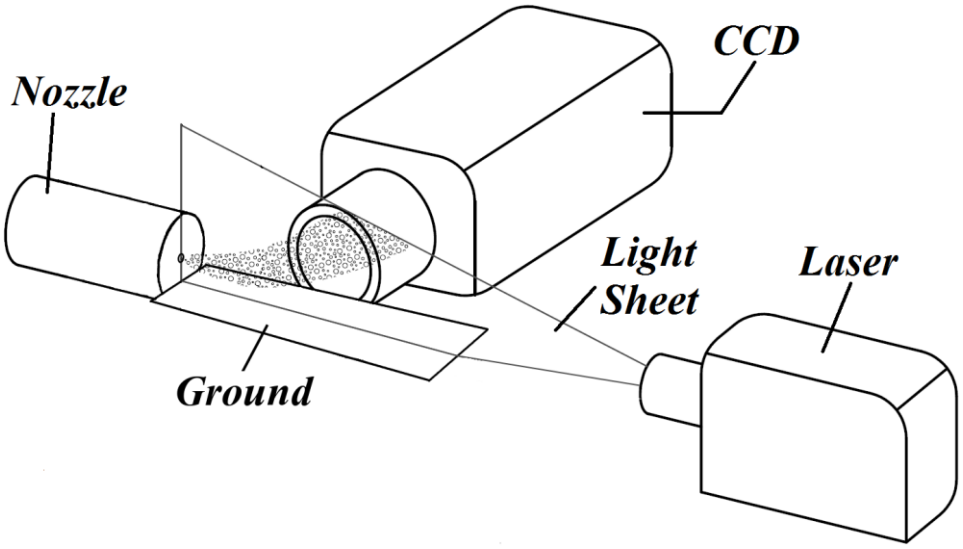

Figure 3.38 – Schematic of experimental setup for ground boundary.

In a turbulent jet flow near a surface, depending on the distance between the surface and the nozzle, the entrainment of ambient into the jet boundary can be significantly influenced by the surface. The presence of a boundary near a jet can significantly restrict the ambient entrainment and mixing characteristics of the flow. The flow velocity profiles in jet flows adjacent to a surface undergo a sharp velocity drop near the boundary surface as a result of no-slip boundary condition. According to Bernoulli's principle this deformation in velocity profiles develop a pressure difference across the jet which forces the overall jet structure towards the surface. This force will be addressed as the surface force in this section.

If the distance between the surface and the nozzle axis is short enough, there will be a dynamic attachment between the jet and surface. This point is called the attachment or also reattachment point and is inevitable because of the entrainment and mixing nature of the jet with its surroundings. The limited ambient entrainment near the wall surface leads to the low pressure effects which will force the jet to be deflected closer to the surface and production of so called wall-jet structure. This force is more pronounced in

cases with higher Froude numbers (i.e. higher initial momentum) as a result of greater dynamic pressure difference between the wall and free sides of the jet.

The mixing process and characteristics of the flow near a boundary surface after the attachment point are governed by wall-jet dynamics. Turbulent wall-jet flows consist of two different layers, a wall layer which is adjacent to the surface and an outer layer which is farther away from the surface. These two layers are separated by a mixing or transition layer. The velocity profiles experience a maximum value in the transition layer.

Mixing rates of wall-jets are reported to be significantly lower comparing to those of free jets (Volker and Johnston 1993) which would theoretically reduce the velocity decay rates of the resultant flow. Lower velocity decay rates led to farther extension of jet structure in downstream locations. Limited information about the effects of buoyancy and inflow condition on wall-jets with different surface orientations is available in literature. The physical characteristics of horizontal turbulent jets in the vicinity of ground, ceiling and vertical wall are presented in following sections.

3.4.1 Jet Centerline

Jet centerlines for different surface orientations are presented in following subsections. Due to small distances between the nozzle axis and the wall surface and the flow tendency to deviate from the nozzle axis, it was preferable to use the jet coordinate system introduced in section 3.1. Points of maximum time-averaged velocity were used at each downstream location to identify the jet centerline, similar to the free jet cases.

3.4.1.1 Ground

The corresponding centerlines for the jet flowing over the ground surface are presented in Figure 3.39.

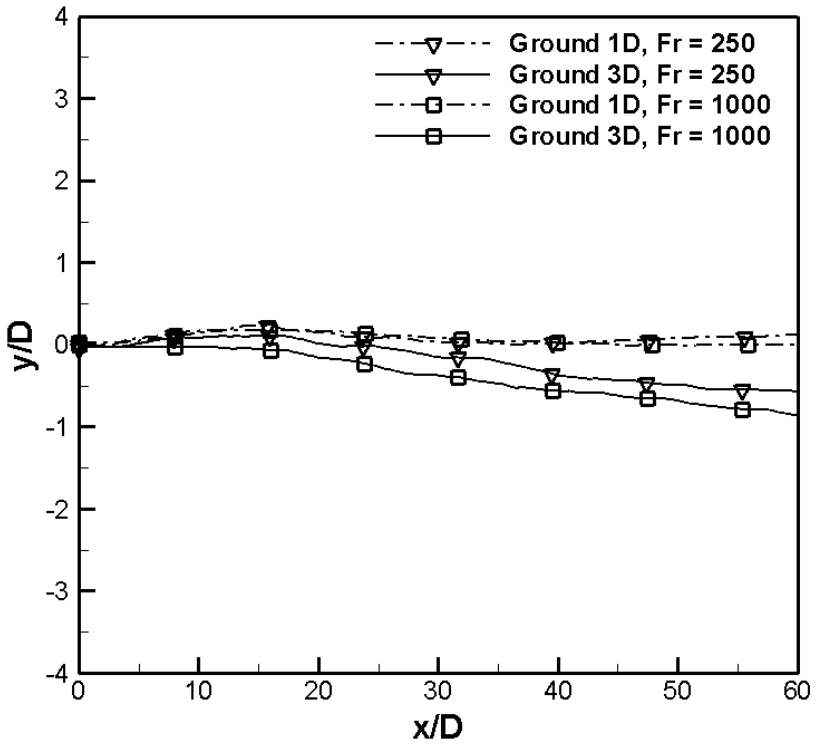

Figure 3.39 – Jet centerline representation for ground boundary normalized by *D*.

Potential core areas for *Fr* = 250 and 1000 were observed to extent 3*D* and 6*D* downstream of the nozzle exit. It has been reported that the potential core region of free jets are shorter comparing to those of pure wall jets (Dongdong and Adrian 2010). Jet centerlines for free jet cases are presented in Figure 3.4. As mentioned before, for the free jet cases the jet centerline experienced no deviation from nozzle axis for *Fr* = 1000, however, for *Fr* = 250 at *x/D* = 60, an approximate 0.5*D* deviation was observed.

For the cases located at 1*D* distance from the ground surface, a small negative concavity was seen in jet centerlines at the jet near-field region. This negative concavity was more pronounced in *Fr* = 1000. Jet to surface attachment was observed

for both cases. The attachment of the jet flow to the surface of the ground prevented the lower boundary of the jet from expansion and ambient mixing in that direction. This resulted in the acceleration of the jet's upper boundary to fulfill the mass flow rate. The acceleration of the jet flow in upper side of the jet shifted the points of maximum velocity away from the surface. Farther downstream, as the velocity gradient diffused the jet centerline was shifted towards the surface due to the presence of surface forces. Downstream of the jet to surface attachment point, as the boundary layer between the jet and the ground surface developed, the jet centerline deflected away from the surface. The boundary layer developed between the jet and the surface downstream of the attachment point is addresses as the surface boundary layer throughout the text. As the surface boundary layer thickened, it retarded the lower layer of the jet which shifted the points of maximum velocity and the jet centerline away from the ground surface. This shift was more pronounced in Fr = 250 cases at 1D distance from the ground surface in comparison with Fr = 1000 at the same distance from the surface. This could be because of lower initial Reynolds number and also stronger buoyancy forces for this case.

For the cases located at 3D distance from the ground surface, jet centerlines were forced towards the ground surface due to surface forces. The ground surface retarded the lower boundary of the jet downstream of the attachment point, which drawn the overall jet structure towards the ground surface due to the resultant pressure gradient across the jet. For Fr = 1000, the ground boundary forced the jet centerline to deviate from the nozzle axis for x/D > 10. However, the first effects of centerline deviation for Fr = 250 were seen at x/D = 20. This might be because of the presence of buoyancy

forces which forced the centerline to move in the opposite direction. On the other hand as mentioned before, lower the Froude number would lead to lower surface forces in flows near a surface. For Fr = 1000 the jet centerline deflected about 1D at x/D = 70 whereas 0.6D deflection was observed at same location for Fr = 250.

3.4.1.2 Ceiling

Jet centerlines for dispersion cases in the vicinity of ceiling boundary are presented in Figure 3.40.

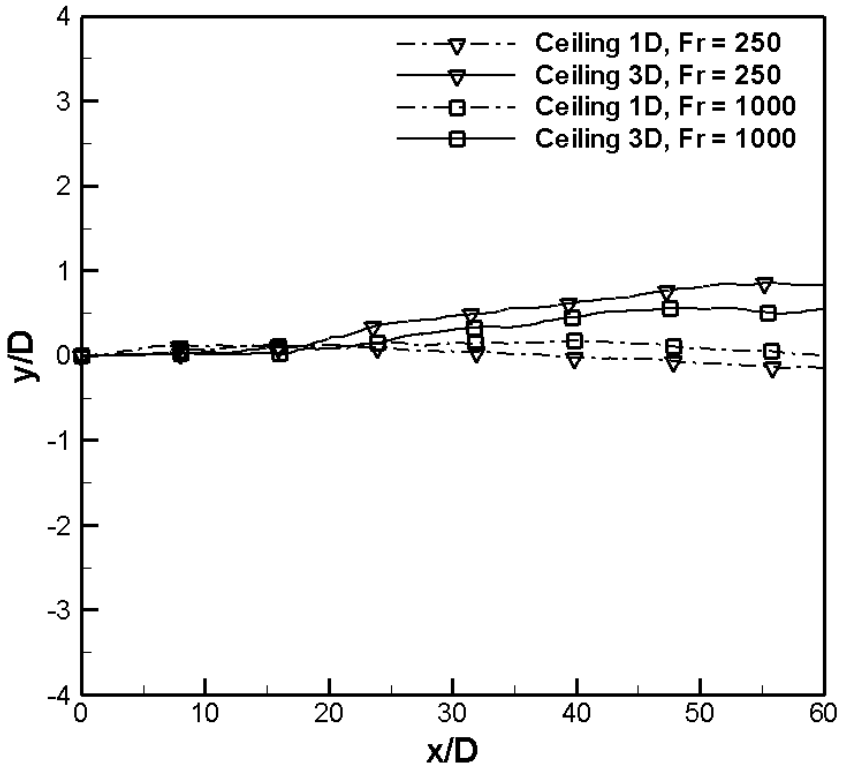

Figure 3.40 – Jet centerline representation for ceiling boundary normalized by D.

The main difference between the jet flows near the ceiling with those near the ground surface was the direction of surface forces. In these cases jet buoyancy forces acted in the same direction as the surface forces. Jet centerline deflections towards the ceiling surface were observed in these cases. For the cases located at 1D distance from

the ceiling surface, jet centerlines were observed to move towards the ceiling surface approximately downstream of the potential core region. Downstream of the jet to surface attachment point, the jet centerlines were shifted away from the ceiling surface as the boundary layer between the jet and the ceiling surface was developed. Similar to jet flows near the ground surface, as the surface boundary layer thickened, the retarded flow in the boundary layer forced the points of maximum velocity and the jet centerline away from the surface. This centerline deflection was found to be more pronounced for lower Froude numbers because of lower initial Reynolds number which led to a thicker boundary layer downstream of the attachment point. This centerline deflection for the cases located at 1*D* distance from the surface, led to a negative overall concavity in flow centerline plots.

For cases located at 3*D* distance from the ceiling, jet centerlines deflected towards the ceiling at approximately $x/D > 17$ and $x/D > 20$ for $Fr = 250$ and 1000 respectively. Overall deviation of 0.9*D* and 0.6*D* from the nozzle axis were observed at $x/D = 70$ for $Fr = 250$ and 1000 respectively. More centerline deviation was observed for $Fr = 250$ due to the presence of stronger buoyancy forces which forces the jet structure towards the surface.

3.4.1.3 Vertical Wall

Figure 3.41 shows the jet centerlines for the cases near the vertical wall surface. In these cases surface forces acted towards the negative *z*-direction while the buoyancy forces acted normal to that, in positive *y*-direction.

For jet flows near the ground and ceiling surface, buoyancy and surface forces acted in the same plane but for the jets near the vertical wall surface, these forces acted in two different planes normal to each other which led to no interaction between buoyancy and surface forces in these cases.

Greater centerline deflections were observed in cases located at 1*D* distance from the surface comparing to other surface orientations. The wall surface retarded the jet flow in the *z*-direction while buoyancy forces moved the jet centerline towards positive *y*-direction. The jet centerline deviations towards the *+y* direction were observed for $x/D > 8$ and $x/D > 40$ for $Fr = 250$ and 1000 respectively. Overall centerline deflection of $y/D = 1.8$ and 0.5 were observed for Fr = 250 and 1000 correspondingly.

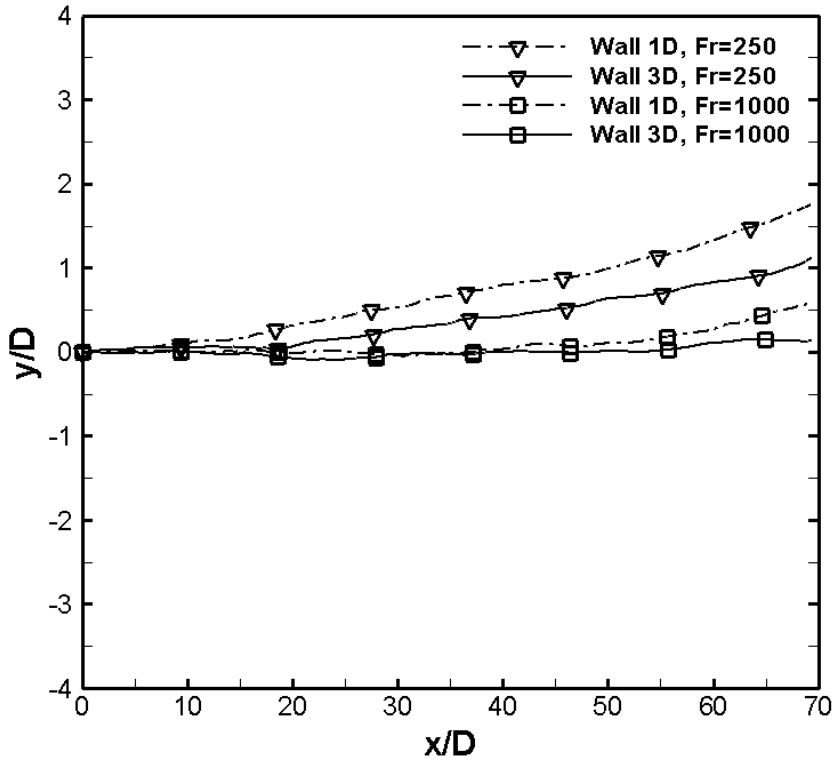

Figure 3.41 – Jet centerline representation for vertical wall boundary normalized by *D*.

For cases located at 3*D* distance from the wall, the resultant surface forces would be less comparing to the cases closer to the wall due to less resultant pressure gradient across the jet. These lower surface forces can be related to slower velocity decay rates. Slower velocity decay rates delayed the transition from momentum to buoyancy dominated regions in the jet flow which resulted in smaller centerline deflection due to buoyancy forces. In these cases jet centerlines were observed to follow the nozzle axis for almost 20*D* and 58*D* for Fr = 250 and 1000 respectively with minimal deviation towards the positive y-direction. Overall centerline deflection of y/D = 1.1 and 0.1 were observed for Fr = 250 and 1000 respectively.

3.4.2 Time-averaged Velocity Field

Time-averaged velocity fields of the jet flows near boundary surfaces are presented in this section. For all the cases presented herein, velocity profiles were averaged over 350 PIV images.

3.4.2.1 Ground

Time-averaged velocity fields for jets at vicinity of ground boundary are shown in Figure 3.42.

For the cases located at 3*D* distance away from the ground surface, the overall jet deflection towards the surface due to the presence of surface forces were more evident. The overall extent of the jet structure were observed to be slightly shorter than those of free jet flows due to interactions of the jet boundary and the ground surface which retarded the jet flow at the jet far-field regions. The jet extent of approximately 30*D* and 20*D* were observed for Fr = 1000 and 250 respectively. The jet extent in free jet

cases was measured to be approximately 32*D* and 22*D* accordingly. Slightly longer potential core areas were also observed in jet flows near a surface comparing to free jet flows. This was due to the limited ambient entrainment which led to slower velocity decay rates. Longer potential core region for jet flows near a ground surface is also reported by (Dongdong and Adrian 2010). The potential core areas for *Fr* = 1000 and 250 located at 3*D* distance from the surface were extended 6*D* and 3*D* versus 5*D* and 2*D* for those in free jet flows.

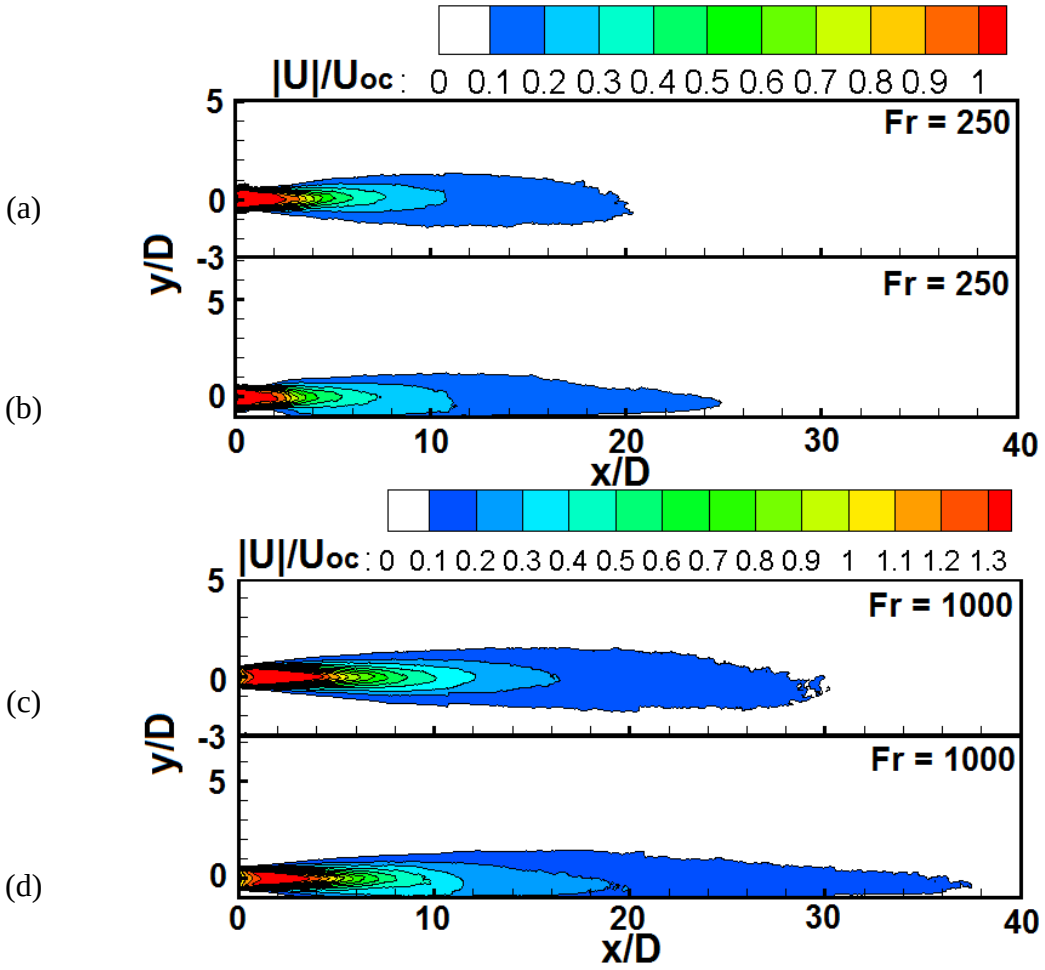

Figure 3.42 – Time-averaged velocity fields (a) Fr = 250 at 3*D*, (b) Fr = 250 at 1*D*, (c) Fr = 1000 at 3*D* and (d) Fr = 1000 at 1*D* distance from the ground surface.

In cases located at 1*D* distance from the ground surface, the overall jet structure travelled farther downstream comparing to those located at 3*D* distance from the surface and also to those of free jet flows. Slower velocity decay rates were observed in these cases due to lower ambient entrainments at the jet's lower boundary which led to longer jet extent. Time-averaged velocity fields extended 37*D* and 25*D* for *Fr* = 1000 and 250 respectively. However, the potential core areas were slightly shorter comparing to jets located at 3*D* from the surface. The potential core extents in these cases were measured to be approximately 5*D* and 2*D* for *Fr* = 1000 and 250, which are comparable to those of free jet flows. The reason for shorter potential core areas in cases closer to the surface may be explained by the position of attachment points. Faster jet to surface attachment in cases located at *1D* distance from the ground surface comparing to cases located at *3D* distance, may greatly slow down the jet's lower boundary which can be related to slightly shorter potential core regions.

In order to calculate the jet to surface attachment point, the jet width development equation of (Kanury 1977) for circular free jets may be used as following:

$$\frac{2\delta_j}{D} = 1 + 24C\frac{x}{D}, \tag{3.7}$$

where δ_j is the jet radius, D is nozzle diameter, x is downstream distance and C is an empirical constant equal to 0.0128.

This relation was used to calculate the approximate downstream distance at which the jet width growth was equal to the nozzle to surface distance. In the other words the downstream distance at with the jet is wide enough to attach to the surface. The jet radius (δ_j) was set to 1*D* and 3*D* which represented the jet to surface distances. The

approximate jet to surface attachment points were calculated to be located at x = 6.5D and 16D downstream of the nozzle exit for nozzle to surface distances of 1D and 3D respectively. The experimental jet attachment distances are shown in Table 3-1. These distances were calculated with respect to the nozzle exit. Theoretical values were found to be closer to experimental values for Fr =1000.

Table 3-1. Jet to surface attachment point measured from nozzle tip for Ground boundary

Froude number	**Jet to surface distance**	**Attachment point, *x***
250	1D	2.5D
250	3D	10D
1000	1D	4D
1000	3D	15D

3.4.2.2 Ceiling

Figure 3.43 represents time-averaged velocity plots for jet flows near the ceiling surface. Downstream jet extents for the cases located at 3D distance from the ceiling surface were observed to be similar to those of jet flows near the ground surface. However, at the jet far-field regions, more evident jet deflections were seen in jet flows near the ceiling surface comparing to jets near the ground surface. This can be related to the presence of strong buoyancy forces in those locations.

The extents of potential core areas were found to be similar to those of jet flows near the ground surface. The flow in potential core region is solely momentum dominated and effects of buoyancy are negligible. For the cases located at 1D distance from the ceiling surface, jet extents of approximately 37D and 25D were observed similar to those of jets near the ground cases.

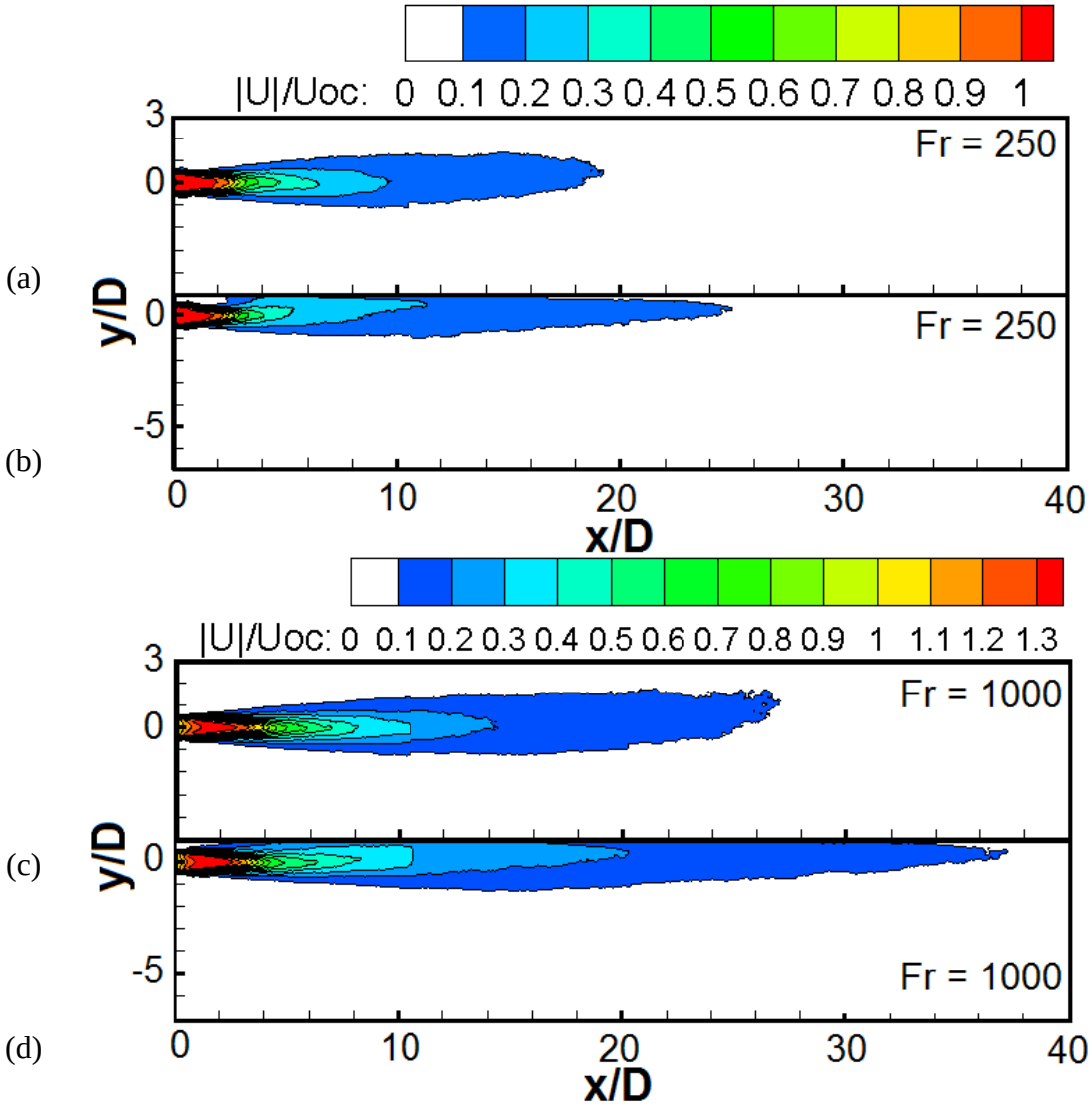

Figure 3.43 – Time-averaged velocity fields (a) Fr = 250 at 3*D*, (b) Fr = 250 at 1*D*, (c) Fr = 1000 at 3*D* and (d) Fr = 1000 at 1*D* distance from the ceiling surface.

The experimental jet to surface attachment points for jet flows near the ceiling surface are shown in Table 3-2. Shorter jet to surface attachment distances were observed in jets near the ceiling surface comparing to flows near the ground surface. As mentioned before, in jet flows near the ceiling surface, buoyancy and surface forces acted in the same direction. The presence of buoyancy forces in $+y$ direction amplified the surface forces which deflected the jet structure towards the ceiling surface and led to shorter jet attachment distances.

Table 3-2. Jet to surface attachment point measured from nozzle tip for ceiling boundary cases

Froude number	Jet to surface distance	Attachment point, *x*
250	1D	2.1D
250	3D	10.5D
1000	1D	2.5D
1000	3D	12.5D

3.4.2.3 Vertical Wall

Time-averaged velocity fields for Fr = 250 and 1000 near the vertical wall surface are presented in Figure 3.44. As mentioned before, in these cases buoyancy forces and surface forces acted in two different planes normal to each other. For jet flows near the ground surface, buoyancy and the surface forces acted in the same plane but in opposite direction. This led to the suppression of buoyancy forces by surface forces and the effect of buoyancy forces were found to be weakened by those forces. On the other hand for jet flows near the ceiling surface, effects of buoyancy forces were observed to be more pronounced which led to smaller jet to surface attachment distances. However, after the attachment point the effects of these forces were observed to be suppressed by the ceiling which prevented the jet from traveling in the direction of buoyancy forces.

For the cases of jets in the vicinity of vertical wall surface, buoyancy and surface forces act in two different planes normal to each other with limited or no interaction. The potential core extent and overall jet structure in jet near-field area were observed to be similar to those of jet flows near ground and ceiling surfaces. The longer potential core region was seen in these cases comparing to free jet flows.

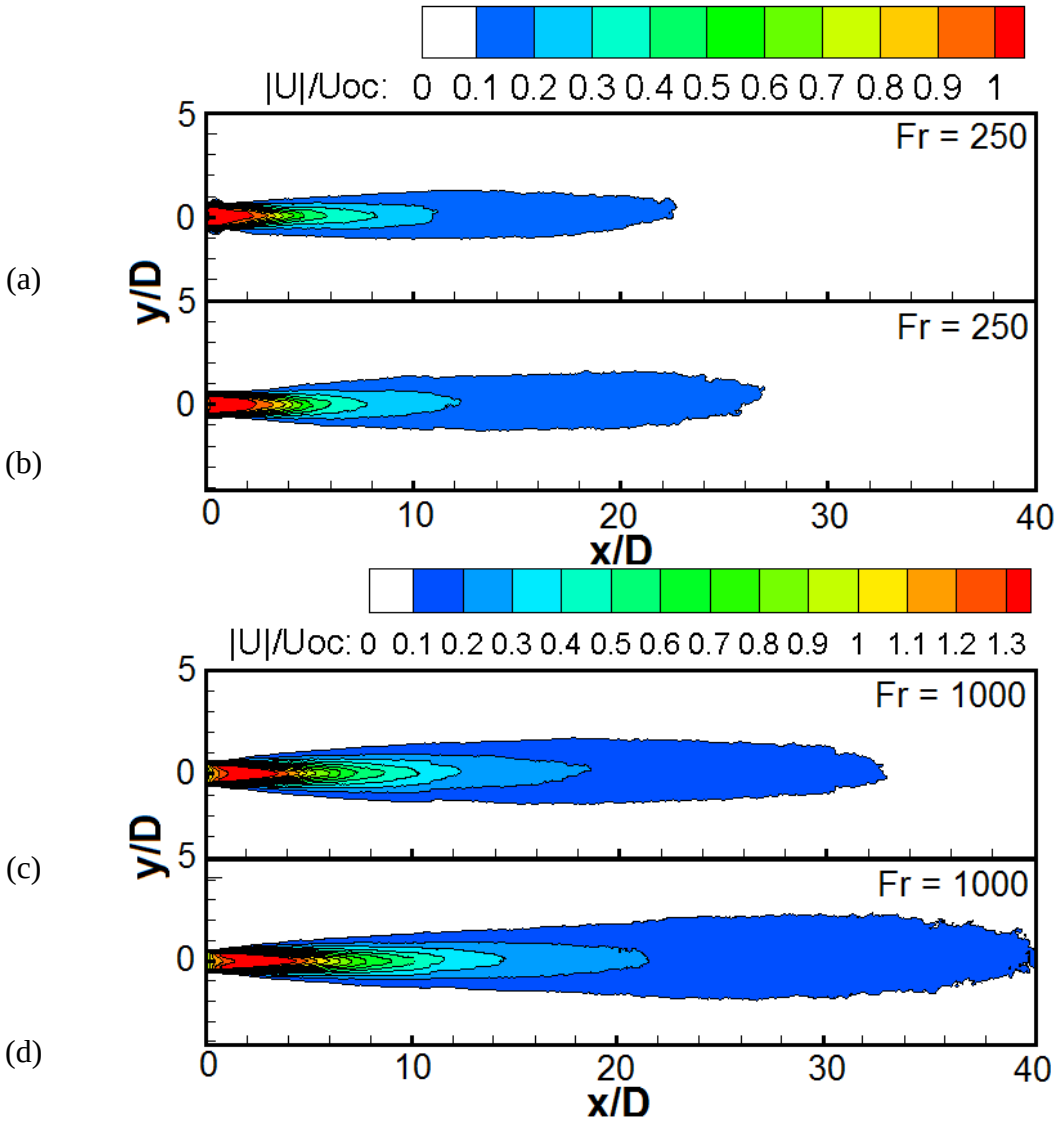

Figure 3.44 – Time-averaged velocity fields (a) Fr = 250 at 3*D*, (b) Fr = 250 at 1*D*, (c) Fr = 1000 at 3*D* and (d) Fr = 1000 at 1*D* distance from the vertical wall.

At the jet far-field location where effects of buoyancy forces were more pronounced, jet structure deflected towards the +*y*-direction. The overall jet extent in these cases were found to be longer comparing to jet flows near ground and ceiling surfaces. For cases located at 3*D* distance from the wall surface, downstream jet extents of 23*D* and 33*D* were observed *Fr* = 250 and 1000 respectively. While the downstream

jet extent of approximately 27*D* and 40*D* were measured for flows located at 1*D* accordingly.

3.4.3 Velocity Decays

Velocity decay rates along the jet centerline for the jet dispersion cases near a wall surface are presented in this section. Velocity decay rates are plotted along the jet centerline coordinate system, *s*. Log-log plots are used in order to capture the centerline velocity variation in a linear manner. The jet centerline velocity was normalized by time-averaged nozzle exit velocity, U_{oc}, and jet centerline coordinate, *s*, was normalized by jet diameter, *D*.

3.4.3.1 Ground

Jet centerline decay rates for jet flows near the ground surface are shown in Figure 3.45. The lines of $s^{-1.1}$, $s^{-0.9}$ and $s^{-0.7}$ are shown in the figure for comparison. It should be noted that for free jet flows, the decay rates of $s^{-1.1}$ and $s^{-0.9}$ in jet near- and far-field regions were observed respectively for the sharp-edged orifice inflow configuration which are presented in section 3.2.3. Velocity decay rates of $s^{-0.5}$ and $s^{-0.6}$ are reported in literature for pure wall-jets with contoured inflow condition (Volker and Johnston 1993).

For *Fr* = 250 located at 1*D* distance from the ground surface, velocity decay rate of $s^{-1.1}$ was observed in the potential core region. However, for *Fr* = 1000, a slightly faster decay rate of $s^{-1.2}$ was seen. Farther downstream, these velocity decay rates were dropped due to the development of the wall-jet flow structure. Decay rates of $s^{-0.9}$ and $s^{-0.8}$ were observed in downstream of potential core region for *Fr* = 250 and 1000

respectively. These decay rates persisted for almost 50*D* at the jet far-field regions. However, farther downstream faster decay rates were observed as the wall boundary layer developed and retarded the flow. In jet far-field regions, the velocity decay rate of $s^{-1.0}$ was measured for *Fr* = 1000, However, for *Fr* = 250 this decay rate was slower (i.e. $s^{-0.9}$) due to presence of strong buoyancy driven acceleration components.

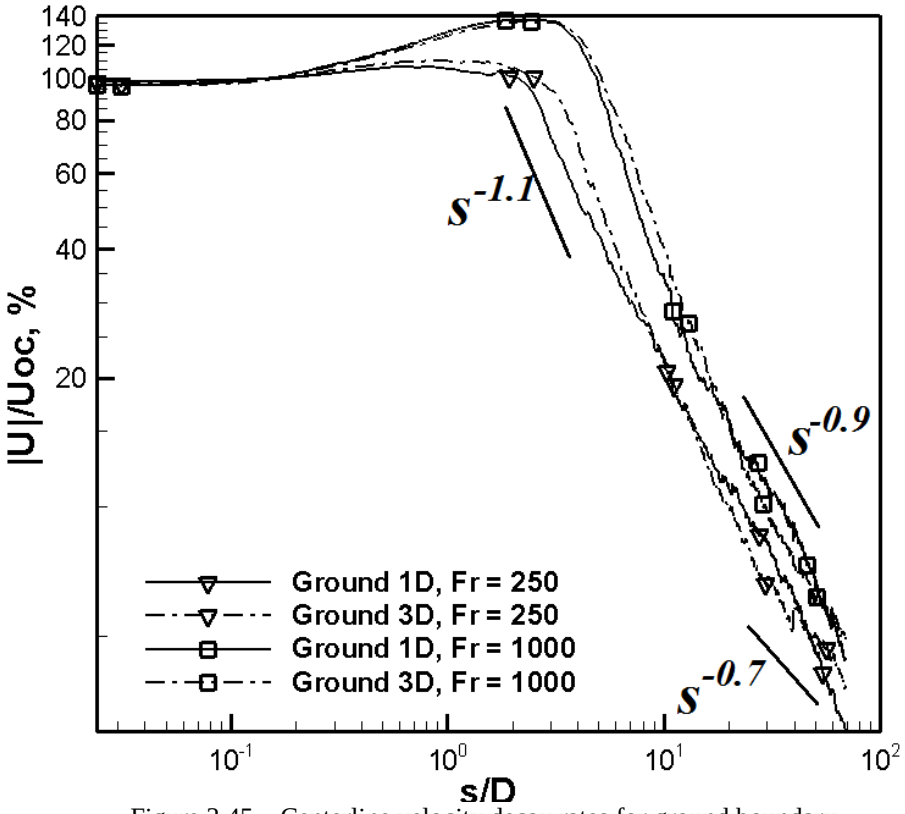

Figure 3.45 – Centerline velocity decay rates for ground boundary.

In jets located at 3*D* distance from the surface, same velocity decay rates of approximately $s^{-1.1}$ and $s^{-1.2}$ were observed in the jet potential core regions for *Fr* = 250 and 1000 respectively. These decay rates dropped to $s^{-0.8}$ downstream of the jet to surface attachment point due to development of wall-jet structure. As mentioned before, for jet flows near the ground surface, buoyancy forces acted in the opposite direction to surface forces. This reduced the surface effects in regions were buoyancy forces were

more pronounced. These velocity decay rate were further dropped to $s^{-0.7}$ at the jet far-field region ($s/D > 55$) as the buoyancy effects became more dominant. Slower velocity decay rate was observed at the jet far-field regions for $Fr = 250$ as a result of more pronounced buoyancy forces.

The velocity decay rates at downstream of the potential core region for jet flows located at 1D distance from the ground surface, were observed to be slightly slower comparing to the cases located at 3D distance from the surface. Smaller nozzle to surface distances led to the shorter jet to surface attachment distances which resulted in a more developed wall-jet structure with slower velocity decay rates. This slower decay rates persisted at the jet far-field regions.

3.4.3.2 Ceiling

Figure 3.46 presents the centerline decay rates for $Fr = 1000$ and 250 near the ceiling boundary. The lines of $s^{-1.1}$ and $s^{-0.7}$ are also included in the figure. Similar velocity decay rates to those of jet flows near the ground surface were observed in potential core regions. Centerline velocity decay rate of $s^{-1.1}$ and $s^{-1.2}$ were observed in potential core areas for $Fr = 250$ and 1000 respectively. These velocity decay rates gradually dropped downstream of the jet to surface attachment point as a result of development of wall-jet structure.

As mentioned before, the buoyancy and surface forces in jet flows near the ceiling surface acted in same direction. So more pronounced wall-jet structure was expected at the jet far-field regions of these cases comparing to jet flows near ground and vertical wall surfaces.

For the jet flows located at 1*D* distance from the ceiling surface, velocity decay rates of $s^{-0.7}$ and $s^{-0.8}$ were observed for *Fr* = 250 and 1000 respectively at downstream of the potential core region. These decay rates persisted for almost 50*D* in downstream direction. Farther downstream, development of wall boundary layer near the ceiling surface retarded the adjacent jet flow which led to faster decay rates at the jet far-field regions. Velocity decay rate of $s^{-1.0}$ was observed at *s/D* > 50 for both *Fr* = 1000 and 250. These rates were slightly faster comparing to those of jet flows near the ground surface especially for *Fr* = 250 as the effects of buoyancy forces were suppressed by the presence of the ceiling surface.

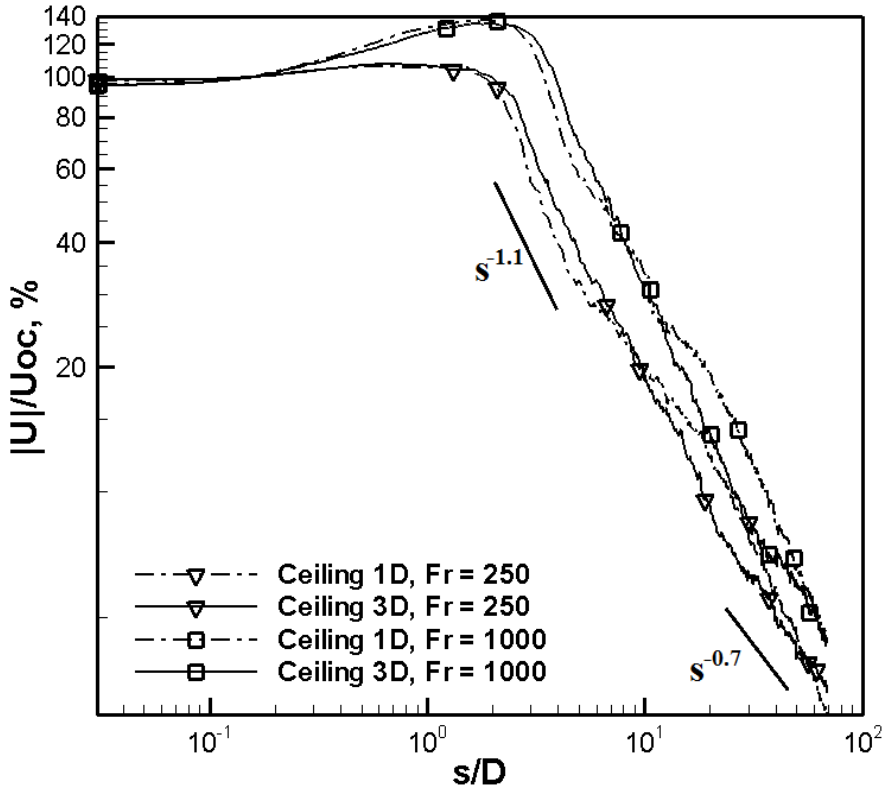

Figure 3.46 – Centerline velocity decay rates for ceiling boundary.

For the jet flows located at 3*D* distance from the ceiling surface, following observations were made. Downstream of the potential core region the jet centerline

velocity decayed at a faster rate comparing to the flows closer to the surface. These decay rates were observed to be similar to those of free jet flows. Greater nozzle to surface distance led to a longer jet to surface attachment distance which delayed the development of wall-jet structure and faster velocity decay rates. Downstream of the attachment point, the jet centerline velocity decay rates were dropped to $s^{-0.7}$ as the wall-jet structure was further developed.

3.4.3.3 Vertical Wall

Centerline velocity decay rate plots for jet flows near the vertical wall surface for *Fr* = 1000 and 250 are shown in Figure 3.47. The lines of $s^{-1.1}$, $s^{-0.9}$ and $s^{-0.7}$ are also presented in the figure for comparison.

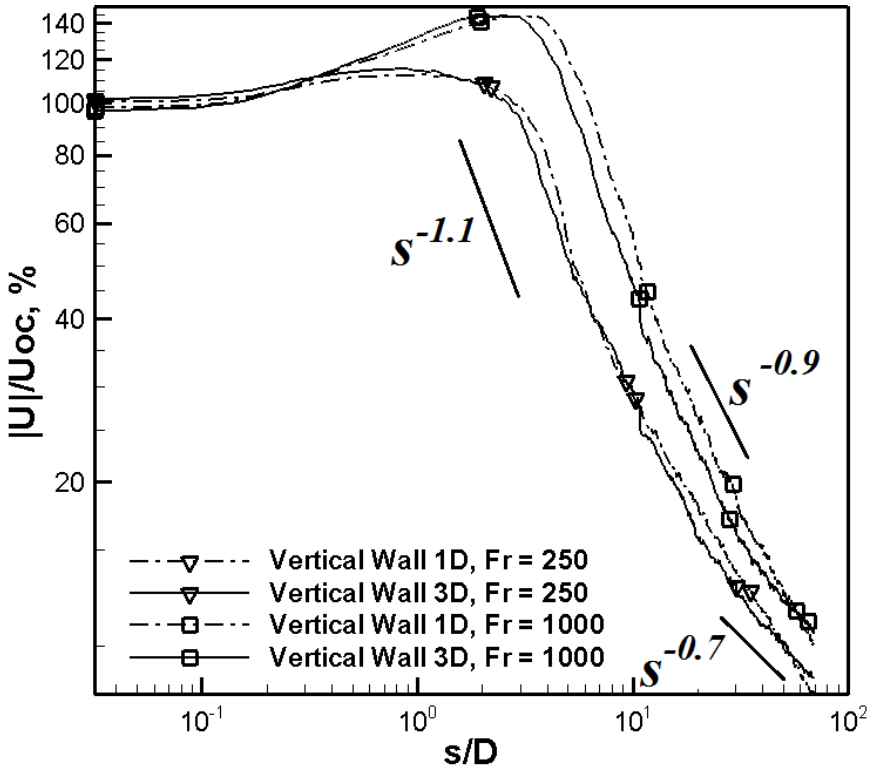

Figure 3.47 – Centerline velocity decay rates for vertical wall boundary.

Velocity decay rates of $s^{-1.1}$ and $s^{-1.2}$ were observed for Fr = 250 and 1000 respectively at potential core areas. Similar observation were also made in flows near ground and ceiling surfaces which led to the conclusion that the jet centerline velocity decay rates in potential core region, were not related to the surface orientation.

Downstream of the potential core region (i.e. at $s/D > 5$ for Fr = 250 and $s/D > 11$ for Fr = 1000), these decay rates were dropped to approximately $s^{-0.9}$ due to development of the wall-jet structure. For the jet flows located at 1D distance from the wall surface, these decay rates persisted to $s = 50D$ in downstream direction. At the far-field locations centerline velocity profiles decayed slightly faster due to thickening of the wall boundary layer which retarded the flow. However, for the flows located at 3D distance from the wall surface, slower decay rate of approximately $s^{-0.7}$ was observed in the jet far-field region due to the presence of buoyancy driven acceleration forces.

3.4.4 Velocity Profiles

Normalized velocity profiles are usually used to shown jet spread in downstream locations. This section presents the normalized velocity profiles for jet flows near boundary surfaces with different orientations. Radial velocity profiles are shown against jet's n-coordinate system normal to jet centerline, s. Radial velocity profiles are normalized by the time-averaged centerline velocity at each downstream location and the n-axis is normalized by L_u parameter. L_u is the point at which radial velocity magnitude is equal to the half of the centerline velocity.

3.4.4.1 Ground

Radial velocity profiles at different downstream locations along the jet centerline for flows near the ground surface are presented in Figure 3.48.

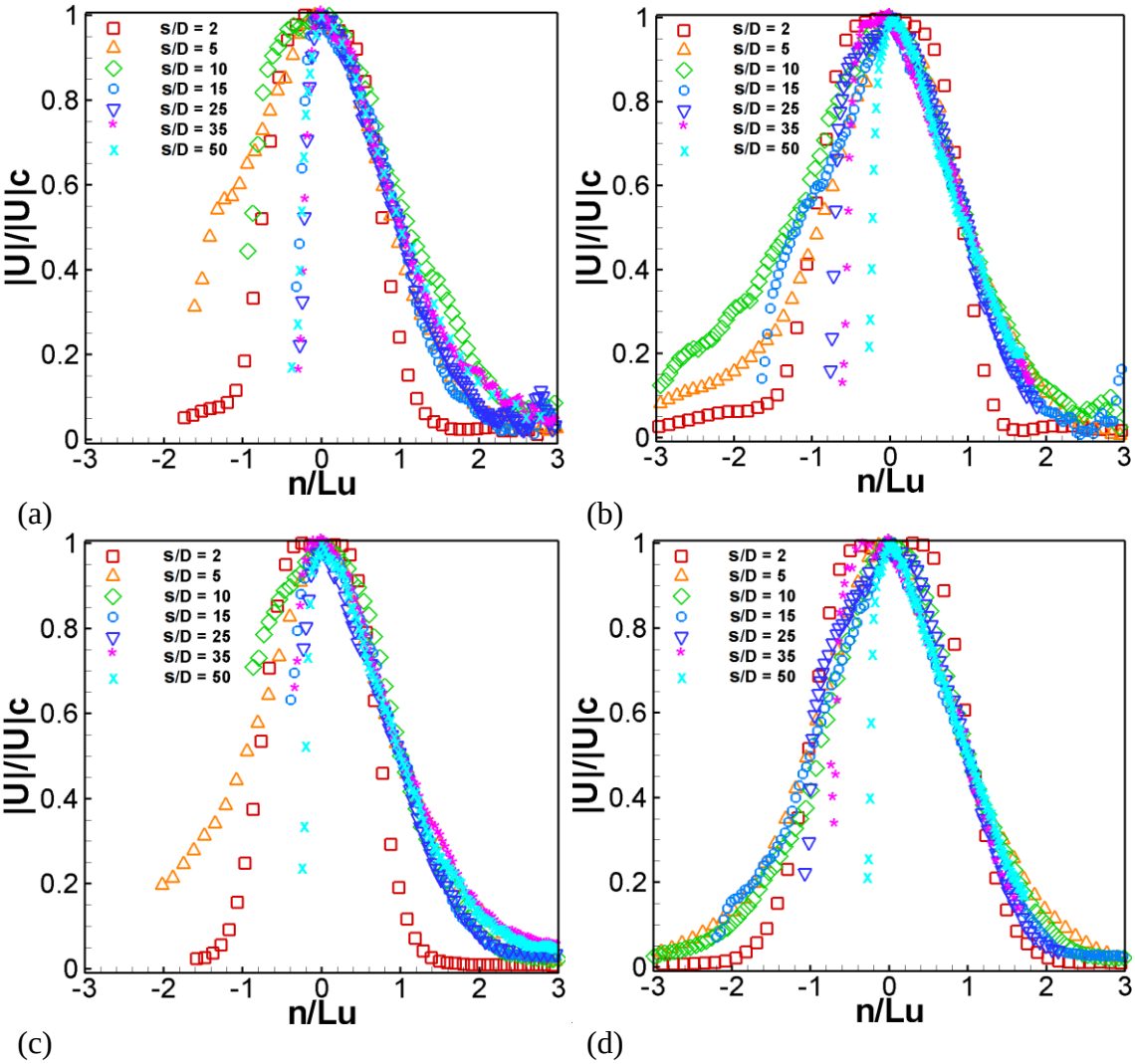

Figure 3.48 – Radial profiles of the time-averaged velocity, jet near ground surface, Fr = 250 located at (a) 1D, (b) 3D and Fr = 1000 located at (c) 1D and (d) 3D from the ground surface.

For the jet flows located at 1*D* distance from the ground surface, jet velocity profiles showed a Gaussian distribution at *s/D* = 2. Farther downstream, first effects of the jet to surface attachment were seen at *s/D* = 5 where radial distribution deformed into an asymmetric profile in the negative *n*-direction. Downstream of the jet to surface

attachment point, the jet structure presented the characteristics of a two layered structure consisting of a lower layer adjacent to the ground surface and a top layer. For Fr = 250, development of the wall-jet structure was evident for s/D > 15 as the radial velocity distribution showed a semi-Gaussian profile in +n direction and was restricted near the ground surface in -n direction. For Fr = 1000, a similar behaviour was observed.

Following observation were made for jet flows located at 3D distance from the ground surface. A symmetric Gaussian distribution was observed at s/D = 2 for both Froude numbers. For Fr = 250, first effects of surface forces were seen at s/D = 5, were velocity profiles were deformed in -n direction. Jet to surface attachment was evident in s/D = 15 profiles as the ground boundary layer retarded the jet flow in the –n-direction. Farther downstream, velocity distributions showed a two peaked profile with one peak near the jet centerline and a weaker peak near the ground surface. As the ground boundary layer developed downstream of the jet to surface attachment point, the ground surface limited the jet expansion in the lower surface of the jet. This led to the acceleration of the upper jet boundary to balance the mass flow rate which resulted a two layered structure with a two velocity peaks. At the jet far-field locations, these two peaks in velocity profiles joint together in a fully developed wall-jet structure.

Same behaviour was observed in cases with Fr = 1000. However, the first effects of ground boundary layer were seen at s/D = 25 and a two peaked velocity distribution was observed at s/D = 35. A fully developed wall-jet structure was observed at s/D = 50 at which the ground boundary layer retarded the lower boundary of the jet.

In order to have a better understanding of downstream evolution of jet flows near the ground surface, normalized velocity profiles at different downstream locations are shown in Figure 3.49.

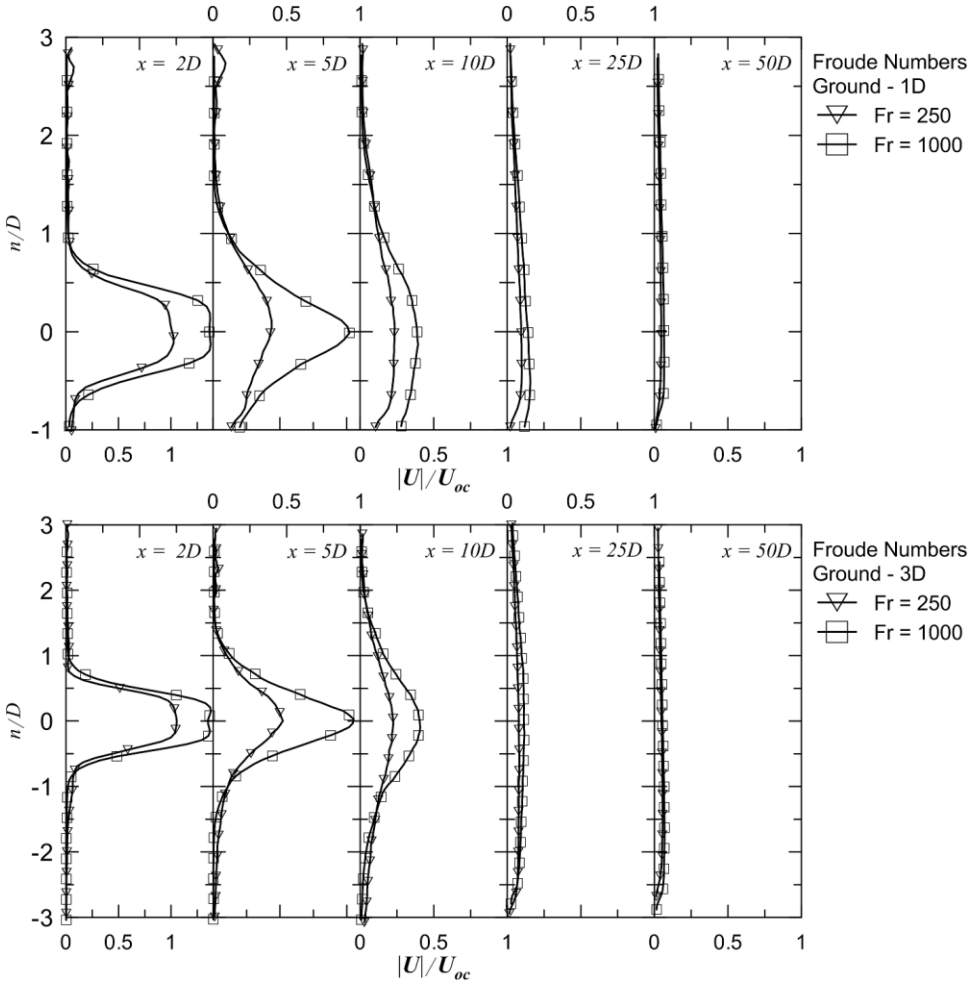

Figure 3.49 – Normalized velocity profiles for jets near the ground surface with nozzle to surface distance of 1D (top) and 3D (bottom).

In all cases, the magnitude of the peak velocity decreased with the increase in downstream distance. The effects of surface forces were more pronounced for Fr = 250 comparing to Fr = 1000. Downstream of the jet to surface attachment point, the velocity profiles were observed to be asymmetric as the jet entrainment was restricted by the ground surface.

The development of a two peaked structure is evident for Fr = 250 located at 1D distance from the ground surface at s/D = 5, which was also observed in the radial velocity profile. At the jet far-field locations these two peaks joint together to form a single peak near the jet centerline close to the ground surface.

For jet flows located at 3D distance from the ground surface, the effects of the ground boundary were less pronounced on the overall flow structure upstream of the jet attachment point. However, at the far-field locations, overall jet structure was deflected closer to the surface which led the development of the wall-jet structure at s/D = 50. At this location, jet centerline for Fr =250 was observed to be located farther away from the ground surface comparing to Fr =1000 due to the presence of stronger buoyancy forces in this case.

3.4.4.2 Ceiling

Radial velocity distributions at different downstream locations for jet flows near the ceiling surface are shown in Figure 3.50. Velocity profiles were normalized by centerline time-averaged velocity at each downstream location and were plotted against jet coordinate system, n, normalized by L_u.

For cases with nozzle to ceiling distance of 1D, a Gaussian distribution were seen at the jet near-field region (i.e. s/D = 2). For Fr = 250, first effects of jet to surface interaction were observed at s/D = 5, where the velocity distribution was deformed into a two peaked velocity profile. Similar to jet flows near the ground surface, a two layer wall-jet structure was observed. The wall-jet structure consisted of a layer near the ceiling surface with lower flow velocity (associated with the weaker peak) and a faster

moving flow near the jet centerline at the lower boundary of the jet. These two peaks joint together at farther downstream which led the development of a fully developed wall-jet structure at $s/D > 5$.

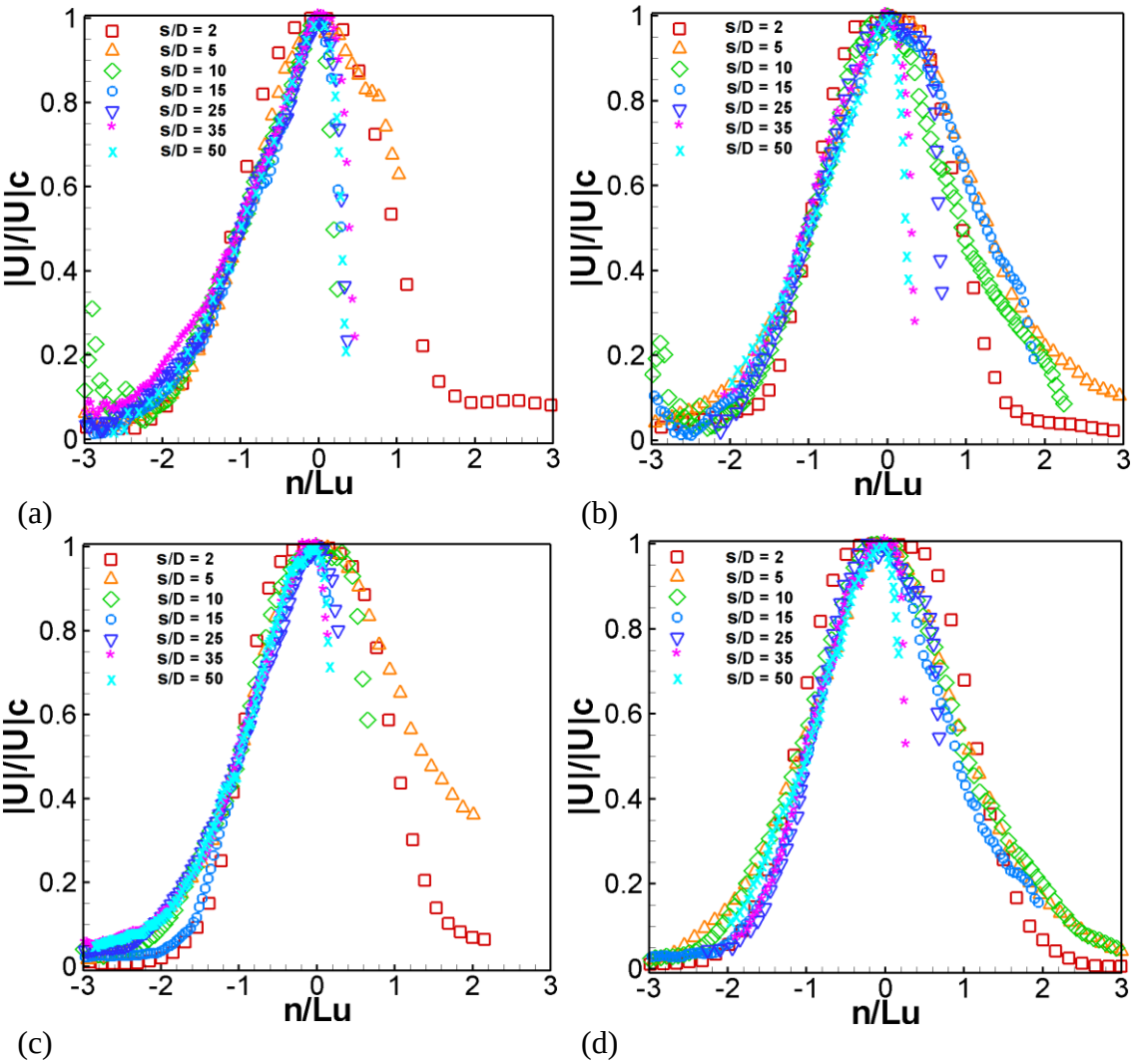

Figure 3.50 – Radial profiles of the time-averaged velocity, jet near ceiling surface, Fr = 250 located at (a) 1D, (b) 3D and Fr = 1000 located at (c) 1D and (d) 3D from the ceiling surface.

It should be noted that, the fully developed wall-jet structure was observed closer to the nozzle in jet flows near the ceiling comparing to those near the ground surface. For instance for $Fr = 250$, the fully developed wall-jet structure was observed at $s/D \geq 10$ (see Figure 3.50.a) versus $s/D \geq 15$ near the ground surface. This can be explained by

the direction of buoyancy and surface forces. In the jet flows near the ceiling surface, the buoyancy forces act in the same direction as the surface forces which push the flow structure towards the ceiling surface. For Fr = 1000, first effects of jet to surface attachment were seen at s/D = 10 at which a two peaked velocity profile was observed. At farther downstream location, fully developed wall-jet structures were observed at $s/D > 10$.

For jet flows located at 3D distance from the ceiling surface, the fully developed wall-jet velocity profiles were observed at $s/D > 35$ for both Froude numbers. First effects of jet to surface attachment were seen at s/D = 15 and s/D = 25 for Fr = 250 and 1000 respectively.

Downstream evolution of jet velocity profiles for cases near the ceiling surface are shown in Figure 3.51. Radial velocity profiles were normalized by the time-averaged nozzle exit velocity, U_{oc}, and are plotted against the n-axis at different downstream locations. The peaks in velocity profiles were located near the jet centerline and were decreased in magnitude with increase in downstream locations.

For jet flows located at 1D distance from the ceiling surface, two picked velocity profiles were observed downstream of the jet to surface attachment point with one pick near the ceiling surface and another near the jet centerline. The distance between these two peaks on the velocity profiles were seen to be smaller comparing to those of jets near the ground surface at a same downstream location. These two peaks joint together and produced a single peaked profile at farther downstream locations.

At the same downstream locations, a more developed wall-jet structure was observed in jet flows near the ceiling comparing to that of ground surface. For instance

the velocity profile at *s/D* = 10 for *Fr* = 250 near the ceiling surface showed a single peak profile near the surface. However, the velocity profile at the same location near the ground surface was observed to have a two peaked profile with a stronger peak near the jet centerline and a weaker peak near the surface.

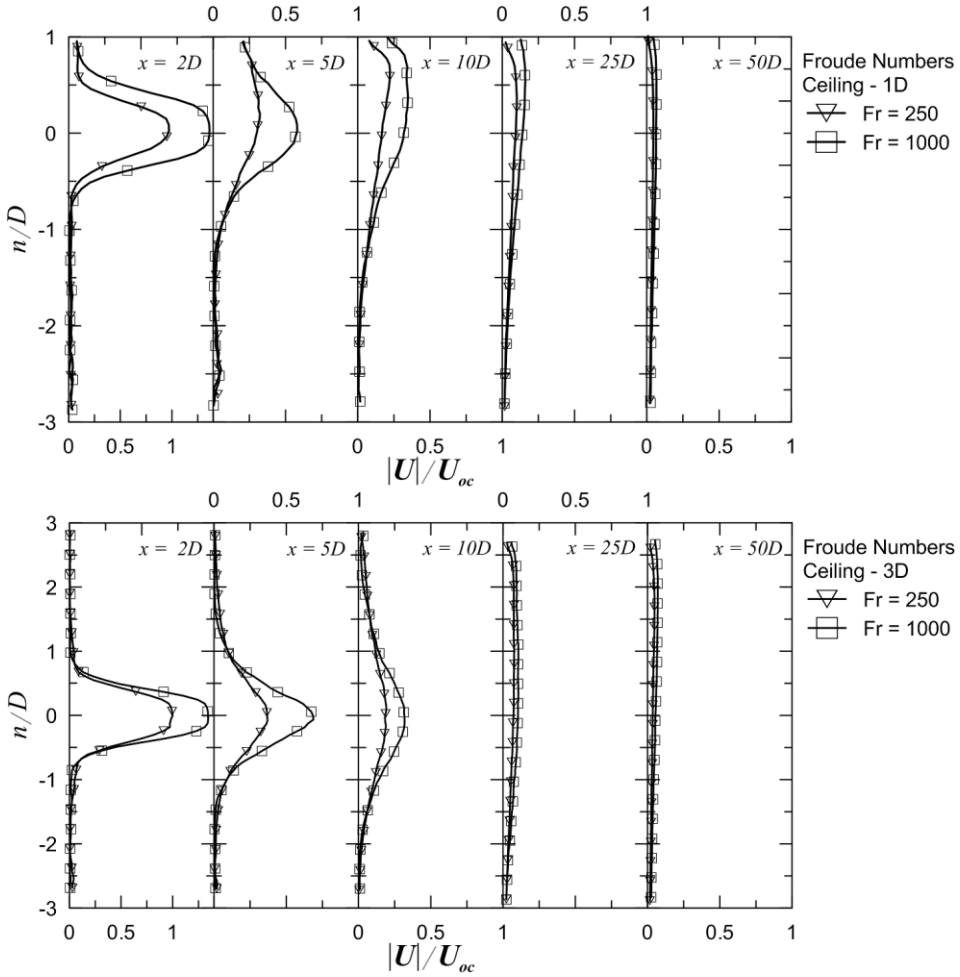

Figure 3.51 – Normalized velocity profiles for jets near the ceiling surface with nozzle to surface distance of 1D (top) and 3D (bottom).

The two peaked velocity profiles represent the development of surface boundary layer and transition of a free jet to a wall-jet structure under the influence of this boundary layer. On the other hand single peaked velocity profiles demonstrate the presence of fully developed wall-jet structure.

For the jet flows located at 3*D* distance from the ceiling surface, following observations were made. Shorter jet to surface attachment distances were observed comparing to flows near the ground surface. Fully developed wall-jet structures were seen in downstream regions at *s/D* > 25 and *s/D* > 35 for *Fr* = 250 and 1000 respectively.

3.4.4.3 Vertical Wall

Radial velocity profiles for the jets flows near the vertical wall are shown in Figure 3.52. The velocity profiles were normalized by the centerline time-averaged velocity magnitude at each downstream location and were plotted against the *n*-axis normalized by L_u. These velocity profiles for the jet flows near the vertical wall are particularly important as they illustrate the jet evolution in a plane parallel to the wall surface. This can be used to understand the jet spread for vertical wall boundary cases and also for other surface orientation.

In these cases the imaging plane was parallel to the vertical wall. Identification of the jet to surface attachment point would be impractical without considering the other physical properties such as velocity decay rates. Radial velocity profiles were observed to be symmetric with Gaussian distribution profiles.

For the jet flows located at 1*D* distance from the wall surface, the radial profiles resembled those of free jet flows at jet potential core region. At the far-field locations the decay rates observed to be slower comparing to free jet flows. However, for the cases with 3*D* from the wall surface these decay rates were observed to be more similar to those of free jet cases.

Increasing surface effects were seen in cases closer to the surface as the decay rates were observed to be slower in those cases.

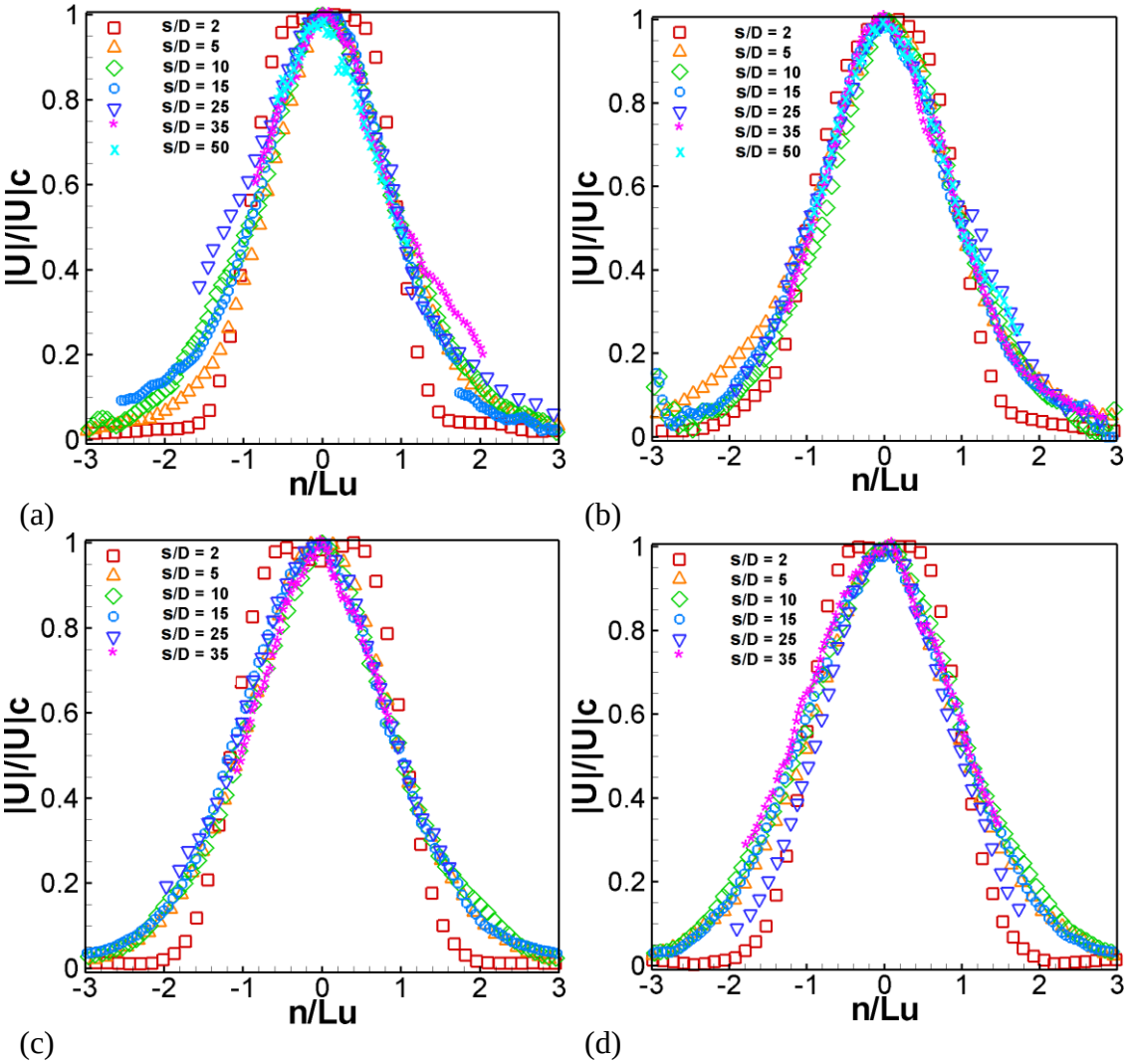

Figure 3.52 – Radial profiles of the time-averaged velocity, jet near vertical wall surface, Fr = 250 located at (a) 1D, (b) 3D and Fr = 1000 located at (c) 1D and (d) 3D from the vertical wall.

For the cases with $Fr = 250$, increasing effects of buoyancy forces at the jet far-field regions were observed as the radial velocity profiles in those regions appeared to be wider in the positive *n*-direction.

In order to better understand the downstream evolution of the jet structure, jet radial velocity profiles in different downstream locations are presented in Figure 3.53.

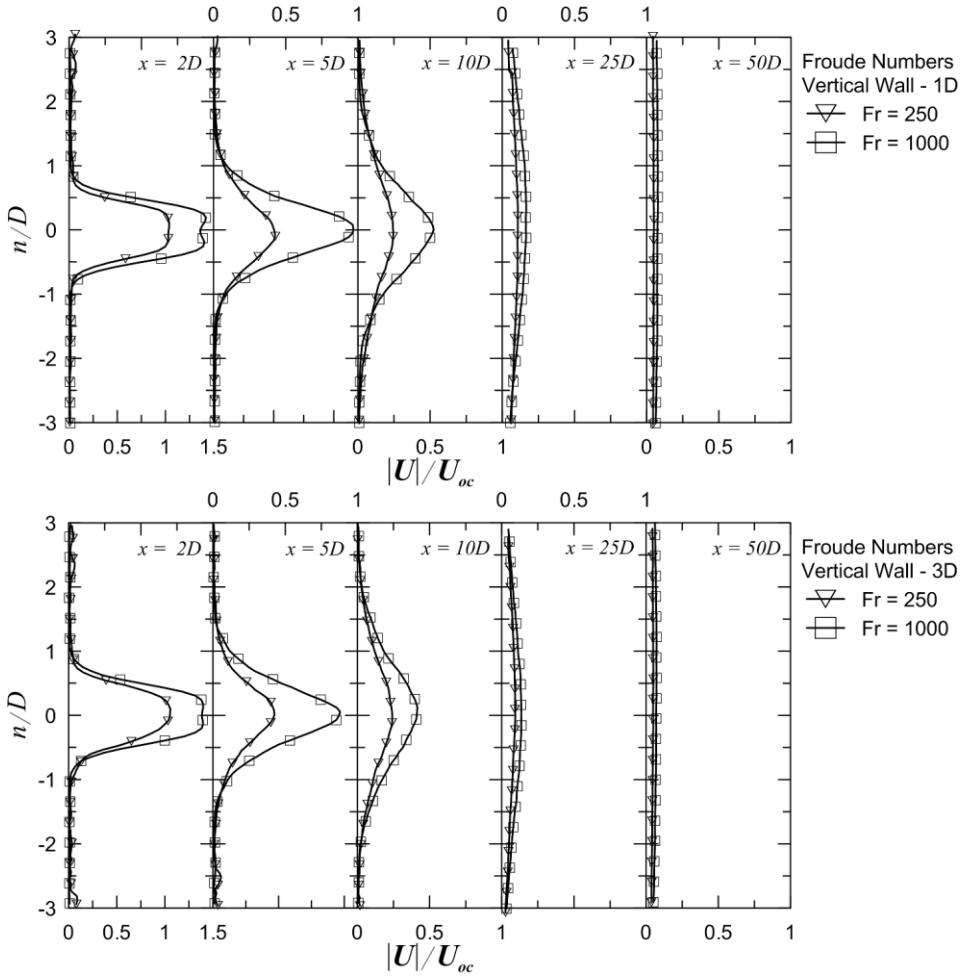

Figure 3.53 – Normalized velocity profiles for jets near the vertical wall surface with nozzle to surface distance of 1D (top) and 3D (bottom).

In momentum dominated regions (i.e. $s/D < 5$) velocity profiles were observed to be similar to those of free jet flows. However, at the far-field locations jet structure spread out more rapidly and overall jet structure were observed to be wider comparing to free jet cases. Limited ambient entrainment near the vertical wall surface led to the acceleration of the jet flow in the y- and the $+z$-direction in order to balance the total mass flow rate. The jet spread rate in the y-direction was observed to be more pronounced as a result of surface forces and the attachment of the jet to the wall surface which led to a wider overall jet structure comparing to free jet flows.

Slower decay rates were evident in cases closer to the wall surface. For instance the maximum peak velocity for Fr = 1000 at s/D = 10 were seen to be $0.6U_{oc}$ for jet flow located at 1D distance from the wall surface. However, this value for the same cases located at 3D distance from the surface was found to be $0.45U_{oc}$.

For jet flows with nozzle to wall surface distance of 1D, velocity profiles at the jet far-field regions were seen to be slightly asymmetric as the peak velocity magnitude shifted towards the +n-direction due to the presence of strong buoyancy forces.

3.4.5 Turbulence Statistics

Normalized rms velocity components for jet flows near a boundary surface are presented in this section. Velocity fluctuations were normalized by the local time-averaged velocity along the jet centerline. The rms values were plotted along the jet centerline coordinate, s, normalized by jet diameter, D. Radial turbulent kinetic energy components at several downstream locations are also included in this section. Stress profiles were normalized by the time-averaged nozzle exit velocity and were plotted against the jet normal axis, n.

3.4.5.1 Ground

Turbulent statistics for jet flows near the ground surface are discussed in this section. Normalized rms values of fluctuating velocity components along the jet centerline are shown in Figure 3.54. High initial turbulence intensities of the sharp edged inflow condition led to a low initial value in fluctuating velocity components. Downstream of the potential core region, the fluctuating velocity profiles were sharply increased to a peak value. These peaks were more evident for Fr = 250 cases. The axial

fluctuating components were observed to have higher value comparing to radial components. Same behaviours were also observed in the free jet flows. However, the differences between axial and radial values were observed to be more distinct comparing to free jet flows.

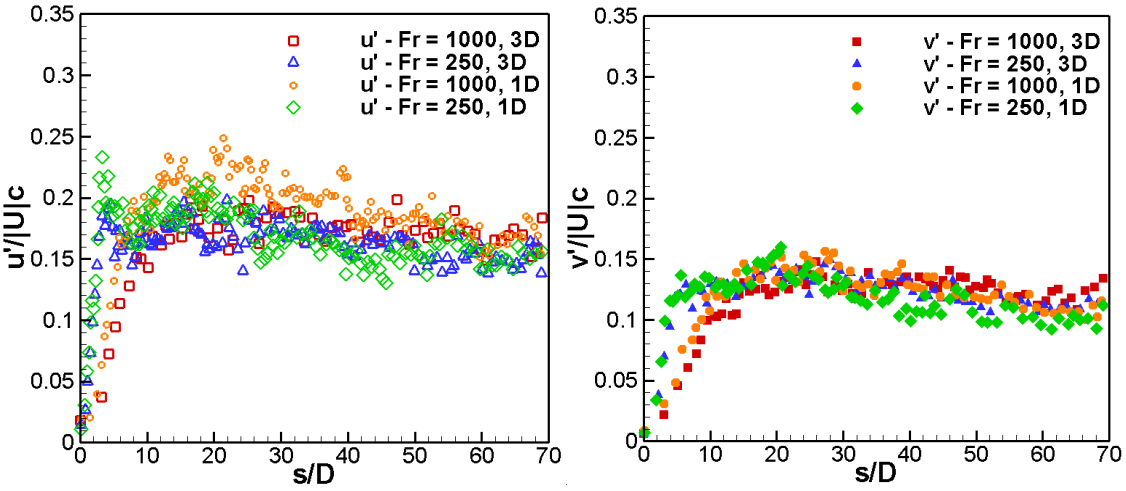

Figure 3.54 – Normalized velocity fluctuations along jet center line, jet near ground surface.

The axial rms profiles reached a peak values of 0.24 for *Fr* = 250 and 1000 located at 1*D* distance from the ground surface. However, the peak values of 0.2 and 0.18 were observed for jets located at 3*D* from the ground surface accordingly. The rms values were observed to be generally higher than those of free jet flows. The opposite direction of buoyancy and surface forces in flows near the ground surface reduced the surface effects to some extent specifically at cases farther away from the surface. For instance, the fluctuating components were observed to have a slightly higher magnitude comparing to those of free jet flows but the overall profiles were seen to be very similar to free jet cases.

For jet flows located at 1*D* distance from the ground surface, the fluctuating velocity components were almost twice larger in magnitude comparing to free jet cases

especially at the jet to surface attachment point. This was due to the presence of wall boundary layer which retarded the jet flow. However, farther downstream, these fluctuating components reached asymptotic values as the wall boundary layer developed. The axial and radial fluctuating components reached asymptotic values of 0.17 and 0.12 respectively at $s/D = 40$. The asymptotic ratio of $v'/u' \approx 0.7$ was observed in jet flows near the ground surface.

Components of turbulent kinetic energy for jet flows located at 3*D* distance from the ground surface are presented in Figure 3.55. Downstream of the nozzle exit, in potential core region, axial and radial components of turbulent normal stresses showed two distinct peaks near the upper and lower boundary of the jet flow due to jet shear layer instabilities along boundaries. Axial stresses were observed to be substantially higher comparing to radial components. This is due to the presence of strong pressure gradient along the *y*-direction which suppressed the radial components of turbulent kinetic energy. The peak values in axial turbulent stress profiles near the jet upper boundary were seen to be slightly stronger in jet near-field regions. This was due to the presence of surface forces which forced the overall jet structure down towards the ground surface. At downstream of the potential core region, the distinct peaks in turbulent normal stress profiles joint together.

The turbulent shear stress profiles, $<u'v'>$, was observed to have a two peaked profile with a positive peak near the jet's lower boundary and a negative peak near the jet upper boundary. The turbulent shear stresses had smaller peak magnitudes comparing to those of normal stresses at the jet near-field regions. As the jet evolved at

the jet far-field regions, the higher ambient entrainment led to the higher generation of turbulent shear stress.

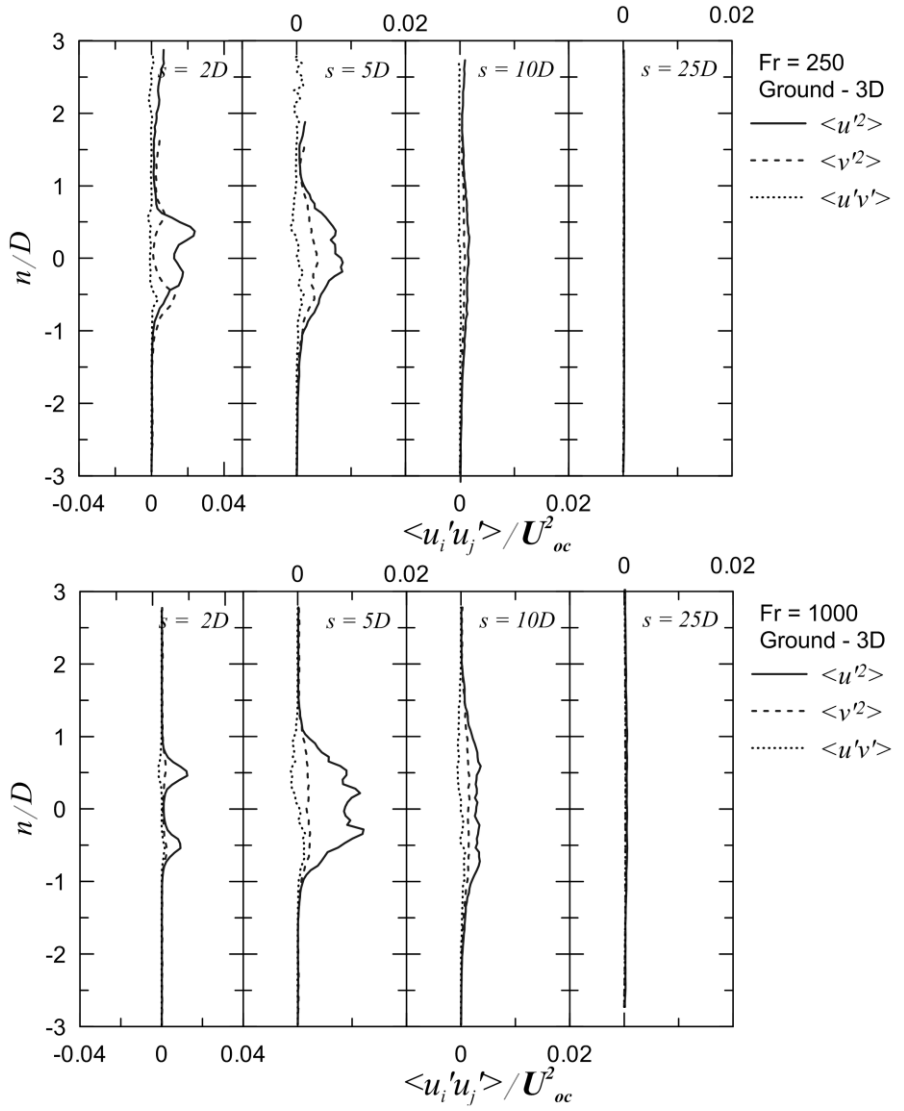

Figure 3.55 – Stress profiles in jet center-plane for jets located at 3*D* from ground surface (a) Fr = 250, (b) Fr = 1000.

In the potential core region, the peaks in $\langle u'v' \rangle$ profiles were aligned by the jet centerline. However, at the far-field locations the regions with negative $\langle u'v' \rangle$ were seen to become stronger relative to the positive peak. This was due to limited ambient entrainment in the jet's lower boundary adjacent to the ground surface as the ambient

entrainment in jet's upper boundary became the dominant mechanism for generation of turbulent shear stress.

The profiles of components of turbulent kinetic energy for jet flows located at 1*D* distance from the ground surface at different fixed downstream locations are shown in Figure 3.56.

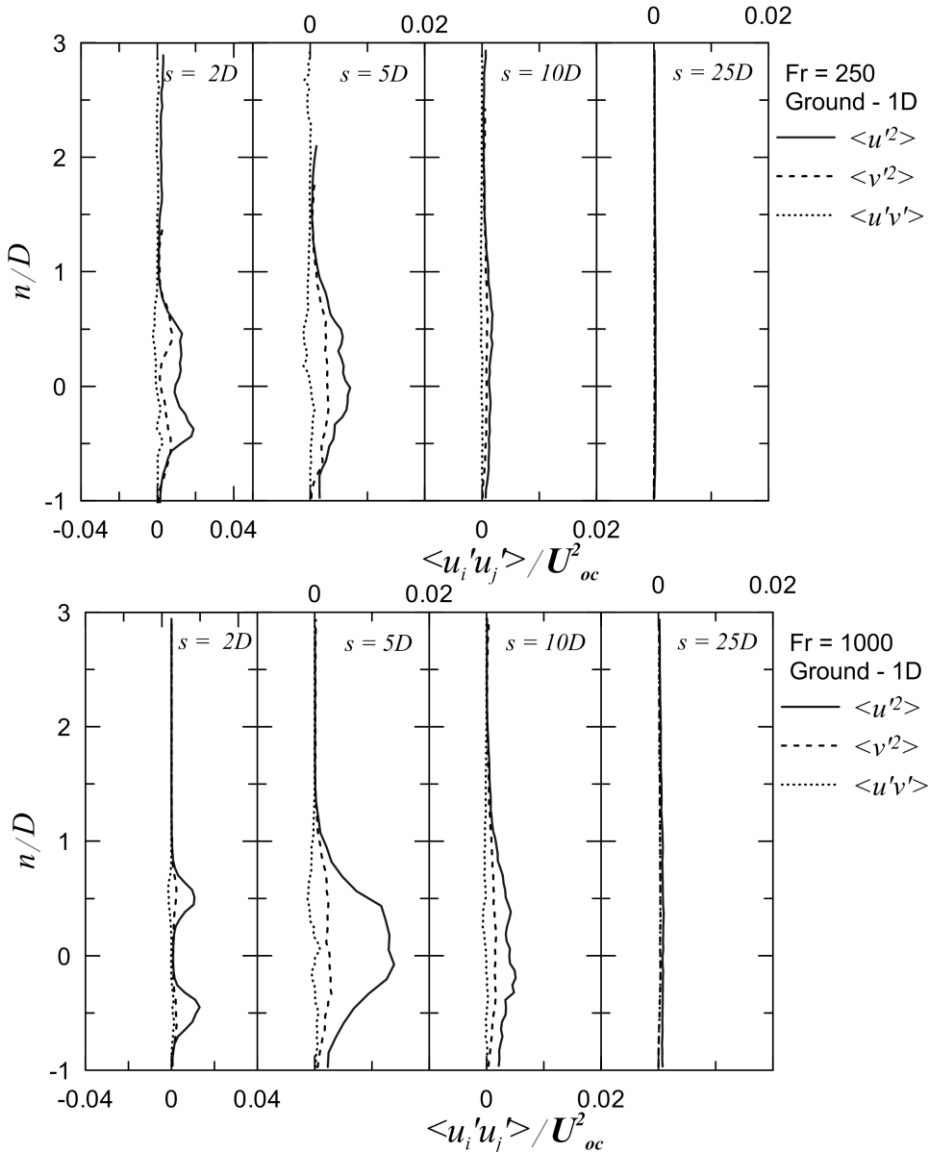

Figure 3.56 – Stress profiles in jet center-plane for jets located at 1*D* from ground surface (a) Fr = 250, (b) Fr = 1000.

Two distinct peaks were evident in profiles of turbulent stresses at the jet near-field regions. The $<u'^2>$ component of turbulent stresses showed higher values comparing to radial components, $<v'^2>$, and shear stresses, $<u'v'>$. Limited ambient entrainment at the jet's lower boundary led to accelerated flow in the upper boundary. This resulted the axial component of turbulent normal stresses to show a slightly stronger peak near the jet's lower boundary adjacent to the ground surface. For Fr = 250 the profiles were no longer aligned by the jet centerline as a result of the strong interaction between the jet and the ground surface.

At the jet far-field regions, axial and radial components of turbulent stresses showed single peaked profiles. However, these single peaked profiles were observed in farther downstream locations comparing to the free jet flows due to the lower ambient entrainment in the flows near the surface.

The profiles of the turbulent shear stress showed two peaked profiles in the jet near-field regions with a positive peak near the ground surface and a negative peak near the jet's upper boundary. These peak values were substantially lower comparing to those of normal stresses. At the far-field locations, the negative peak became stronger relative to positive peak located near the ground surface. Limited mixing along the jet's lower boundary weakened the positive peak as the ambient entrainment at the upper boundary became the dominant mechanism for generation of $<u'v'>$.

3.4.5.2 Ceiling

The rms of fluctuating velocity components normalized by local time-averaged velocity (i.e. $u'/|U|c$ and $v'/|U|c$) along the jet centerline coordinate system are

presented in Figure 3.57. The main difference between the jet flows near the ceiling surface relative to those near the ground surface discussed earlier is the direction surface forces. In cases near the ceiling surface the buoyancy forces and the ground forces were in the same direction and pushed the overall jet structure towards the ceiling surface.

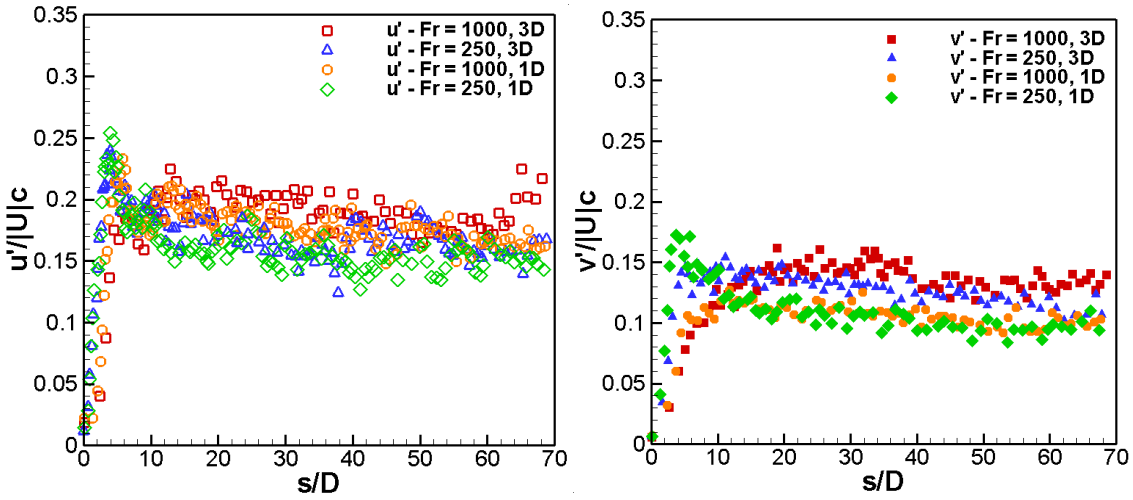

Figure 3.57 – Normalized velocity fluctuations along jet center line, jet near ceiling surface.

Sudden increase to the peak values in the turbulence intensities profiles were observed at downstream of the potential core region. The peak values were observed to be generally higher relative to the jet flows near the ground surface. This was due to higher combined buoyancy and surface forces which forced the jet to deflect towards the ceiling surface. The turbulent intensities reached the maximum values of approximately 0.25 and 0.24 for Fr = 250 located at 1D and 3D distance from the ceiling surface respectively. For Fr = 1000, the maximum values of 0.23 and 0.2 were observed for cases at 1D and 3D from the ceiling surface accordingly.

For jet flows closer to the ceiling surface, the radial and axial rms of fluctuating velocity components reached the asymptotic values of 0.11 at s/D = 12 and 0.17 at

s/D=20 respectively. However, for the flows located at 3*D* from the ceiling surface the values of 0.13 at *s/D* = 12 and 0.18 at *s/D* = 20 where observed accordingly. The lower asymptotic value for the cases closer to the ceiling surface can be explained by the development of the fully developed wall-jet structure. The buoyancy and surface forces pushed the jet structure towards the ceiling surface which resulted in a more developed boundary layer at the jet far-field regions. This developed boundary layer retarded the jet structure which together with the surface forces suppressed the radial components of velocity fluctuations. Similar to jets near the ground surface, the axial component of velocity fluctuations were observed to be generally higher comparing to radial components.

Figure 3.58 shows the radial distribution of components of the turbulent kinetic energy at the different downstream locations for jets located at 3*D* distance from the ceiling surface. Axial and radial components of turbulent normal stresses showed a two peaked profiles in the jet potential core region. These two peaks were aligned by the jet centerline and the magnitudes of the axial component were observed to be substantially greater than the radial component. The $<u'^2>$ components were observed to have a slightly stronger peak near the jet's lower boundary. At the jet far-field locations, at *s/D* > 5, as the jet deflected towards the ceiling surface, the axial and radial components of turbulent normal stresses showed single peak profiles. The maximum $<u'^2>$ occurred closer to the jet lower boundary and the maximum of $<v'^2>$ was located closer to ceiling surface. This peak misalignment continued at the jet far-field regions.

Turbulent shear stresses showed a negative peak near the jet's upper boundary and a weak positive peak near the jet's lower boundary. At the jet far-field locations the

negative peak near the ceiling surface became stronger as the overall jet structure deflects towards the ceiling and the ambient entrainment at upper boundary became the dominant mechanism for $<u'v'>$ generation. Downstream of the jet to surface attachment point, the jet lower boundary observed to be the main source of turbulent shear stress generation as the upper boundary is restricted by the ceiling surface.

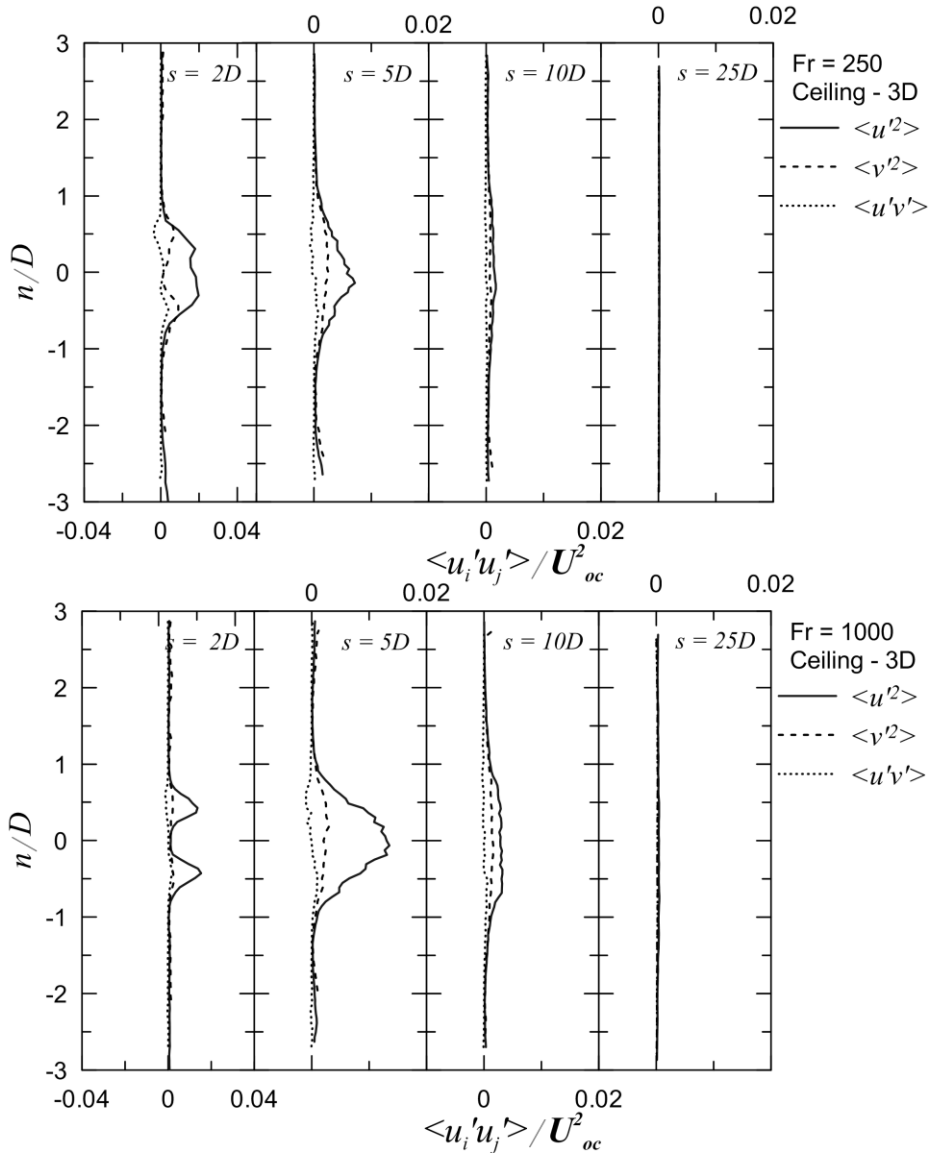

Figure 3.58 – Stress profiles in jet center-plane for jets located at 3*D* from ceiling surface (a) Fr = 250, (b) Fr = 1000.

The radial turbulent stress profiles at different downstream locations for jet flows located at 1*D* distance from the ceiling surface are presented in Figure 3.59.

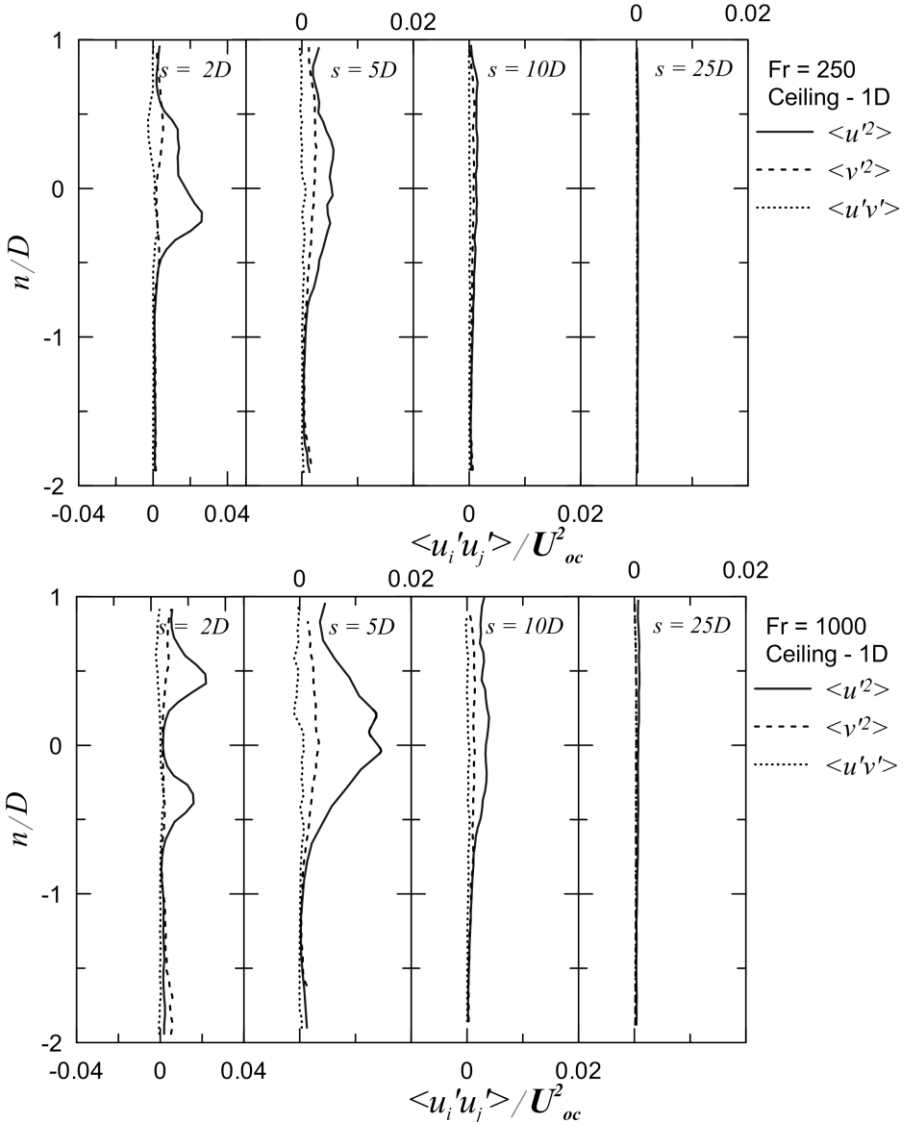

Figure 3.59 – Stress profiles in jet center-plane for jets located at 1*D* from ceiling surface (a) Fr = 250, (b) Fr = 1000.

For *Fr* = 250, an asymmetric two peak $<u'^2>$ profile with a stronger peak near the jet lower boundary was seen at *s/D* = 2 in the jet near-field region. The deflection of jet structure towards the ceiling surface under the influence of buoyancy and surface forces decelerated the jet lower boundary which accelerated the jet flow near the ceiling surface before the attachment point. This led to the presence of the stronger $<u'^2>$ peak

near the slower moving boundary and also the stronger $<v'^2>$ values near the upper boundary. Downstream of the jet to surface attachment point (i.e. $s/D > 5$) the $<u'^2>$ profiles showed a single peaked distribution with the maximum located near the ceiling surface due to development of the wall boundary layer which retarded the jet flow. The $<u'v'>$ generation mechanism was restricted near the ceiling surface which led to the presence of a small positive peak near the jet lower boundary in $<u'v'>$ profiles.

For Fr = 1000, higher jet initial momentum prevented the jet sharp deflection towards the ceiling which led to an almost symmetric two peak $<u'^2>$ profile at s/D = 2. As the jet momentum decayed downstream the potential core region, these two peaks joint together to form a single peaked profile. At $s/D > 10$, axial turbulent normal stress component showed a single peaked profile with the maximum value close to the ceiling surface. The $<u'v'>$ generation mechanism was similar to that of Fr = 250.

3.4.5.3 Vertical Wall

The rms of velocity fluctuations for jet dispersion near the vertical wall surface are shown in Figure 3.60.

The normalized rms velocity components ($u'/|U|c$ and $v'/|U|c$) along the jet centerline were observed to be similar to those of free jet flows. However, the potential core regions were appeared to be slightly longer in jet cases near the vertical wall due to lower ambient entrainment at the jet boundary close to the wall surface. In general rms values were observed to be slightly lower comparing to jet flows near ceiling and ground surfaces. However, these rms values were slightly higher than those in free jet flows due to the presence of the wall surface which retarded the jet flow.

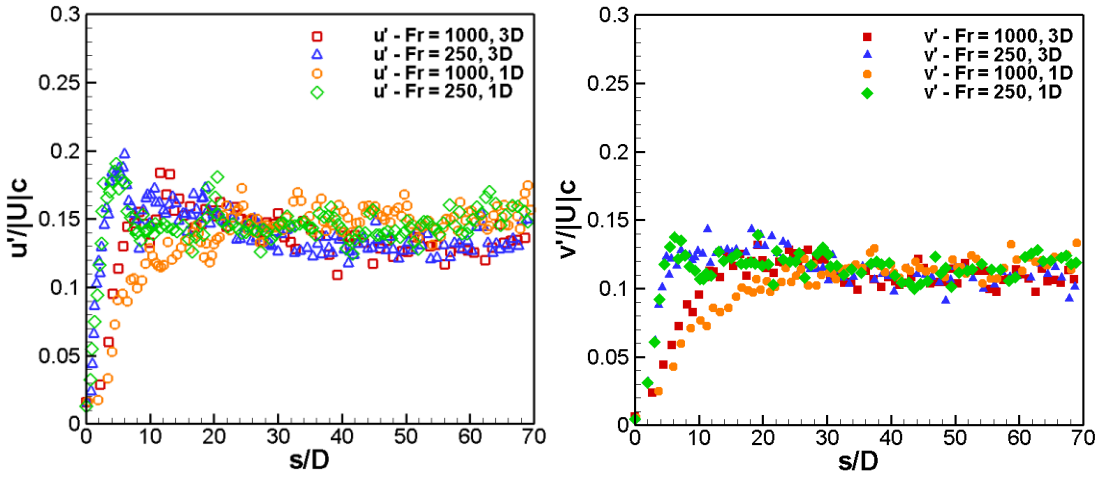

Figure 3.60 – Normalized velocity fluctuations along jet center line, jet near vertical wall surface.

The axial velocity fluctuation components were generally higher than radial fluctuations for all cases considered herein. Downstream of the potential core region, sudden increase in the turbulent intensity values to peak values of 0.19 for *Fr* =250 and 0.17 for *Fr* =1000 were observed. The axial and radial rms values for jet flows located at 1*D* distance from the wall surface reached the asymptotic value of 0.15 at *s/D* = 20 and 0.12 at *s/D* = 25 respectively. These values were observed to be 0.13 at *s/D* = 30 and 0.11 at *s/D* = 35 for the flows located at 3*D* from the wall surface respectively. The higher asymptotic turbulent intensity values for cases located at 1*D* distance from the wall surface was due to the faster development of wall-jet structure in these cases. Development of wall-jet structure led to a more developed wall boundary layer which retarded the jet flow. The asymptotic ratio of $v'/u' \approx 0.8$ was observed in jet flows near the wall surface.

Figure 3.61 shows the components of turbulence kinetic energy for the jet flows located at 3*D* distance from the wall surface. Component of turbulent stresses showed a two peaked profiles aligned by the jet centerline in the jet potential core region. The $<u'^2>$ components presented higher values comparing to radial component, $<v'^2>$ and

shear stress components, $<u'v'>$. The peaks in stress profiles were located near the jet's upper and lower boundary which showed shear layer instability along the jet boundary at the potential core region. At the jet far-field regions the peaks in turbulent stresses profiles moved closer to the jet centerline.

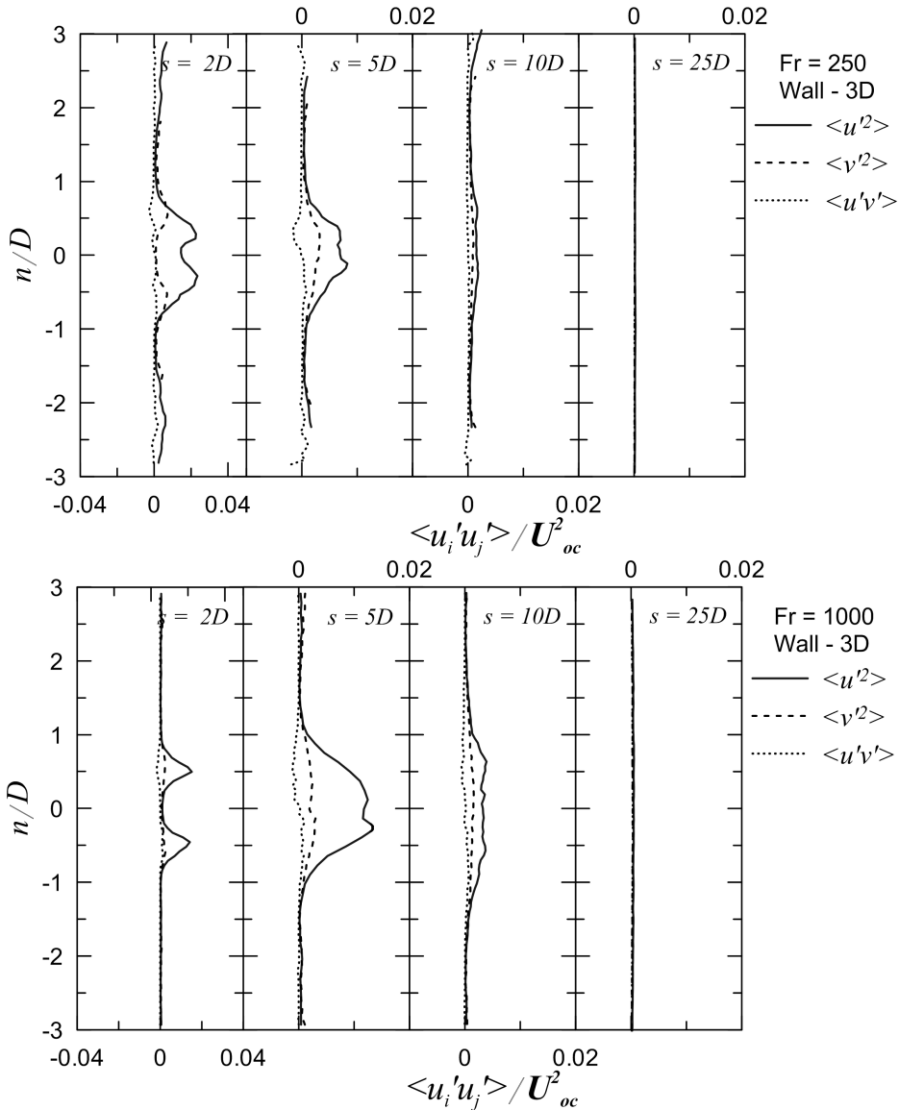

Figure 3.61 – Stress profiles in jet center-plane for jets located at 3*D* from vertical wall surface (a) Fr = 250, (b) Fr = 1000.

At *s/D* = 5 the $<u'^2>$ component of turbulent stresses developed a stronger peak near the lower boundary due to presence of strong buoyancy forces which led to the jet deflection towards the +*y*-direction. As the jet structure deflected towards the direction

of buoyancy forces, the lower boundary of the jet decelerated which led to the acceleration of the jet upper boundary in order to fulfill the mass balance. The deceleration of the jet lower boundary resulted in a stronger peak in $<u'^2>$ profiles near the lower boundary whilst the faster moving upper boundary led to a stronger peak in $<v'^2>$ profiles near the upper boundary. These peaks were more evident for Fr = 250 plots at s/D = 5 due to presence of stronger buoyancy forces. The $<u'v'>$ instabilities became stronger at the far-field locations as more ambient mixing occurred.

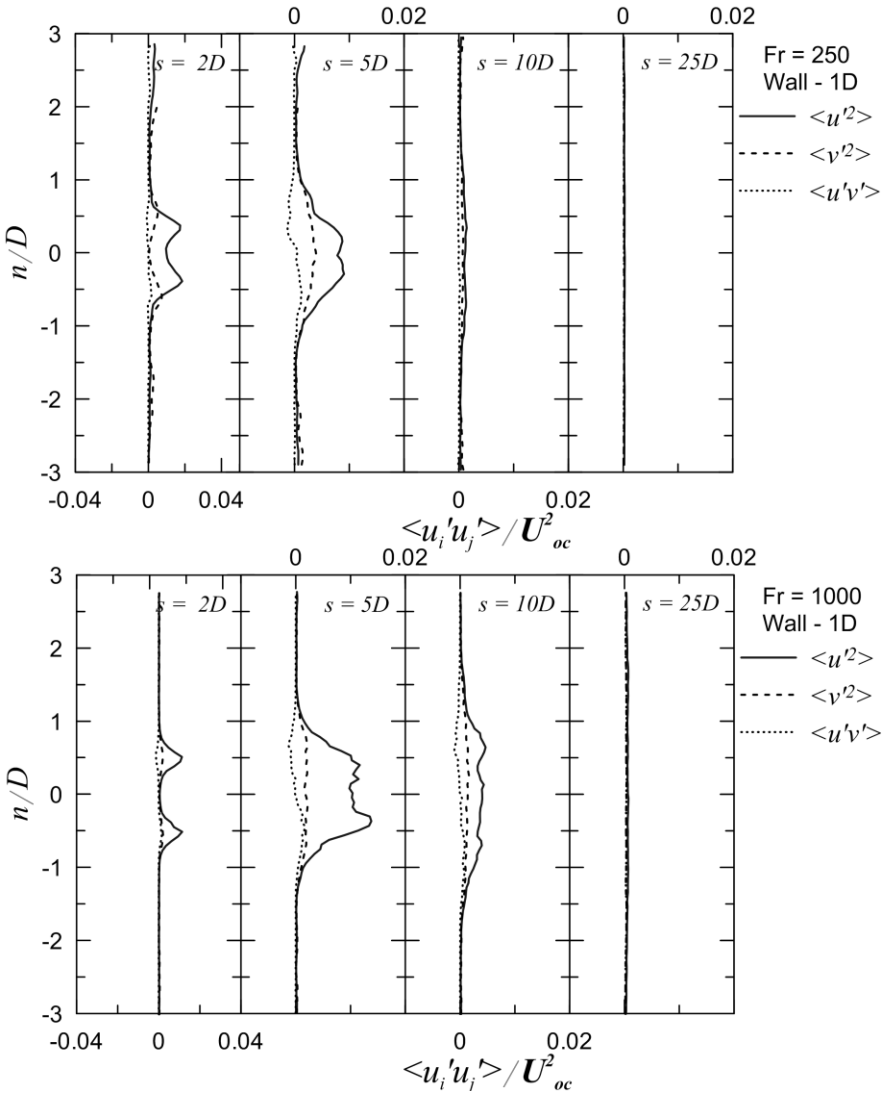

Figure 3.62 – Stress profiles in jet center-plane for jets located at 1D from vertical wall surface for Fr = 250 (top) and Fr = 1000 (bottom).

The components of turbulent shear stresses for jet cases located at 1*D* distance from the vertical wall surface are presented in Figure 3.62. Conclusions similar to those of jet flows located at 3*D* distance from the vertical wall surface can be drawn for the jet flows located at 1*D* from the wall surface. However, the effects of surface forces were observed to be more pronounced in these cases. For instance the peaks in $<u'^2>$ profiles at *s/D* = 5 were more pronounced near the jet's lower boundary. This was due to the development of the wall boundary layer which retarded the jet flow and led to a stronger buoyancy effects and the faster jet deflection.

3.4.6 Flow Structure in Jets Near a Surface

Flow vorticity and streamlines representations for the jet flows near the boundary are discussed in this section.

3.4.6.1 Ground

Time-averaged out-of-plane vorticity contours for the jet flows adjacent to the ground surface are shown in Figure 3.63. Downstream of the jet to surface attachment point at downstream of the potential core region, the jet upper boundary was decelerated as a result of surface forces which force the jet flow to turn towards the ground surface. In the same region, the jet boundary near the ground surface accelerated and widened slightly in order to balance the mass flow rate. The wide lower boundary led to a bigger circulation region which is more visible in Figure 3.63.d. This wide circulation region was restricted by the surface in cases closer to the ground surface and led to the attachment point in the cases located at 1*D* distance from the ground surface. Downstream of the potential core region the jet centerline velocity

decayed gradually which resulted in a more vulnerable jet structure to the surface forces.

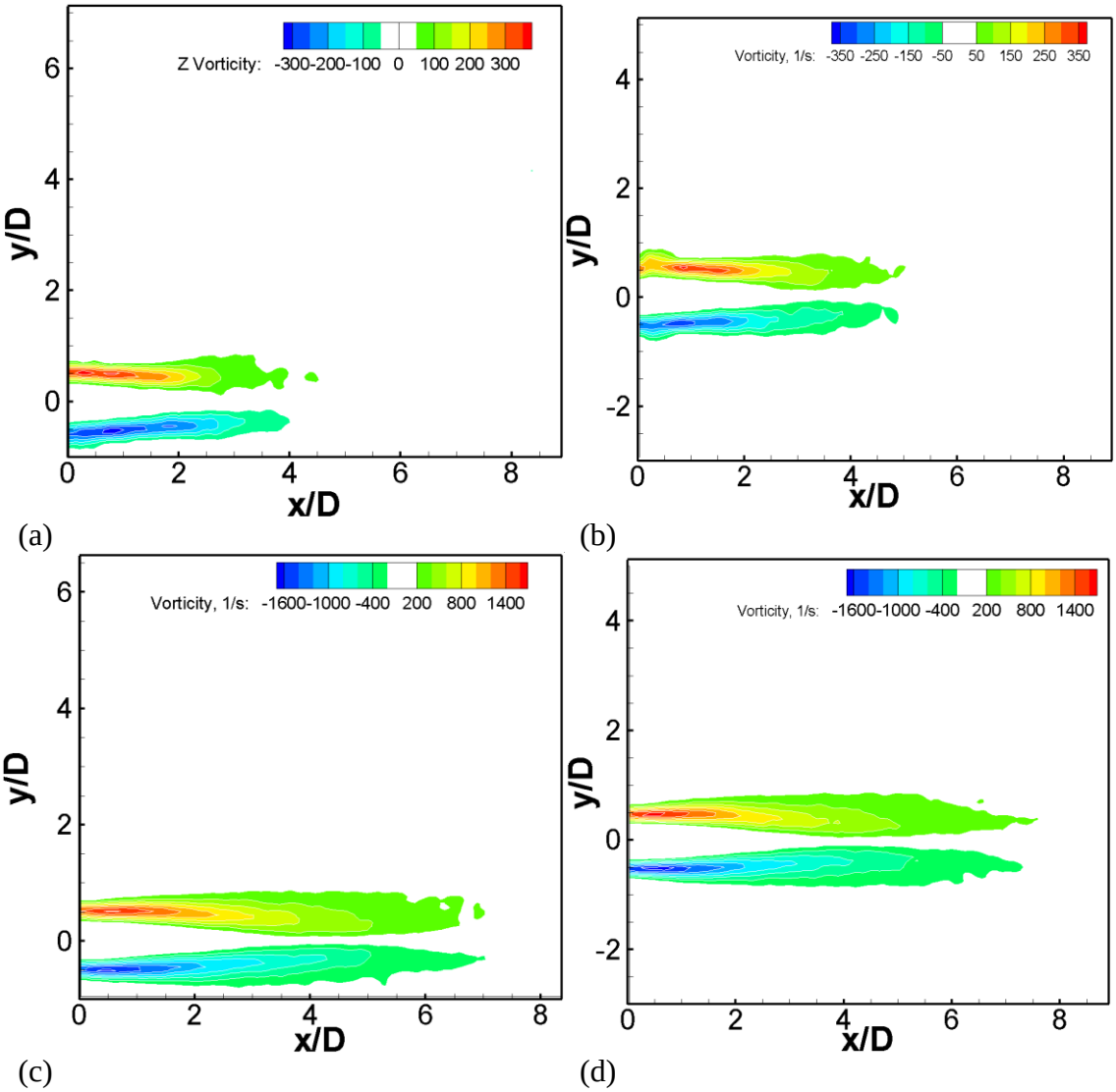

Figure 3.63 – Time-averaged out-of-plane vorticity contours for *Fr* = 250 located at (a) 1D, (b) 3D and *Fr* = 1000 located at (c)1D and (d) 3D from the ground surface.

Downstream of the jet to surface attachment point, the vorticity field in lower side of the jet adjacent to the ground surface were very restricted. Farther downstream, development of the wall boundary layer decelerated the jet lower boundary which led to the acceleration of the upper boundary to fulfill the mass flow rate. The accelerated

flow caused the vortices to stretch in downstream direction. These stretched vortices were observed to join together which led to the regions of strong turbulence quantities.

Propagation of the wall boundary layer at the jet far-field regions retarded the jet flow adjacent to the surface and led to a smaller velocity gradient between the upper jet boundary and regions close to the surface which led to the dissipation of flow vorticity. The magnitude of the maximum vorticity dropped in the jet downstream distance but the circulation area was widened in the jet upper boundary.

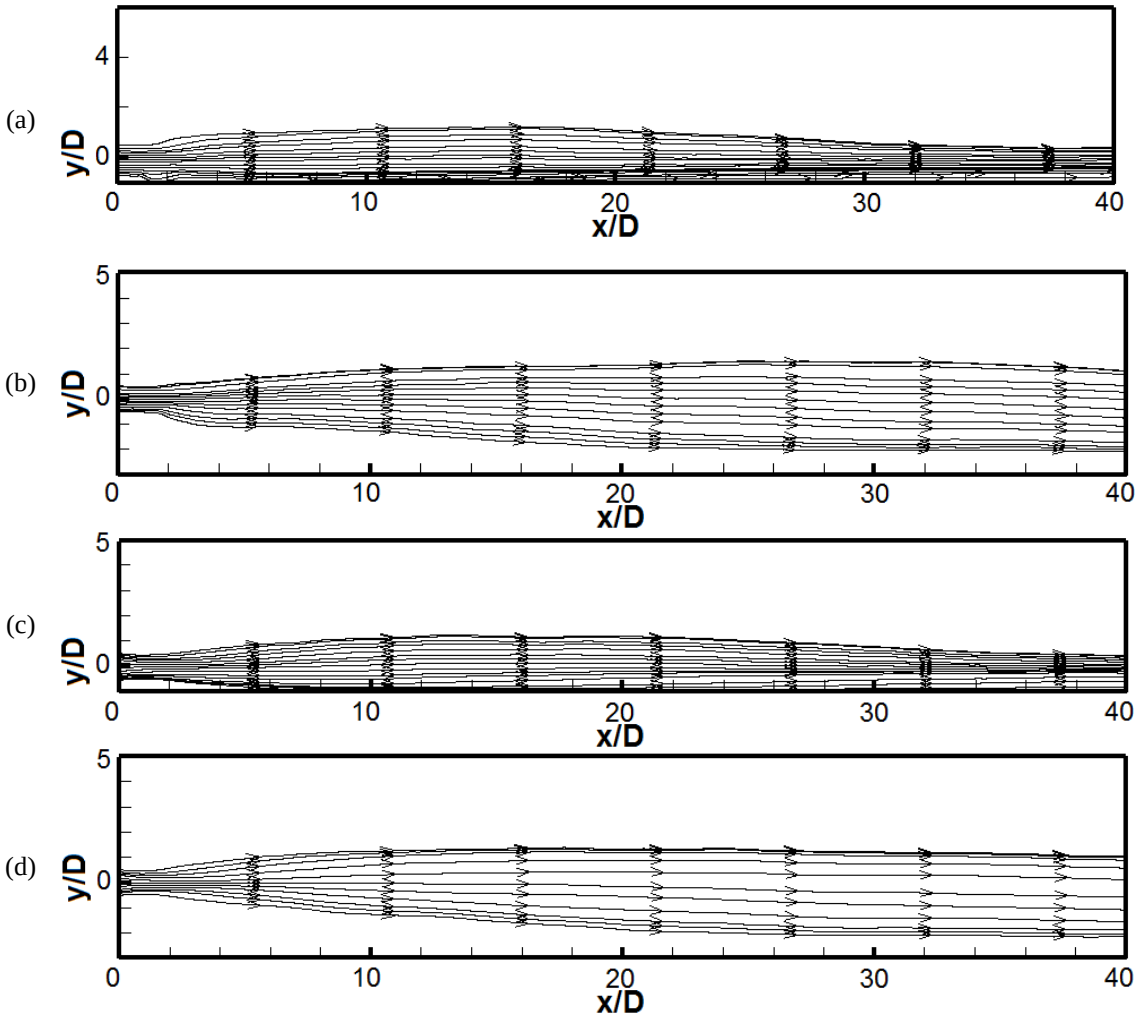

Figure 3.64 – Flow streamlines for *Fr* = 250 with nozzle to surface distance of (a)1D, (b) 3D and *Fr* = 1000 with nozzle to surface distance of (c)1D and (d) 3D - Jet near ground surface.

Flow streamlines for the jet flows near the ground surface are presented in Figure 3.64. Arbitrary spacing between streamlines was selected and they do not necessarily represent the stream function values. The jet streamlines showed a general waviness along the jet upper boundary. This waviness was also observed in crossflowing jets which show an effective mixing with ambient at these areas. This waviness pattern may be explained by the jet momentum. Starting from the nozzle tip in the jet upper boundary side and moving towards downstream regions, the jet initial momentum decayed under the influence of surface forces which decelerated the jet upper boundary. Flow kinetic energy dissipated into heat and turbulent kinetic energy in these regions. However, the jet's lower boundary was restricted by the ground surface with limited ambient entrainment. The rate of dissipation of kinetic energy into heat was expected to be more at the jet lower boundary adjacent to the surface comparing to the upper boundary. However, the jet acceleration and the wider jet structure at the upper boundary led to the higher dissipation of jet kinetic energy into turbulent kinetic energy at this boundary which led to an efficient mixing and waviness pattern.

The widening of the jet's lower boundary downstream of the attachment point is more evident in cases located farther away from the ground surface (see Figure 3.64.*b* for instance). On the other hand, the widened upper boundary after the jet to surface attachment point was more pronounced in cases closer to the ground surface which is shown in Figure 3.64.*a* and *c*. The deflection of the overall jet structure towards the ground surface due to the surface forces was observed in Figure 3.64.*b* and *d*.

3.4.6.2 Ceiling

The time-averaged out-of-plane vorticity contours for the jet flows near the ceiling surface are presented in Figure 3.65.

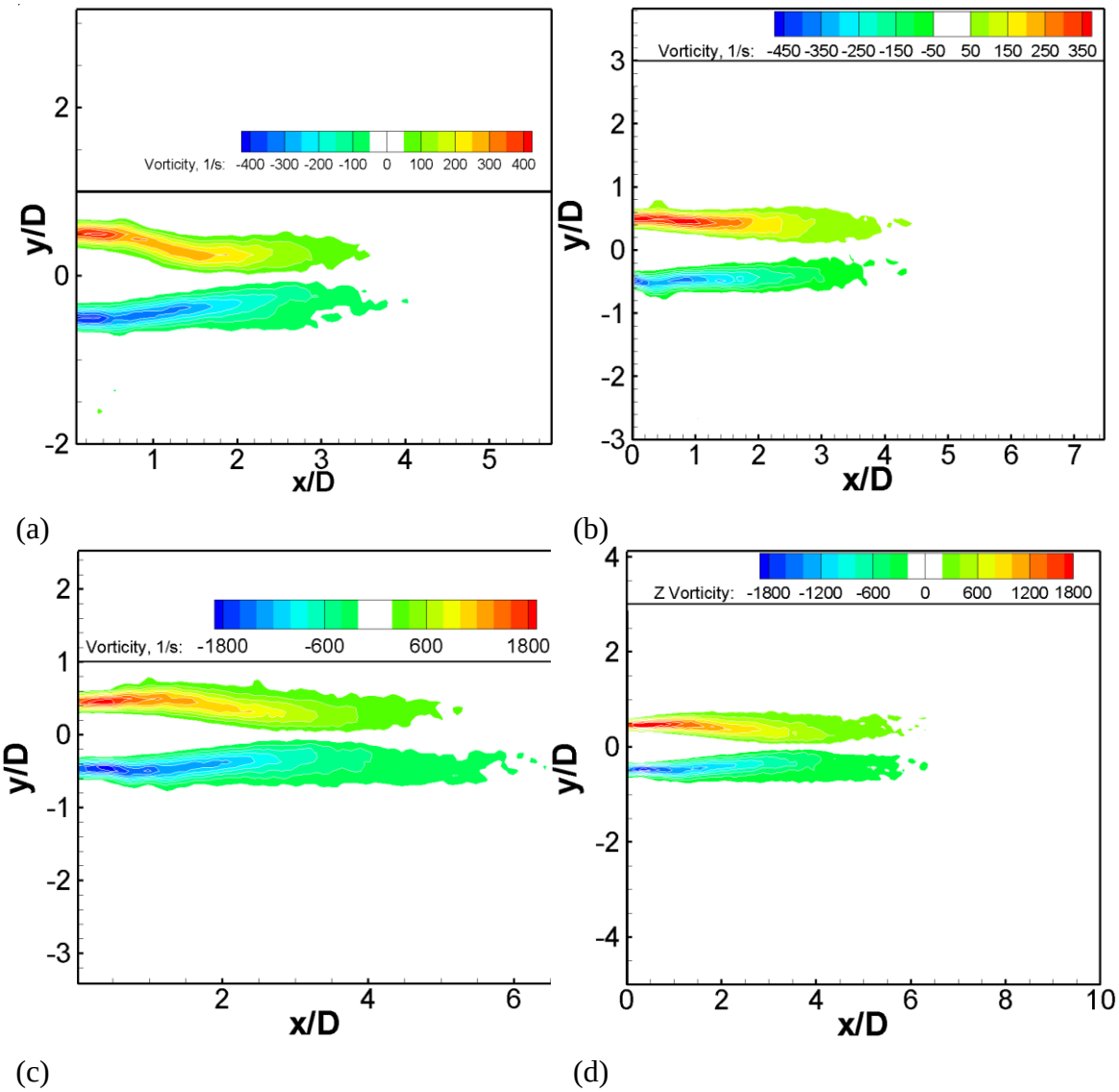

Figure 3.65 – Time-averaged out-of-plane vorticity contours for *Fr* = 250 located at (a) 1D, (b) 3D and *Fr* = 1000 located at (c) 1D and (d) 3D from the ceiling surface.

As mentioned before, in these cases buoyancy forces acted in the same direction as the surface forces which led to more developed wall-jet structure.

Downstream of the jet to surface attachment point, the jet lower boundary decelerated due to the presence of buoyancy and surface forces which forced the jet structure towards the ceiling surface. The deceleration of the lower boundary accelerated and widened the jet's upper boundary. This wider boundary was more evident in jet flows located at 3*D* distance from the ceiling surface (see Figure 3.65.*b* at $x/D = 3$). Downstream of the jet to surface attachment point, the jet's boundary near the ceiling surface decelerated drastically which led to the acceleration and widening of the jet's lower boundary to fulfill the mass flow rate (see Figure 3.65.*a* at $x/D = 2.5$). The accelerated flow in the jet lower boundary then stretched the vortices in downstream direction which forced the vortices in this region to join and produce regions of strong turbulence. The stretched vortices were more pronounced in $Fr = 1000$ at 1*D* distance from the ceiling surface (see Figure 3.65.*c* at $x/D = 4$). At the jet far-field locations, flow vorticity fields dissipated as the ceiling boundary layer propagated more in the jet structure.

Resultant flow streamlines representation from the time-averaged velocity field for jet flows near the ceiling surface are shown in Figure 3.66. The spacing and locations of the stream lines were selected arbitrarily and does not necessarily represent the stream function values.

For the cases located at 1*D* distance from the ceiling surface the jet propagation in the *y*-axis was observed to be lower comparing to flows near the ground surface. This was due to the combined buoyancy and surface effects which forced the overall jet structure towards the ceiling surface. The overall waviness of the jet lower boundary away from the ceiling surface was observed to be lower comparing to the jet flows near

the ground surface. This can be related to the lower mixing rates and the presence of lower turbulence intensities in jet flows near the ceiling surface due the development of wall-jet structure in these cases.

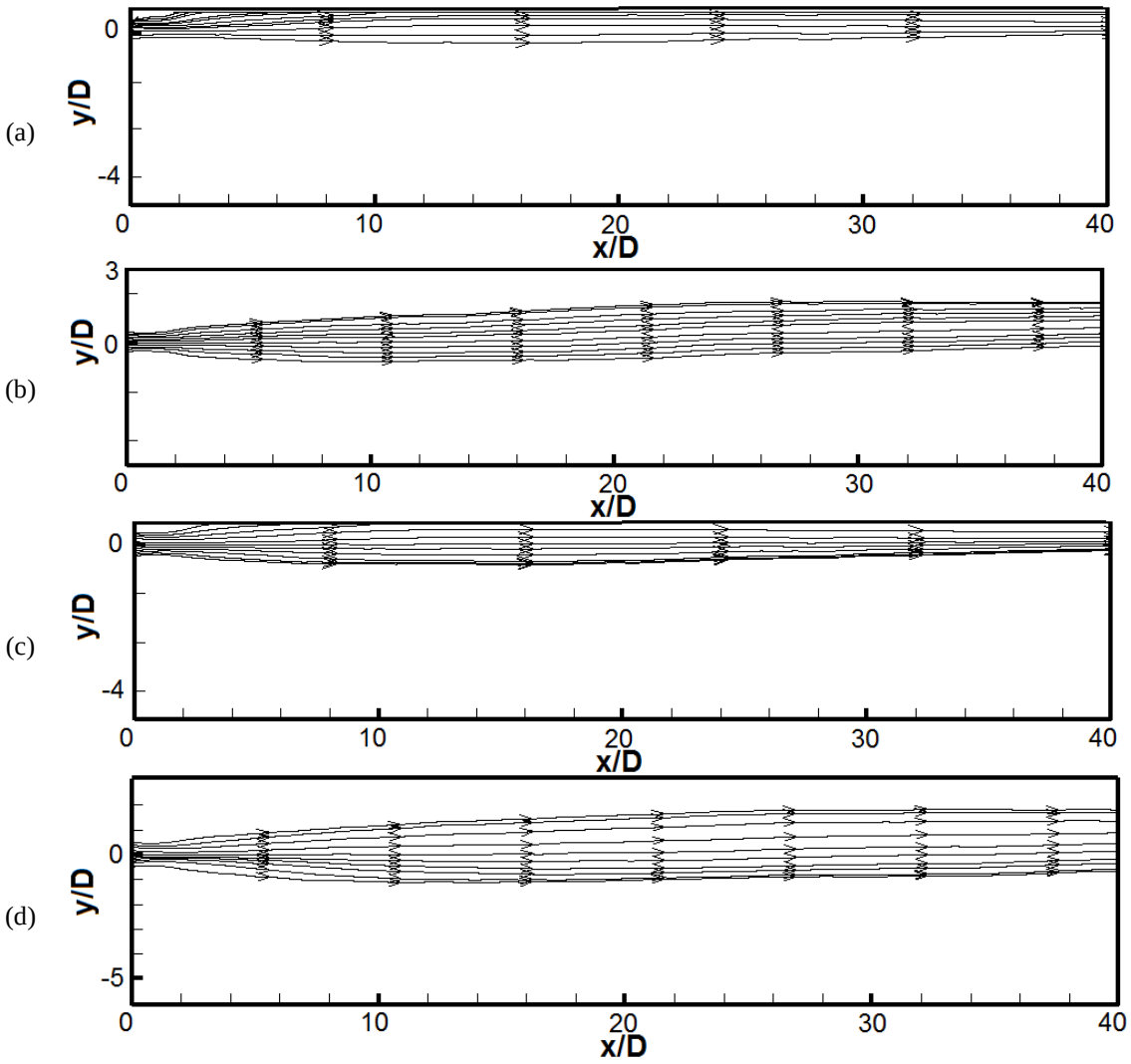

Figure 3.66 – Flow streamlines for *Fr* = 250 located at (a) 1D, (b) 3D and *Fr* = 1000 located at (c) 1D and (d) 3D from the ceiling surface.

The overall jet deflection towards the ceiling surface was more evident in jet flows located at 3*D* distance from the ceiling surface (see Figure 3.65.*b* and *d*). The jet deflection towards the surface was more pronounced in *Fr* = 250 due to presence of strong buoyancy forces.

3.4.6.3 Vertical Wall

Figure 3.67 shows the vorticity contours calculated from the time-averaged velocity fields for the jet dispersion cases near the vertical wall surface.

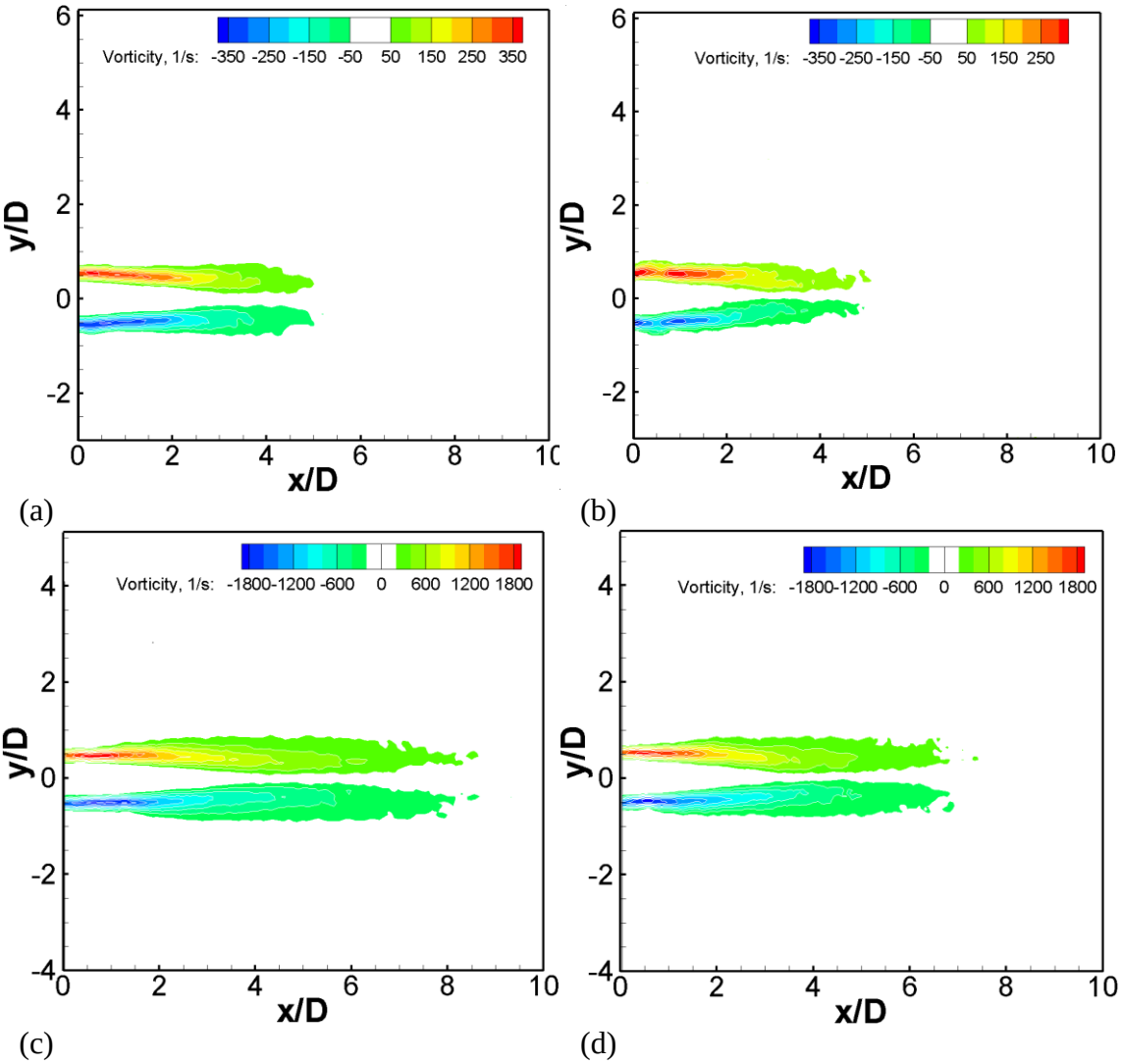

Figure 3.67 – Time-averaged out-of-plane vorticity contours for *Fr* = 250 located at (a) 1D, (b) 3D and *Fr* = 1000 located at (c)1D and (d) 3D from the vertical wall surface.

Buoyancy and surface forces in these cases acted in two different planes and the experimental configuration was set in order to capture the buoyancy effects only. The maximum vorticity magnitude was observed to drop in downstream location for all cases considered herein. Upstream of the jet to surface attachment point, the surface

forces deflected the overall jet structure towards the wall surface. This jet deflection decelerated the jet front boundary (located at +*z*-direction) which accelerated the back boundary of the jet and widened the jet's boundary in the direction of the wall surface. Downstream of the jet to surface attachment point, the jet back boundary adjacent to the wall surface decelerated drastically due to the interaction of the jet with the wall surface. This accelerated the jet front boundary and widened the jet circulation in those areas. These effects were more pronounced in jet flows located at 1*D* distance from the wall surface (see Figure 3.67.*a* and *c*). The acceleration of the jet front boundary led to the vorticity field stretch in the downstream direction. The interaction of the stretched vortices in those regions led to the presence of strong turbulence regions which resulted in higher turbulence intensities in these cases comparing to free jet flows. The stretched vorticity field was more evident for Fr = 1000 located at 1*D* distance from the wall surface due to higher initial momentum and the presence of the stronger surface forces relative to jet flows located at 3*D* distance from the wall surface. For instance the 200 vorticity field for Fr = 1000 was stretched to x/D = 6 and 8 at 3*D* and 1*D* distance from the wall surface respectively. The stretched vorticity field for Fr = 1000 and 250 located at 1*D* distance from the wall surface, resulted in higher turbulence intensities comparing to those located at 3*D* distance from the wall surface as shown in Figure 3.60 and also in section 3.4.5.3.

The flow streamlines representations for the cases near the vertical wall surface are presented in Figure 3.68.

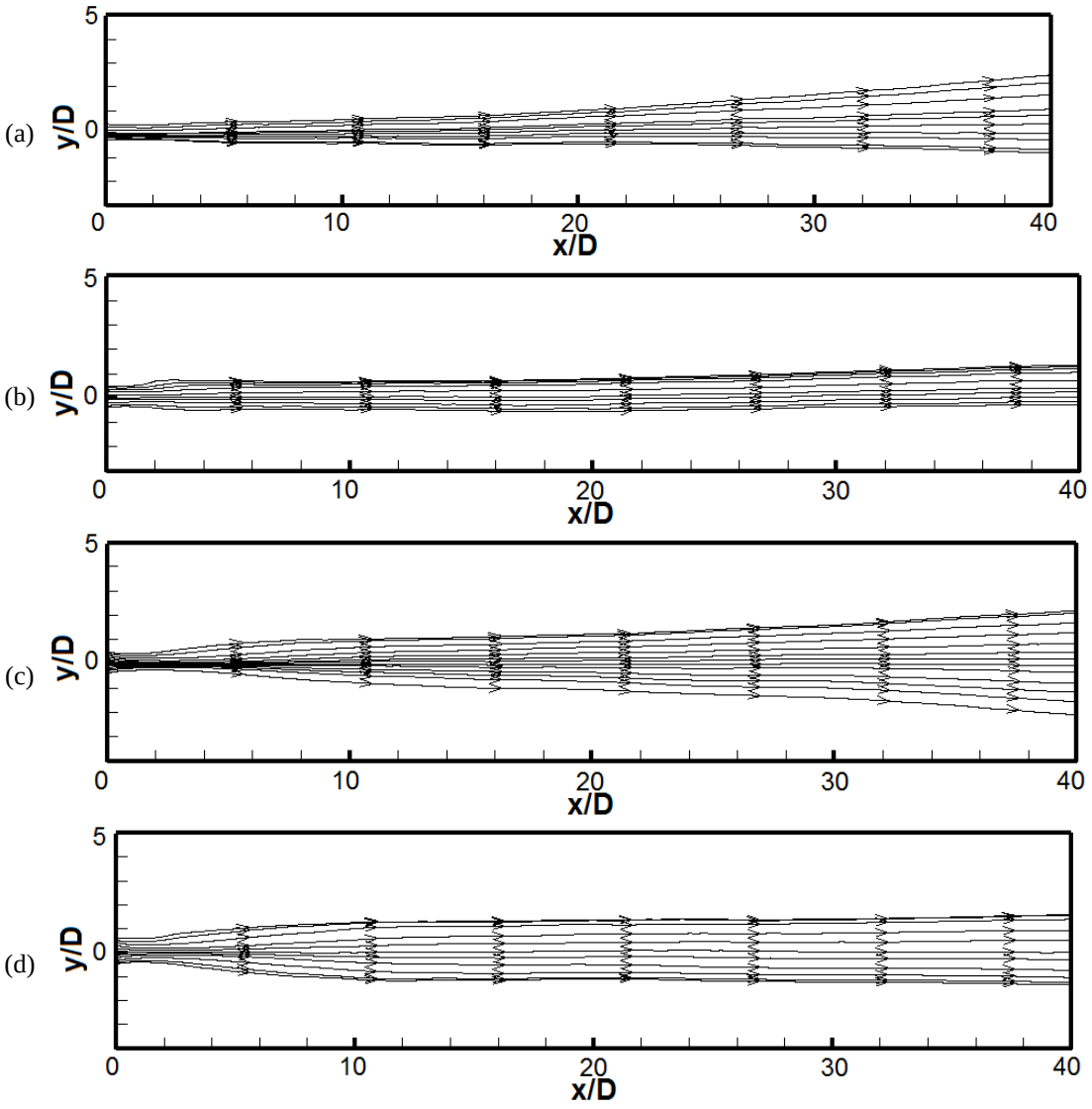

Figure 3.68 – Flow streamlines for *Fr* = 250 located at (a) 1D, (b) 3D and *Fr* = 1000 located at (c) 1D and (d) 3D from the vertical wall surface.

The streamlines were observed to diverge at the jet far-field regions for jet flows located at 1*D* distance from the wall surface. This was due to the presence of stronger surface forces and fully developed wall-jet flow structure in these cases. The fully developed wall-jet flow structure resulted in a more developed wall boundary layer which retarded the flow structure. The effects of buoyancy forces were observed to be stronger in *Fr* = 250 at the jet far-field regions. The overall jet structure for *Fr* = 1000

propagated almost symmetrically at the jet far-field regions. However, for Fr = 250, the jet streamlines deviated slightly from the nozzle axis at the jet far-field regions. For these flows, the jet centerline deflections were observed at x/D = 30 and 40 for flows located at 3D and 1D distance from the wall surface respectively.

3.4.7 Flow Widths in Jets Near Surface

3.4.7.1 Ground

The jet boundary contours for the jet flows near the ground surface are illustrated in Figure 3.69. Similar to free and crossflowing jets, the flow boundary contours (solid line) were computed by first determining the flow centerline (dashed line), then marching in the centerline's normal direction till the time-averaged velocity values dropped to 20% of the centerline value at each downstream location.

The deflection of the jet centerline towards the ground surface is evident in the figure. As the flow developed in the downstream locations, the wall boundary layer near the ground surface thickened. This forced the points of maximum velocity and subsequently the jet centerline away from the ground surface at the jet far-field regions. The jet boundary contour growth was observed to be similar to those of free jet cases at the jet near-field regions. This growth rate slowed down at the jet far-field regions. The overall jet structure was observed to be attached to the ground surface in jet far-field regions.

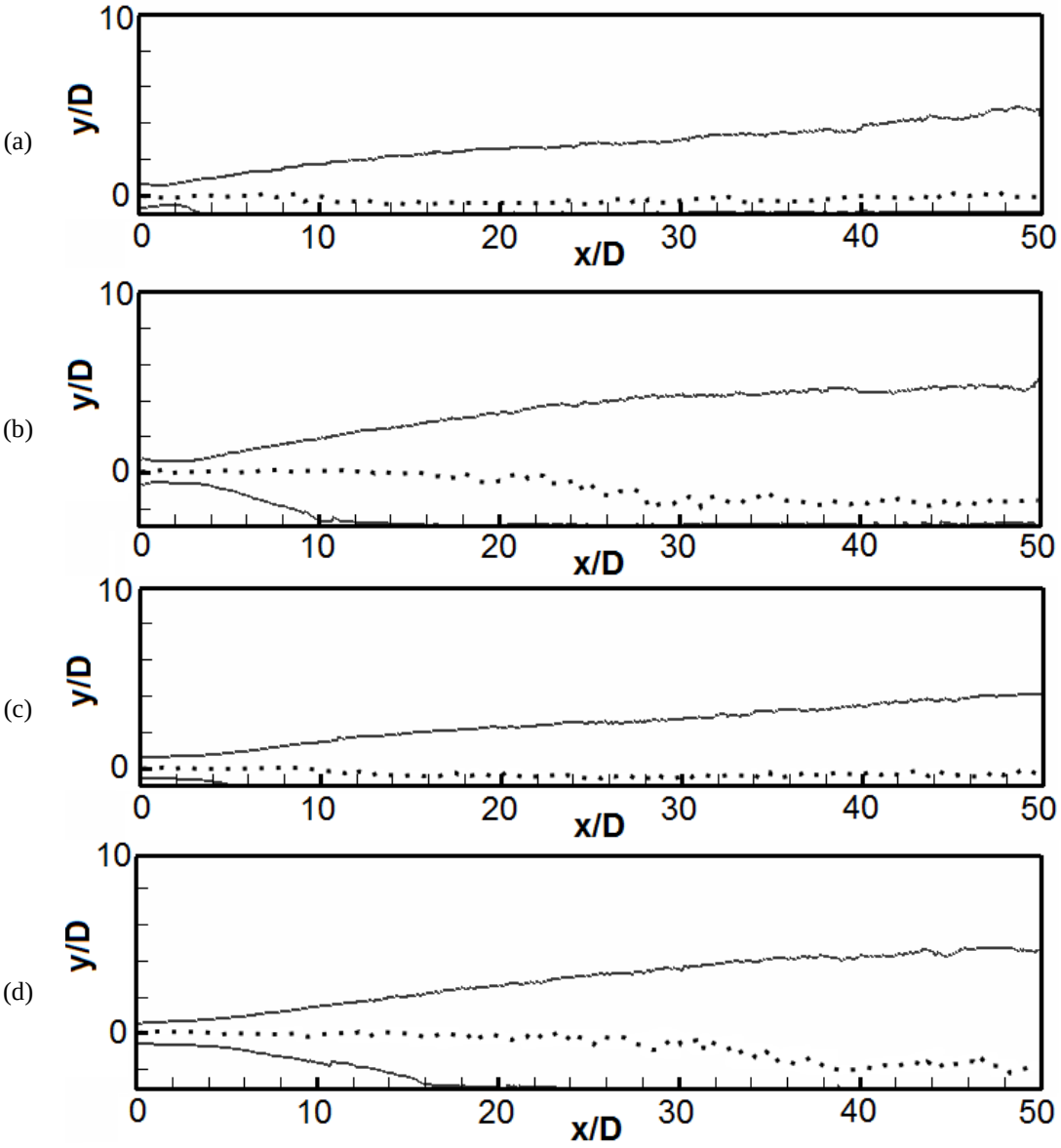

Figure 3.69 – Boundary contours for *Fr* = 250 located at (a) 1D, (b) 3D and *Fr* = 1000 located at (c) 1D and (d) 3D from the ground surface.

The flow widths for the jet flows near the ground surface are presented in Figure 3.70. Flow nominal half-width at each downstream location was computed as the distance between the jet boundary and the jet centerline at that point. Due to asymmetric nature of the flow, these values were calculated for $+y$ and $-y$ direction separately. These partial widths were denoted by δ_+ and δ_- respectively and the full width by $\delta_t \equiv \delta_+ + \delta_-$.

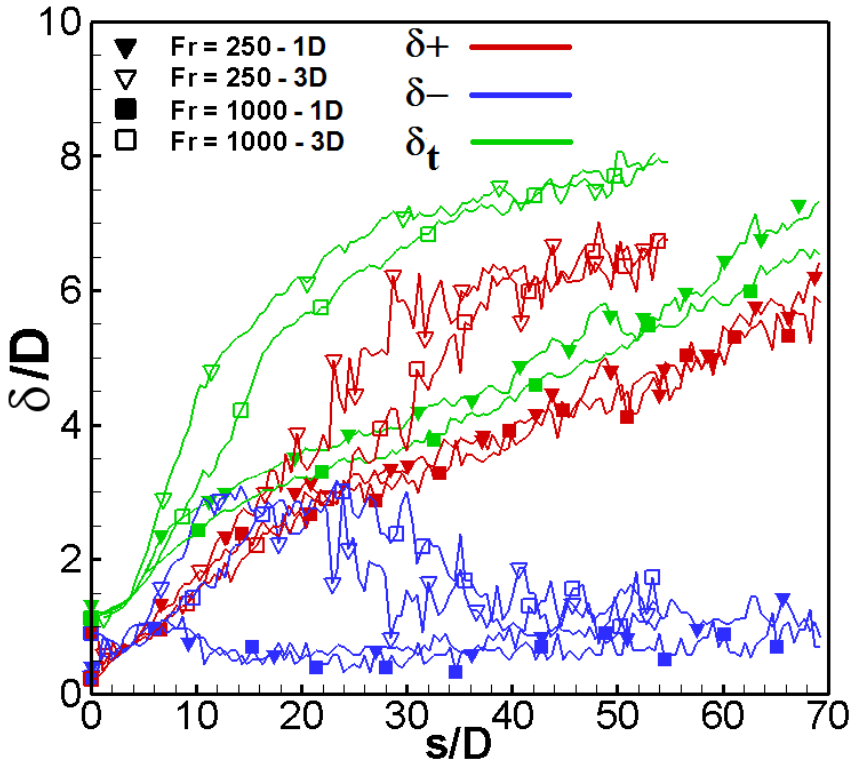

Figure 3.70 – Flow width, Jet near the ground surface.

The jet growth rate was observed to be similar to those of free jet flows at the jet near-field region (i.e. $s/D < 10$). Farther downstream, this growth rate slowed down as the jet attached to the ground surface and spread in the out-of-plane direction over the ground surface. This growth rate further reduced at the jet far-field region as the surface boundary layer thickened and retarded the jet lower boundary. It should be noted that in jet flows located at 3*D* distance from the ground surface, the overall jet structure deflected faster towards the ground surface in higher Froude numbers. This was as a result of the higher initial momentum in those cases which led to a higher pressure difference across the jet and higher surface forces consequently.

At the jet far-field regions ($s/D > 30$), faster growth rates were observed in jet flows located at 1*D* distance from the ground surface in comparison with flows located at 3*D* distance from the ground surface.

3.4.7.2 Ceiling

The boundary contours for the horizontal jets near a ceiling surface are presented in Figure 3.71. The jet centerline and boundary contours were calculated in the same manner as the jet flows near the ground surface.

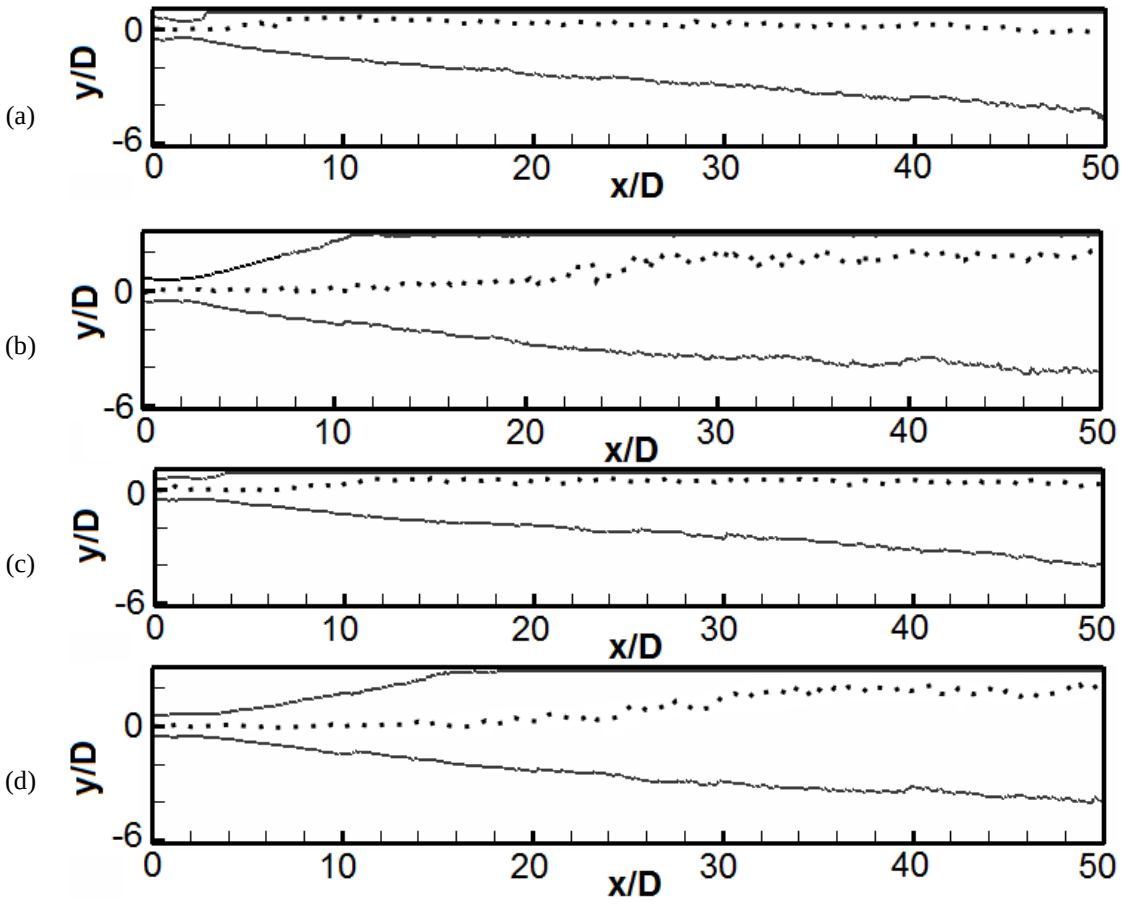

Figure 3.71 – Boundary contours for *Fr* = 250 located at (a) 1D, (b) 3D and *Fr* = 1000 located at (c) 1D and (d) 3D from the ceiling surface.

The jet boundary contours were observed to be very similar to those of jets near the ground surface. More pronounced jet centerlines deflection towards the surface were observed in jet flows near the ceiling surface comparing to the those near the ground surface. The flow widths for the jet flows near the ceiling surface were calculated similar to the cases near the ground surface and are presented in Figure 3.72.

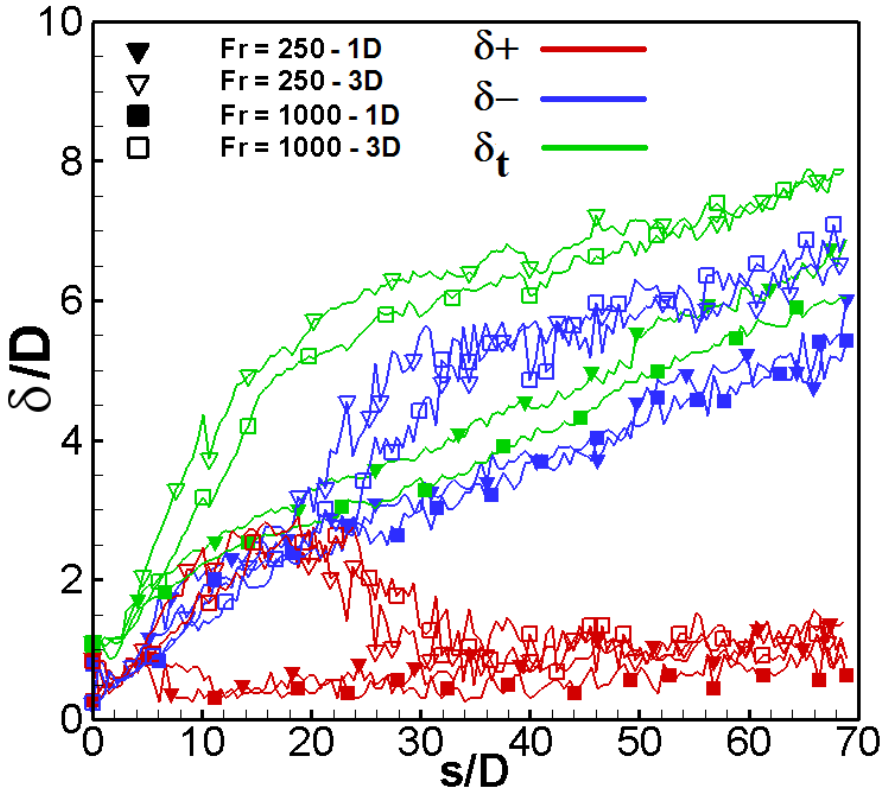

Figure 3.72 – Flow width, Jet near the ceiling surface.

Similar to the jet flows near the ground surface, flow partial-widths collapsed on each other in the jet potential core region (i.e. $s/D < 6$). The jet growth rates were similar to those of free jet cases in these regions. Downstream of the potential core area at the jet near-field region, the jet lower boundary growth rates were increased as the lower boundary thickened to fulfil the overall mass balance. Jet growth rates dropped at the jet far-field regions ($s/D > 30$) as the ceiling boundary layer developed and retarded the upper boundary of the jet. The overall jet growth rates and boundary contours of the jet flows cases near the ceiling and ground surfaces were found to be very similar. For instance the evolution of jet boundaries close to the surface as a function of downstream distance was observed to be very similar for jets near the ceiling and the ground surfaces.

It should be noted that for the jet flows located at 3*D* distance from the surface, sudden expansion of the jet boundary away from the surface was evident at *s* = 24D (see Figure 3.72).

3.4.7.3 Vertical Wall

The jet boundary contours along the centerline coordinate system, *s*, for the jet flows near the vertical wall are illustrated in Figure 3.73.

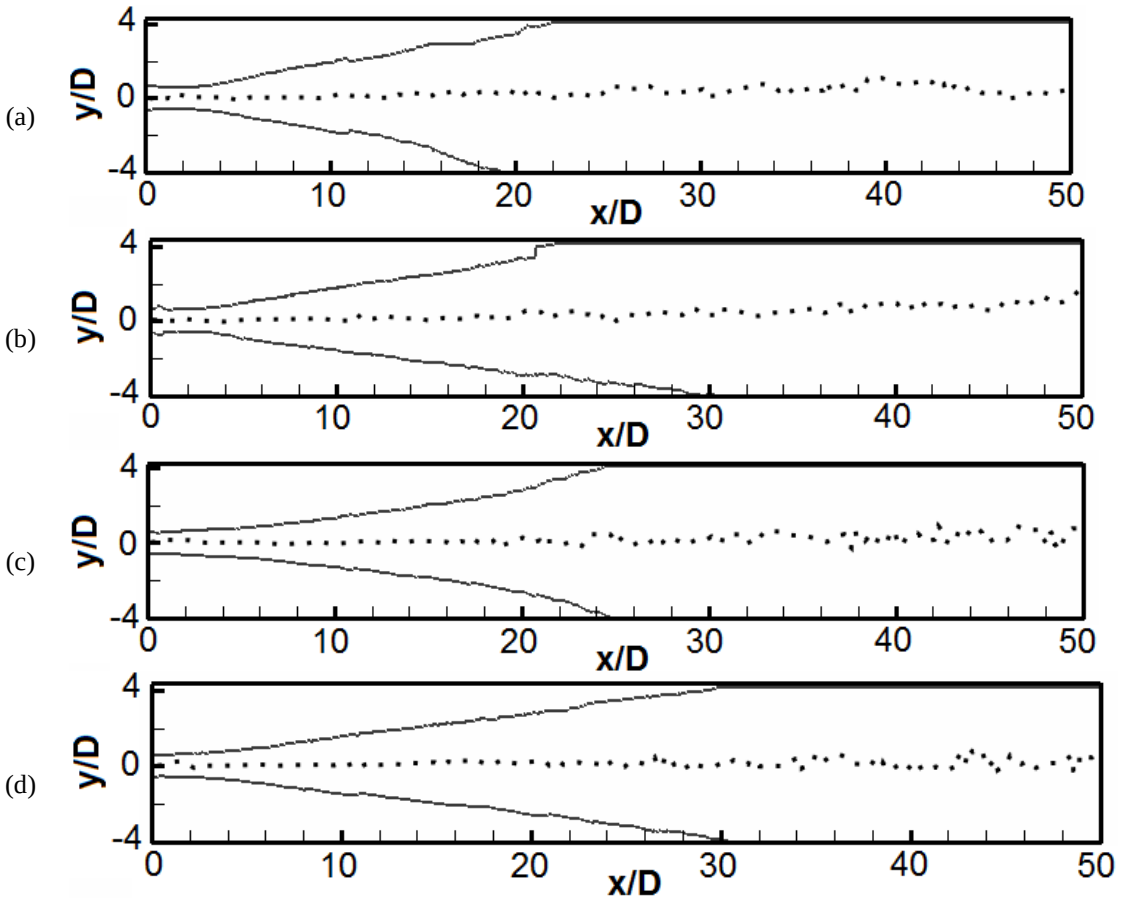

Figure 3.73 – Boundary contours for *Fr* = 250 located at (a) 1D, (b) 3D and *Fr* = 1000 located at (c) 1D and (d) 3D from the vertical wall surface.

The boundary contours and the jet centerlines were computed according to the same procedure used in flows near the ceiling and ground surfaces. The jet growth rate in potential core region was observed to be similar to those of free jet flows and also flows

near the ceiling and ground surfaces. The effects of buoyancy forces were observed to be more pronounced for the flows located at 3*D* distance from the wall surface.

Flow nominal half-width as a function of downstream distance, *s*, is presented in Figure 3.74. The values were calculated separately for the *+y* direction (i.e. upper boundary) and the *-y* direction (lower boundary) using the same procedure explained in previous section.

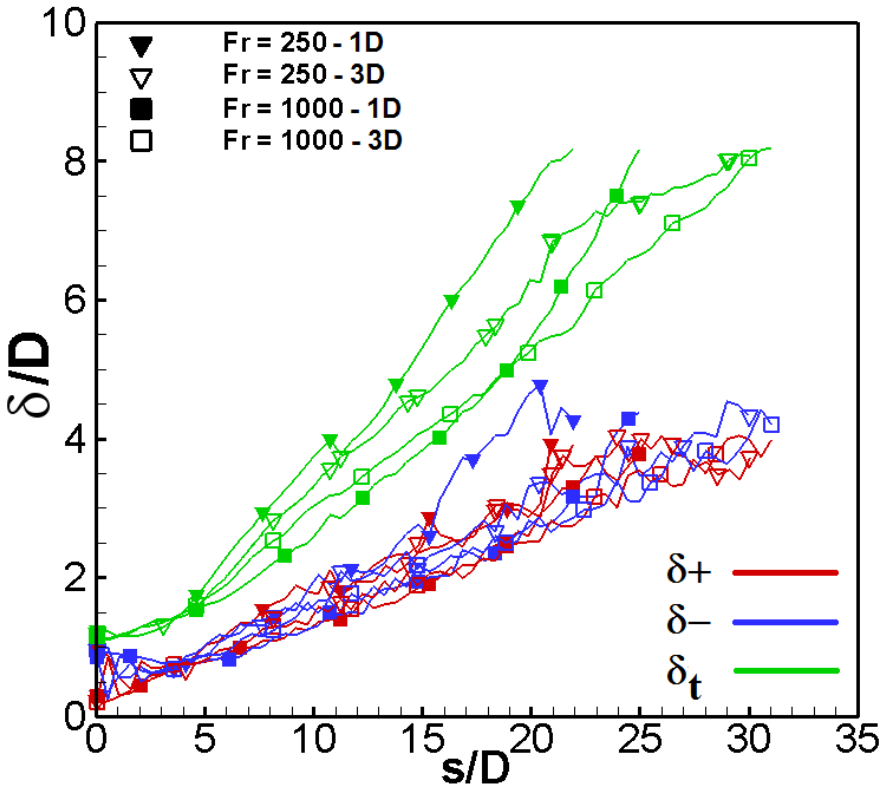

Figure 3.74 – Flow width, Jet near the vertical wall surface.

The δ_+ and δ_- nominal half-width values collapsed in the jet potential core region (i.e. $s/D < 5$) for all the cases considered herein. The growth rates were found to be similar to those of free jet flows in these regions. Downstream of the potential core area, the jet growth rates almost doubled as the jet attached to the wall surface. These plots are of a special importance as they illustrate the jet evolution in planes parallel to

the wall surface. The jet width plots of jet flows near the ceiling and ground surface represented the jet evolution normal to the surface.

As the jet attached to the wall surface the jet growth rates were observed to increase. This was helpful in the understanding of the 3-dimensional evolution of the wall-jets as function of downstream distance and led to a general conclusion for the overall 3-*D* structure of these flows. As the jet structure near the surface boundary attached to the surface the overall structure widened away from the surface in the planes parallel and normal to the wall surface in order to fulfill the mass balance. At the jet near-field regions, the growth rates were comparable in both parallel and normal planes. At the jet far-field regions, as the surface wall boundary layer was thickened, the jet growth rates were dropped in the jet center-plane normal to the wall surface. This increased the jet growth rate in the planes parallel to the surface to balance the mass flow rate which widened the overall jet structure in those planes. For the lower Froude numbers (i.e. *Fr* = 250), the effects of buoyancy forces were more pronounced. This may force some of the mass flow towards the direction of the buoyancy forces which led to a slower growth rate at the jet far-field regions.

CHAPTER 4

CONCLUSIONS

4.1 SUMMARY

Subsonic release of hydrogen from a sharp-edged round orifice was emulated using Helium as the working fluid for turbulent leaks with a circular geometry. The time-averaged velocity components and turbulent quantities were quantified using particle image velocimetry (PIV). The effects of buoyancy, crossflow and barrier surfaces on a horizontal round jet were characterised over a wide range of Froude numbers and experimental setup were designed and configured accordingly. Physical characteristics of the resultant flow structures were studied and presented in detail for each case.

Due to the bifurcated structure of the resultant jet in most of the cases considered herein, a new coordinate system was implemented to capture the downstream evolution of the flow closely. A brief summary and conclusion for each experiment is presented in following.

1) The effects of the sharp-edged orifice inflow configuration on physical characteristics of the resultant jet were quantified in details. The resultant initial velocity and the turbulent intensity profiles showed a saddle-back distribution and high initial turbulent intensity for high Froude numbers. The centerline velocity increase of approximately 30% was experienced in the potential core region. Faster velocity decay rates along the jet centerline and higher asymptotic ratio of rms of velocity fluctuations (i.e. $v'/u' \approx 0.75$) led to high ambient entrainment.

2) For free jet flows, the overall jet structure extended gradually and symmetrically for high Froude numbers. However, for Fr < 250, presence of strong buoyancy forces in the jet far-field regions reduced the downstream extent of the jet centerline. On the other hand the jet flow extended in the transverse direction as the upper boundary of the jet was expanded as a result of buoyancy induced mixings.
3) Different length scales have been implemented in the jet in crossflow and free jet cases in an attempt to find a global scaling factor for each case. The detailed information about the different scaling factors and the effect on the downstream evolution of the resultant jet are also discussed.
4) For jet in cross flow, three different length scales were implemented in an attempt to find a global scaling factor for the resultant vortical structure. The *D* scale was observed to be useful in resolving *r* dependent characteristics of the flow. The implementation of r^2D length scale led to the conclusion that regions with $y/r^2D<0.2$, corresponded to the jet near-filed regions at which *r* dependent properties of the jet such as the formation of counter-rotating vortex pair structure were developing. For the range of *r* values considered herein, the best centerline collapse was observed using the *rD* scale and it was implemented as the global scaling factor. Implementation of the *rD* factor in turbulence intensity and velocity decay rates distributions along the jet centerline suggested the vertical extension and three dimensionality of the resultant jet.
5) In jet flows in proximity to surface, the ambient entrainment at the jet boundary close to the surface was restricted but on the other hand, the boundary away from

the surface remained unobstructed which led to local pressure drop along the wall surface and deviation of the overall jet structure towards the surface.

6) Limited ambient entrainment in jet flows in proximity to surface increased the maximum extent of the resultant flow. Special attention was given to the offsetting distance and it was observed that the closer the surface to the jet centerline, the bigger the impact is on the extent of the resultant flow. The effect of strong buoyancy forces in amplifying and reducing the effect of the surface on the overall extent of the resultant jet was evident. For instance more developed wall-jet structure was observed in jet flows adjacent to the ceiling surface comparing to the same downstream location in jet flows close to the ground surface.

7) Comparing the dependency of the jet growth rates in planes normal and parallel to the surface led to the conclusion that the jet width growth rate normal to the surface was independent of the surface orientation. However, in the jet far-field regions faster jet width growth rate along the jet downstream distance was observed in planes parallel to the surface comparing to those in normal planes. This together with the decreasing trend in the values of longitudinal and transverse components of rms of velocity fluctuations in planes normal to the surface suggested the asymmetric extension of the jet structure over the adjacent surface downstream of the jet to surface reattachment point. In other words, downstream of the reattachment point, the extension of the jet boundary in profiles normal to the surface is much slower comparing to the jet extension parallel to the surface.

4.2 FUTURE WORK

Many physical characteristics of the horizontal dispersion cases emulating the hydrogen leaks were presented in this study using Helium as the working fluid. Effects of crossflow and adjacent barrier surfaces were discussed in order to achieve a better understanding of the hydrogen dispersion phenomena. These results may be used in the development of new safety standards. However, understanding of the flammable regions from controlled and uncontrolled releases of hydrogen is a must in development of safety standards. With the upper and lower explosive limits of hydrogen known, the flammable envelope surrounding the site of an uncontrolled hydrogen release can be found from the concentration field. Future concentration measurement using techniques such as Laser Induced Fluorescent would be a very valuable step in relating the velocity and concentration fields and to draw general conclusion for the development of new safety standards for the emerging hydrogen industry.

REFERENCES

Adrian, R. "Particle-Imaging Techniques for Experimental Fluid Mechanics." *Annual Review Fluid Mechanics,* 1991: 261-304.

Andreopoulos, J. "On the structure of the jets in a crossflow." *Journal of Fluid Mech.,* 1983: 163-197.

Andreopoulos, J, and W Rodi. "Experimental investigation of jets in a crossflow." *Fluid Mechanics,* 1984: 93-127.

Becker, HA, HC Hottal, and GC Williams. "The Nozzle fluid Concentration field of the round, turbulent, free jet." *Journal of Fluid Mechanics,* 1967: 285-303.

Broadwell, RE, and JE Breidenthal. "Structure and mixing of a transverse jet in incompressible flow." *Journal of Fluid. Mech.,* 1984: 405-412.

Chernyavsky, B, TC Wu, F Peneau, P Benard, P Oshkai, and N Djilali. "Numerical and experimental investigation of buoyant gas release: Application to hydrogen jets." *International journal of hydrogen energy*, 2010: 2645-2655.

Cosart, WP, and WH Schwarz. "The two-dimensional turbulent wall-jet." *J. Fluid. Mech. Vol. 10,* 1960: 481-495.

Crabb, D, DFG Durao, and JH Whitelaw. "A round jet normal to a crossflow." *Fluids engineering*, 1981: 142-153.

Crow, SC, and FH Champagne. "Orderly Structure in Jet Turbulence." *Journal and Fluid Mechanics,* 1971: 547-591.

Dongdong, S, and WL Adrian. "Boundary impingment and attachment of horizontal offset dense jets." *J. of Hydro-environment Research 5*, 2010: 15-24.

Fric, TF, and A Roshko. "Vortical structure in the wake of a transverse jet." *Journal of Fluid Mech.,* 1994: 1 - 47.

George, WK. *The Self-Preservation of turbulent flows and its relation to initial condition and coherent structures.* Ed. Arndt, R.E.A and George, W.K., 1989.

George, WK, JE Abrahamsson, RI Karlsson, L Lofdahl, and M Wosnik. “A similarity theory for the turbulent plane wall jet without external stream.” *J. Fluid Mech. vol. 425*, 2000: 367-411.

Glauert, MB. “The wall jet.” *J. Fluid Mech. Vol. 1*, 1956: 625.

Hama, FR. “Streamlines in a perturbed shear flow.” *Phys. Fluids.*, 1962: 644-650.

Hart, DP. “PIV error correction.” *Experiments in Fluids, Vol.29*, 2000: 13-22.

Hinds, WC. *Aerosol Technology: Properties, Behavior and Measurement of Airborne Particles.* New York: Wiley, 1999.

Hourri, A, B Angers, and P Benard. "Surface effects on flammable extent of hydrogen and methane jets." *International Journal of Hydrogen Energy*, 2009: 1569-1577.

Huang, H, D Dabiri, and M Gharib. "On error of digital particle image velocimetry." *Measurement Science & Technology 8*, 1997: 1427-1440.

Jirka, GH. “Integral model for Turbulent Buoyant jets in Unbounded Stratified Flows Part 1: Single Round Jet.” *Journal of Environmental Fluid Mechanics*, 2004: 1-56.

Kanury, AM. *An introduction to combustion phenomena.* Gordon & Breach Science Publishers Inc., 1977.

Keffer, JF, and WD Baines. “The round turbulent jet in cross-wind.” *Journal of Fluid Mech.*, 1963: 481-496.

Kelso, RM, TT Lim, and AE Perry. “An experimental study of a round jet in cross-flow.” *Journal of Fluid Mech.*, 1996: 111-144.

Kikkert, GA. *Buoyant Jets with Two and Three Dimensional Trajectories.* PhD Thesis, Christchurch, New Zealand: University of Canterbury, 2006.

Launder, BE, and J Rodi. “The Turbulent Wall Jet.” *Prog. Aerospace Sci., vol. 19*, 1981: 81-128.

List, PN, and EJ Papanicolaou. “Investigation of round vertical turbulent buoyant jets.” *J. Fluid Mech.*, 1988: vol. 195, pp. 341-391.

Lockwood, FC, and A Moneib. “Fluctiating Temperature Measuerments in heated round free jet.” *Combust. Sci. Technol.*, 1980: 63-81.

Mi, J, GJ Nathan, and DS Nobes. “Mixing characteristics axisymetric free jets from a contoured nozzle, an orrifice plate and a pipe.” *Journal of Fluid mechanics*, 2001: 878-883.

Mikhailova, NP, EU Repik, and YP Sosedko. “Optimal Control of Free-Stream Turbulence Intensity by Means of Honeycombs.” *Journal of Fluid Dynamics*, 1994: 429-437.

Moussa, ZM, JW Trischka, and S Eskinazi. “The near field in the mixing of a round jet with a cross-stream.” *Journal of Fluid Mech.*, 1977: 49-80.

Mungal, MG, and SH Smith. “Mixing, Structure and scaling of the jet in crossflow.” *Journal of Fluid Mech.*, 1998: 83-122.

Narasimha, R, K Yegna Narayan, and S Parthasarathy. “Parametric analysis of turbulent wall jets in still air.” *Aero. J.*, 1973: 355-359.

Nathan, GJ, J Mi, GJR Newbold, DS Nobes, and ZT Alwahabi. “Effects of subtle and dramatic changes to initial conditions on a jet's turbulent structure, mixing and combustion.” *15th Australasian Fluid Mechanics Conference.* Sydney: The University of Sydney, 2004.

Pratte, BD, and WD Baines. “Profiles of round turbulent jet in a cross flow.” *Journal of Hydronaut. Div.*, 1967: 53-64.

Quinn, WR. “Turbulent free jet flows issuing from sharp-edged rectangular slots: the influence of slot aspect ratio.” *Exp. Therm. Fluid. Sci*, 1992: 203-215.

Raffel, M, C Willer, and J Kompenhans. *Particle Image Velocimetry: A Particle Guide.* Springer, 2002.

Schefer, RW, WG Houf, and TC Williams. “Investigation of small scale unintended release of hydrogen: buoyancy effect.” *International journal of hydrogen energy*, 2008: 4702-4712.

Schefer, RW, WG Houf, and TC Williams. “Investigation of small-scale unintended release of hydrogen: momentum dominated regime.” *Internation journal of hydrogen energy*, 2008.

Schefer, RW, WG Houf, B Bourne, and J Colton. “Spatial and radiative properties of an open-flame hydrogen plume.” *International journal of hydrogen energy*, 2006: 1132-1140.

Schefer, RW, WG Houf, TC Williams, B Bourne, and J Colton. “Characterization of high-pressure, under expanded hydrogen jet flames.” *International journal of hydrogen energy*, 2007: 2081-2093.

Schlichting, H. *Boundary Layer Theory.* New York: McGraw Hill Inc., 1979.

Schwarz, WH, and WP Cosart. “The two-dimensional turbulent wall-jet.” *Fluid Mech. Vol. 10,* 1960: 481 – 495.

Smith, BS. *Wall Jet Boundary Layer Flows OverSmooth and Rough Surfaces.* Ph.D. dissertation, Aerospace and Ocean Engineering Dept., Virginia Tech,Blacksburg, VA, 2008.

Smith, EJ, J Mi, GJ Nathan, and BB Dally. “Preliminary Examination of a "Round jet initial condition anomaly" for k-e Turbulent Model.” *15th Australasian Fluid Mechanics Conference.* Sydney: The University of Sidney, 2004.

Stamhuis, E. “Basics and Principles of Particle Image Velocimetry for Mapping Biogenic and Biologically Relevant Flows.” *AquaticEcology, Vol40,* 2006: 463-479.

Su, LK, and MG Mungal. “Simultaneous measurements of scalar and velocity field evolution in turbulent crossflowing jets.” *Fluid Mechanics,* 2004: 1-45.

Townsend, AA. *The structure of turbulent shear flow, 2nd edition.* Cambridge University press, 1996.

Utami, T, RF Blackwelder, and T Ueno. “A cross-correlation technique for velocity field extraction from particulate visualization.” *Experiments in Fluids, Vol 10,* 1991: 213-223.

Velikorodny, AS. *Flow-Induced Sound and Vibration due to the Separated Shear Layer in Backward-Facing Step and Cavity Configurations.* University of Victoria, BC: PhD Thesis, 2009.

Vogel, S. *Life in Moving Fluids, the Physical Biology of Flow.* New Jersey: Princeton Press, 1994.

Volker, RE, and AJ Johnston. “Round buoyant jet entering shallow water.” *J. of Hydrogen research 31*, 1993: 121-138.

Westerweel, J. “Fundamentals of digital particle image velocimetry.” *Measurement Science & Technology, Vol 8,* 1997: 1379-1392.

Willert, CE, and M Gharib. “Digital Particle Image Velocimetry.” *Experiments in Fluids, Vol 10*, 1991: 181-193.

Wygnanski, I, Y Katz, and E Horev. “On the applicability of various scaling laws to the turbulent wall jet.” *J. Fluid Mech.* vol. 234 (1992): pp. 669-690.

Xu, G, and RA Antonia. “Effects of different initial condition on turbulent round jet.” *J. of Exp. Fluid;33,* 2002: 677-683.

Yuan, LL, RL Street, and FerzigerJH. “Large-eddy simulations of a round jet in crossflow.” *J. Fluid Mech. 379,* 1999: 71-104.